ABSTRACT

SOLAR FLARES AS OBSERVED IN THE LOW FREQUENCY MICROWAVE GYROSYNCHROTRON EMISSION

by
Shaheda Begum Shaik

Solar flares involve the sudden catastrophic release of magnetic energy stored in the Sun's corona. This dissertation focuses on investigating the low-frequency microwave, optically-thick gyrosynchrotron emission during solar flares for its spatial and spectral dynamics, characteristics, and role in the flare process.

The first part of this dissertation mainly addresses the spectral dynamics and characteristics of the source morphology. The high-resolution spectra of a set of microwave bursts observed by the Expanded Owens Valley Solar Array (EOVSA) during its commissioning phase in the $2.5 - 18$ GHz frequency range with 1-s time resolution are presented here. Out of the 12 events analyzed in this study, nine bursts exhibit a direct decrease with time in the optically thick spectral index α_l, an indicator of source morphology. Particularly, five of the bursts display "flat" spectrum ($\alpha_l \leq 1.0$) compared to that expected for a homogeneous/uniform source ($\alpha_l \approx 2.9$). These flat spectra at the low-frequencies (< 10 GHz) can be defined as the emission from a spatially inhomogeneous source with a large area and/or with multiple emission components. In a subset of six events with partial cross-correlation data, two events with flat spectra both show a source size of ~ 120 arcsec at $2.6 - 3$ GHz. Modeling based on inhomogeneity supports the conclusion that only multiple discrete sources can reproduce a flat spectrum. These flat spectra appear predominantly in the decay phase and typically grow flatter over the duration in most of the bursts, which indicates the increasing inhomogeneity and complexity of the emitting volume as the flare progresses. This large volume of flare emission filled with the trapped energetic particles is often invisible in other wavelengths, like hard X-rays, presumably due to

the collisionless conditions in these regions of low ambient density and magnetic field strength.

In the second study, imaging spectroscopy of gyrosynchrotron emission from C-class flare SOL2017-04-04 observed by EOVSA is presented. The microwave source observed at the low frequencies showed an extended emission that is almost ten times as large as the associated high frequency and hard X-ray flare emission. The source area seems to decrease steeply by more than an order of magnitude as we move from low to high frequencies. Unlike a single and straightforward loop "standard solar model" type flare, this event in the microwave emission shows the contribution of the multiple flux loops in different sizes with the "three-dimensional loop-loop interaction" scenario, resulting in the flare eruption. The emission at other wavelengths barely shows any sign of particle transport at the secondary sites where we see the low-frequency extended sources. These high-resolution microwave observations indicate that, after the main reconnection process, the accelerated particles have access to a much larger volume of the flaring region through the overlying loops.

SOLAR FLARES AS OBSERVED IN THE LOW FREQUENCY MICROWAVE GYROSYNCHROTRON EMISSION

by
Shaheda Begum Shaik

A Dissertation
Submitted to the Faculty of
New Jersey Institute of Technology and
Rutgers, The State University of New Jersey – Newark
in Partial Fulfillment of the Requirements for the Degree of
Doctor of Philosophy in Applied Physics

Department of Physics

August 2021

APPROVAL PAGE

SOLAR FLARES AS OBSERVED IN THE LOW FREQUENCY MICROWAVE GYROSYNCHROTRON EMISSION

Shaheda Begum Shaik

Dr. Dale E. Gary, Dissertation Advisor Date
Distinguished Professor of Physics, NJIT, Newark

Dr. Haimin Wang, Committee Member Date
Distinguished Professor of Physics, NJIT, Newark

Dr. Gregory Fleishman, Committee Member Date
Distinguished Research Professor of Physics, NJIT, Newark

Dr. Michele Pavanello, Committee Member Date
Professor of Physics, Rutgers University, Newark

Dr. Bin Chen, Committee Member Date
Associate Professor of Physics, NJIT, Newark

BIOGRAPHICAL SKETCH

Author: Shaheda Begum Shaik

Degree: Doctor of Philosophy

Date: August 2021

Undergraduate and Graduate Education:

- Doctor of Philosophy in Applied Physics,
  New Jersey Institute of Technology and Rutgers University, Newark, NJ, 2021
- Master of Science in Applied Physics,
  New Jersey Institute of Technology and Rutgers University, Newark, NJ, 2013
- Master of Science in Electronics,
  St. Joseph's College, Bharathidasan University, India, 2007
- Bachelor of Science in Mathematics, Physics, and Electronics
  Dr. A. E. R. Degree College, Sri Venkateswara University, India, 2005

Major: Applied Physics

Publications:

S. B. Shaik, & D. E. Gary, "Large Microwave Flare Sources observed by EOVSA Imaging Spectroscopy," in preparation

S. B. Shaik, & D. E. Gary, "Implications of Flat Optically Thick Microwave Spectra of Solar Flares for Source Size and Morphology," *The Astrophysical Journal*, in Press

S. Sreekumar, P. Vinod, S. Essy, J. P. Malkar, A. R. Rao, M. K. Hingar, V. P. Madhav, D. Debnath, T. C. Kotoch, A. Nandi, **S. B. Shaik,**, & S. K. Chakrabarti, "Instruments and their Test and Evaluation of RT-2 Payloads Aboard CORONAS-PHOTON V: Onboard Software, Data Structure, Telemetry and Telecommand," *Experimental Astronomy*, Vol. 29, pp. 109-133, 2011.

A. R. Rao, J. P. Malkar, M. K. Hingar, V. K. Agrawal, S. K. Chakrabarti, A. Nandi, D. Debnath, T.B. Kotoch, T. R. Chidambaram, P. Vinod, S. Sreekumar, Y. D. Kotov, A. S. Buslov, V. N. Yurov, V. G. Tyshkevich, A. I. Arkhangelskij, R. A. Zyatkov, **S. B. Shaik**, & P. K. Manoharan, "RT-2 Detection of Quasi-Periodic Pulsations in the 2009 July 5 Solar Hard X-ray Flare," *The Astrophysical Journal*, Vol. 714, pp. 1142-1148, 2010.

M. Lahkar, P. K. Manoharan, K. Mahalakshmi, K. Prabhu, G. Agalya, **S. B. Shaik**, & P. Revathi, "The Interplanetary Consequences of a Large CME", Book: Magnetic Coupling Between the Interior and the Atmosphere of the Sun," *Springer (Astrophysics and Space Science Proceedings)*, pp. 489-493, 2010.

S. B. Shaik, "Solar Eclipse Observation on May 21, 2012, from JVLA," *Master's Thesis*, 2013.

Selected Presentations:

S. B. Shaik, & D. E. Gary, "The Study of Flat Optically Thick Microwave Spectra Observed by EOVSA in Association with Source Size and Morphology," *AAS/Solar Physics Division Meeting*, 2018.

S. B. Shaik, & D. E. Gary "Flat optically thick microwave spectra observed by EOVSA," *Mid-Atlantic Section – American Physical Society meeting*, 2017.

S. B. Shaik, "Introduction on eclipses and the eclipse observed by VLA interferometer," *United Astronomy Clubs of New Jersey Public talk*, 2017.

S. B. Shaik, D. E. Gary, & G. M. Nita, "Source Dynamics of the Microwave Emission During a Solar Flare," *American Astronomical Society (AAS)/Solar Physics Division Meeting*, 2016.

S. B. Shaik, & D. E. Gary, "Flare dynamics with EOVSA observations in the active region 12297," *14th RHESSI Workshop*, 2015.

S. B. Shaik, & D. E. Gary, "Solar eclipse radio observation on May 21, 2012 from JVLA," *Female Research Showcase*, 2014

S. B. Shaik, & D. E. Gary, "Solar eclipse observation on May 21, 2012 from JVLA," *NJIT IX Annual GSA graduate student research day*, 2013

S. K. Chakrabarti, A. R. Rao, V. K. Agrawal, A. Nandi, D. Debnath, T. B. Kotoch, S. Sreekumar, Y. D. Kotov, A. I. Arkhangelskij, A. S. Buslov, E. M. Oreshnikov, V. N. Yurov, V. G. Tyshkevich, P. K. Manoharan, & **S. B. Shaik**, "RT-2 Observations of Solar Flares," *38th Committee on Space Research (COSPAR) Scientific Assembly*, 2010.

To my beloved late sister, Maha Jabeen Fathima Aapa,
beloved Daddy, Shaik Khaja,
darling husband, Jaya Chandra Konduru, and
dear A. P. J. Abdul Kalam sir.

ACKNOWLEDGMENT

First and foremost, I would like to express my heartfelt gratitude to my dissertation advisor Dr. Dale E. Gary. Thank you for taking a chance on me and having faith in me, and molded me into the researcher that I am today. The gratitude I have for others would not have had any meaning without having you as my advisor. You have indirectly bolstered my resolve and propelled me onwards no matter how unpleasant life got during these long years of Masters and Ph.D. Regardless of the number of times I stumbled on my way, your profound belief in my abilities and my work always kept me worth pushing forward. This gratitude is something that is far beyond my comprehension. I always admired your phenomenal style of mentorship, the fine techniques that you teach, and especially your unique way of visualizing the research data. I take this opportunity to tell you that I secretly look forward to the summer parties at your home and your homemade ice cream. I cherish the work that I did under your guidance, and I hope to pass this on to the next generation of researchers as I grow as a researcher. Finally, thank you for giving us EOVSA!

I thank my committee members for serving on my dissertation committee. My special thanks to Dr. Gregory Fleishman for being a great teacher by always making me understand the connection between research and fundamentals in Physics. I especially thank him and Dr. Bin Chen for carefully examining my work at all the presentations and discussions, which helped me mold my work. I thank Dr. Bin Chen and Dr. Sijie Yu for keeping research with fresh ideas by constantly updating and looking into current trends and technologies.

Special thanks to Dr. Haimin Wang for his unwavering support and always being there to track my progress through each doctoral milestone. I thank Dr. Michele Pavanello for immediately accepting to serve on my committee at short notice. I want to thank Dr. Gelu Nita for helping me with the software tools used in this dissertation.

My career in Solar Astrophysics would not have taken shape during its infancy in India without Dr. A R Rao, a great mentor and a friend to whom I always reach out. Thank you for your unconditional support throughout the Ph.D. admission process. I fondly reminisce about our chats on building X-ray detectors and the physics behind them during my time at TIFR and ISRO institutes.

I take this chance to express my love and gratitude towards my spiritual master Sri Sri Ravishankar, the founder of the Art of Living organization, for teaching me the knowledge of अथ योगानुशासनम् (*"Atha yoga-anushasanam"*) - "the value of the moment 'Now' and the discipline of Yoga, the union" and being अहो निरञ्जनः (*"Aho niranjana"*) - with self-realization and enthusiasm. My gratitude to him for helping me bring back to my usual "self".

I thank Dr. Daniel Saland for his therapy sessions during his years at the Center for Counseling and Psychological Services (CCAPS), NJIT. While writing this dissertation, I remembered and incorporated the writing tips that he gave from his Ph.D. dissertation.

I thank Miller Goss, NRAO, New Mexico, for his long discussions about the science and the history of Radio Astronomy. He helped me to break some of the cultural obstacles in the US.

I gratefully acknowledge the Teaching Assistantship funding from the Department of Physics. I convey my gratitude to the administrative staff in the Center for Solar-Terrestrial Research (CSTR) and in the Department of Physics, NJIT, Ms. Cheryl E. James, Ms. Christine A. Oertel, Ms. Leslie M. Williams, Ms. Cindy Montalvo-Harden for their work to make my graduate life easier. I thank Dr. Sung Maeng, the Physics lab director, for being an amazing colleague and friend during my teaching assistant duties in the Physics lab, which made me instruct effectively and bring out the teacher in me.

I thank Sotirios G. Ziavras and Clarisa González-Lenahan, for reviewing this document keenly and taking me through the process as smoothly as possible, even during these times of pandemic.

I thank my super-hero dad, Shaik Khaja, for his unshakeable love and guidance throughout my studies and life events. I am indebted for all the moral values he inculcated in me right from my childhood.

My love to my sister Jabeen for "all" that she did for me and for making me the person that I am today. She is the one who instilled confidence in me to pursue a doctoral degree when I was hesitant.

I thank my childhood friend and husband, Jaya Chandra Konduru, for his love and always being by my side whenever I needed him. Though we disagree on some ideologies, he is always someone with whom I can be myself in my natural self.

My love to my daughter Tara Jabeen for keeping me on my toes and making me live in the moment every day. I take pride in saying that she is the one who fulfills the women and the mother in me. I wish she was born to me much earlier in my life and spurred me to finish this thesis much earlier.

I thank my wonderful niece Shaheen Bibi, my brothers Shaik Abdul Rahiman, Shaik Reyazuddin, and their families for always being there to support and take pride in every achievement that I had in these years of Ph.D.

I thank my friend Venkatakrishnan Rengarajan for his constant support, numerous discussions, and journal clubs that helped me in my research work. He truly makes my world a better place by just being in it.

I thank my friend Sajal Jain for her love and the beautiful bond we share, even though we were not born together biologically. The purest soul she is!

I thank my beloved friend, Mr. Muthu Kumaravel, for being someone who steadied me during the turbulent times that shook me. I also want to thank my dear friend Dr. B. Praveen Kumar for being an amazing inspiration and for growing as a buddy with me.

My heartfelt thanks to each one of my lovely friends, Siva Kumar Valluri, Sherry Chhabra, Harshita Gedela, and Riddhi Chavda, for giving me all the support and love during all these years and creating many beautiful memories together. They were always there during all my precious moments in recent years. My special mention to Sherry Chhabra for her tremendous company while writing this dissertation.

I thank my friends Qin Li, David Apigo, and Roman Basisty for all the discussions we had during the physics courses we attended. I thank my friends and schoolmates Natsuha Kuroda, Jiasheng Wang, Yi Chai, Yingjie Lou, Yuqian Wei, and Meiqi Wang for making all these years enjoyable. Thanks to my colleagues, the staff, the faculty, and group members in the NJIT research centers who directly or indirectly contributed to my Ph.D. dissertation.

No matter what surprises the future holds for me, I am happy and proud that I could pass through the rough phase after my sister's demise and my early years at NJIT to stand strong and write these words with a wide smile of contentment. There were days when my strategies were flawed throughout these years, and I was not conventionally fast enough, but whatever the reasons were, I am very happy today that they were not due to lack of effort; efforts either dealing with research work or dealing with my own mind.

TABLE OF CONTENTS

TABLE OF CONTENTS
(Continued)

Chapter **Page**

LIST OF TABLES

Table **Page**

LIST OF FIGURES

List of Figures
(Continued)

Figure **Page**

List of Figures
(Continued)

Figure **Page**

LIST OF FIGURES
(Continued)

Chapter 1

INTRODUCTION

1.1 The Sun

Our nearest star, the Sun, acts as a natural laboratory to study fundamental physical processes that occur across the universe. It is a main sequence G-type star with a mass of 1.99 x 10^{30} kg, radius of 6.96 x 10^5 km, and luminosity of 3.84 x 10^{33} erg s^{-1}. The heat and light radiated from the Sun make life possible on the Earth. The Sun emits at almost all the wavelengths in the electromagnetic (EM) spectrum, some of which are harmful such as X-rays, ultraviolet (UV), γ-rays and are blocked by the Earth's atmosphere. Some part of radio, UV, infrared (IR) along with the complete visible wavelengths reach the surface. The visible surface of the Sun, the photosphere has a temperature of around 5800 K. Moreover, as we move to the outer layers of the photosphere the temperature increases to a few million degrees in the outermost layer, the corona. The most energetic phenomena of the Sun manifest in this part of the solar atmosphere.

Solar flares, coronal mass ejections (CMEs), and solar energetic particle (SEP) events are some examples of the most impulsive phenomena observed in our solar system. A solar flare is a sudden catastrophic release of magnetic energy from the Sun, and a CME is an eruption carrying $\sim 10^{12}$ kg of coronal plasma material embedded in the magnetic field, which is ejected out into the interplanetary space. The exact association between flares and CMEs, however, is still debatable. Although CMEs are believed to be triggered by flares, they are sometimes observed in the absence of flares as well. Depending on their orientation and direction, CMEs can interact with the magnetic field of Earth, causing geomagnetic storms. Distortion of the shape of the Earth's magnetosphere, dramatic auroral displays (northern and southern lights), magnetic storms affecting satellites and astronauts, outage of radio communications, power systems, and pipeline corrosion are some consequences of such an interaction. The high-energy particles and radiation (mainly X-rays) from the flares disturb the Earth's ionosphere, heat up and expand the Earth's outer atmosphere, and in turn disrupt radio communications. In addition, intense radio emission from flares and the variations in the Earth's atmospheric layers can also degrade satellite communications and precision of Global Positioning System (GPS) measurements [29, 52]. Therefore, studying the physical processes of the Sun to better comprehend and predict solar flares, CMEs, and SEPs plays a vital role in understanding space weather.

1.2 Flares on the Sun

Solar flares, in general, are triggered by magnetic reconnection and are responsible for the large-scale restructuring of the coronal magnetic field and coronal heating [[11], and references therein]. A flare can induce emission across the whole electromagnetic spectrum, from radio waves to gamma rays. During a flare, the total energy expended is typically on the order of 10^{30} ergs. This flare energy is compared to be ten million times greater than the energy released in a volcanic explosion. On the other hand, this energy is one-tenth of the total energy emitted every second by the Sun.

In literature, Richard Christopher Carrington and Richard Hodgson were the first to detect a flare in white-light independently in 1859 [13, 47]. They observed the flare as localized, minute-long brightenings on the Sun, which remained a mystery during that time. A few years after this study, the Sun and the solar flares were typically studied using the chromospheric hydrogen $H\alpha$ line observations. Followed by these, coronal radio emissions in meter wavelength range and increase in solar irradiance during a solar radio burst were detected in 1942. In the late 1950s, solar flares were first observed in hard X-ray emission [93]. Later, in 1968, [84] a significant fraction of initial energy in the flare was seen to show enhancements

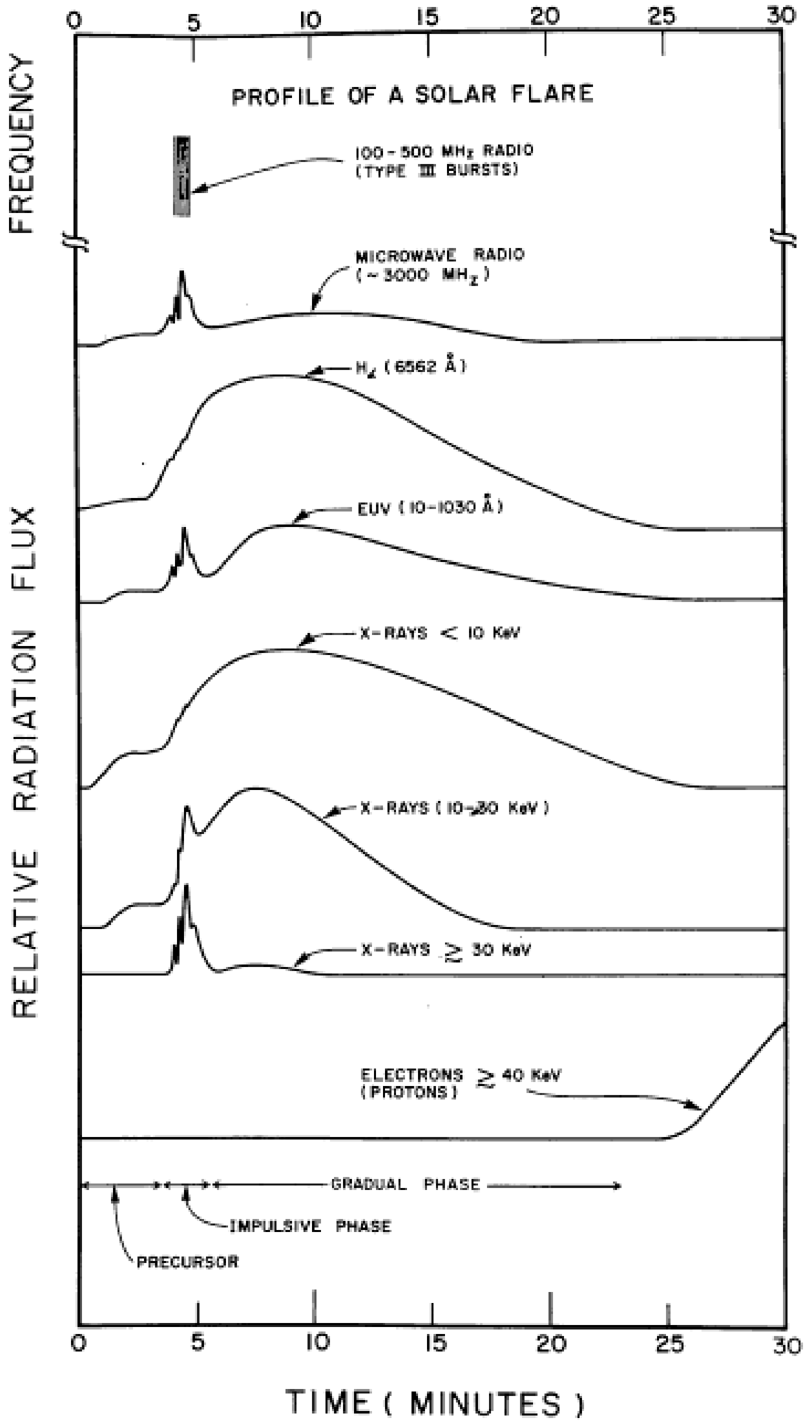

Figure 1.1 Schematic representation of a solar flare observed in different wavelengths of the electromagnetic wavelengths (vertical axis) at various phases as marked at the bottom with the horizontal axis.
Source: [51]

in radio centimeter wavelength and hard X-ray emissions. Furthermore, extreme ultra-violet (EUV) and soft X-ray observations have revealed that the coronal active region loops heat up to 1.5 to 30 MK by the flare energy. Since then, solar flares are continuously recorded by various space-borne and ground-based observations throughout the electromagnetic spectrum ranging from radio waves to γ-rays. Even after 162 years since discovering solar flares and even after a large heritage of flares observations, flares still remain as unclear and complex problems in astrophysics.

Figure 1.1 shows the schematic time profile of a flare in multiwavelength electromagnetic emissions, although each flare is unique and differs in terms of intensity and size. Generally, a flare is roughly divided into three phases, namely *preflare or precursor, impulsive, and gradual or decay phase* as shown in the bottom of the schematic [51]. In the *preflare phase*, the plasma in the solar corona starts heating up and becomes visible in soft X-rays, radio and EUV. This phase is seen as a slight relative increase in the radiation, indicating the possible occurrence of the next phase of explosive emission within a short interval of time. In the *impulsive phase*, a large number of energetic electrons and ions are accelerated through a sudden release of magnetic energy. This phase is characterized by apparent quick rise and decay of hard X-rays and microwave radiation. Hard X-rays are produced by bremsstrahlung when free electrons interact with the ions and emit photons as they change their paths due to the Coulomb force. Microwaves are generated by gyration of mildly relativistic electrons trapped in the magnetic field. The incoherent microwave emission at centimeter wavelengths from non-thermal electrons fills the flaring magnetic loops. At the chromospheric level, the hard X-ray footpoint sources appear characteristically in this phase [48] sometimes with single or multiple sources [74, 114]. The soft X-rays and $H\alpha$ emissions reach their peak after this impulsive phase, where energy is more gently released. In the *decay phase*, the plasma in the corona restores to its near-original state. In the high altitudes of the corona ($> 1.2\ R_\odot$, where $R_{\odot}$ is the Sun's photospheric radius), particles still be accelerated by magnetic reconfiguration, and shock waves, leading to radio bursts in meter wavelengths and further creating particle events in the interplanetary medium. As seen in the figure, the duration of these stages can be as short as a few seconds to an hour.

Flares are usually classified in levels as given in Table 1.1 according to the peak flux intensities of $1 - 8$ Å (1.5 to 12.4 keV) soft X-ray wavelength channel in watts per square meter (W/m^2) measured with *National Oceanic and Atmospheric Administration (NOAA)/Geostationary Operational Environmental Satellite (GOES)* spacecraft located at the Earth.

Table 1.1 Solar Flare Classification

Classification	1 -8 Å Peak flux intensity (W/m^2)
A	$\leq 10^{-7}$
B	$10^{-7} - 10^{-6}$
C	$10^{-6} - 10^{-5}$
M	$10^{-5} - 10^{-4}$
X	$\geq 10^{-4}$

Each of these letter classes is divided into a linear scale from 1 to 9 and are noted as a suffix (for example, M3 flare has a peak flux intensity of 3 x 10^{-5} W/m^2). X-class is the largest and strongest, and A & B-classes are the lowest of solar flares. X-class flare exceeding X9 peak flux intensity is only observed very occasionally.

1.2.1 The Standard Two-dimensional Flare Model

Many theoretical flare models have been developed depending on the initial magnetic topology, instabilities/drivers of the flares, and CMEs. The standard solar two-dimension (2D) flare model is a widely accepted and well-understood one that explains most solar flare observations. This model is evolved from the concepts of Carmichael, Sturrock, Hirayama, Kopp, and Pneuman, known from the initials of five authors as "the CSHKP model". [12, 108, 46, 57].

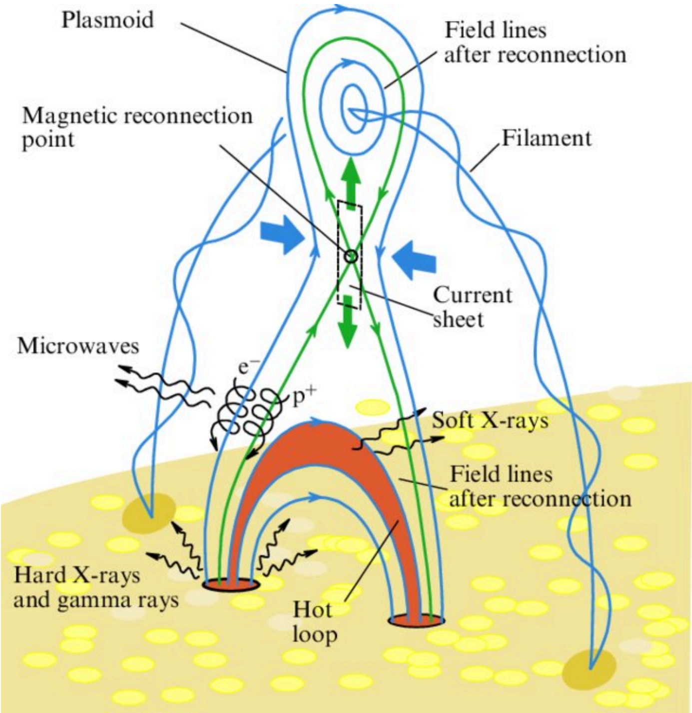

Figure 1.2 The standard model of a solar flare. The flare is triggered by the rising filament/prominence resulting in the X-point reconnection and the cool plasma inflow from the sides of the reconnecting loops marked with the blue arrows. The green arrows mark the outflow of the hot plasma moving upwards and downwards. The particles accelerated during the reconnection get trapped and move along the field lines giving rise to microwaves. These particles travel towards their footpoints and emit hard X-rays and sometimes gamma rays. Due to precipitation from the chromosphere, the entire post-flare loops heat up and emit soft X-rays.
Source: [75], adapted from [103]

Figure 1.2 depicts the flare scenario where the rising filament located above the neutral line of the active region acts as the initial driver of the flare. The release of the energy stored in the non-potential magnetic system happens due to the restructuring of the field by magnetic reconnection. This reconnection occurs at the formation of a stretched current sheet above a loop due to the rising filament. In some cases, twisting of the loop by displacement of its footpoints relative to each other can also lead to reconnection of the field lines. The X-point region of reconnection is assumed to be the main location of the major release of magnetic energy heating up the local coronal plasma and accelerating the non-thermal particles becoming detectable in hard X-rays, microwave, and other wavelength emissions. These particles go through a sequence of processes like acceleration, injection, propagation, trapping, and precipitation. A portion of the accelerated particles escape the Sun's surface and are observed as many consequent phenomena in the interplanetary space. The remainder of these particles is captured in the magnetic field trap and travels along the field lines down to the surface of the Sun. The electrons trapped in the magnetic field loop produce gyrosynchrotron emission at 1 GHz to a few tens and hundreds of GHz frequency range. Close to the footpoints of the loops, where the magnetic field is strong and particle density is high, the non-thermal electrons undergo Coloumb collisions with the ambient ions, generating bremsstrahlung emission observed in hard X-rays and gamma rays at energies ranging from tens of keV up to ∼10 MeV. As a result of thermal conduction of Maxwellian thermal electrons and precipitation of nonthermal electron, the chromospheric footpoints of the newly reconnected magnetic field lines are heated, giving rise to soft X-rays, radio, and EUV emissions. The plasmoid shown in the figure is a blob of plasma bound within the twisted magnetic tube, which eventually erupts as a CME. During the late phase of the flare, subsequent reconnections may continue, giving rise to long duration X-ray emission with cusp structure. As the loops cool down by conduction and radiative loss, they become visible in EUV and Hα.

1.2.2 The Three-dimensional Multi-loop Flare Model

In some flares, instead of having one single system of magnetic loops, multiple loops can interact, leading to a more complex three-dimensional (3D) reconnection. This type of reconnection involves small and large-scale magnetic loop configurations sometimes connecting between two active regions. Some studies with available spatial locations of the radio (mainly at 17 GHz), and hard and soft X-ray sources have

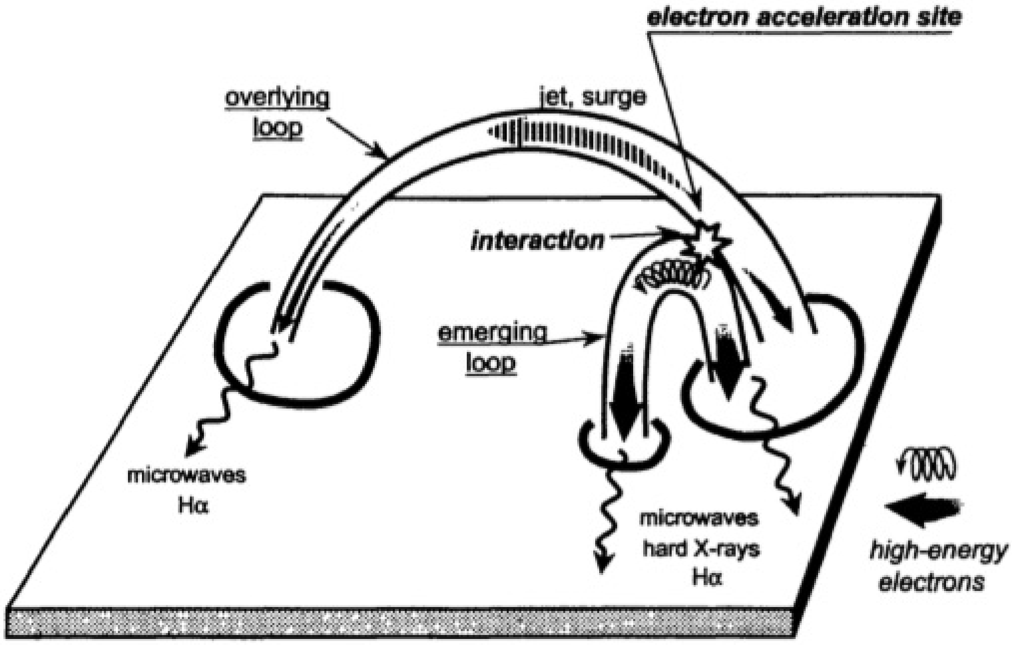

Figure 1.3 Schematic drawing of a double-loop flare indicating the transport of high energetic electrons from the acceleration site through the loops to the footpoints of the loops interacted.
Source: [45]

reported double-loop, and multiple-loop flaring system [82, 44, 45, 81, 87, 62] as shown in Figure 1.3.

Hanaoka[43, 45] have reported that the emerging flux forming the small loop interacts with the large overlying loop resulting in the onset of flares and microflares. Time delays were observed by some fractions of a second between radio sources at the main flare site and a remote site at the leg of a large loop [45]. This delay suggests the time of flight taken by the energetic electrons to travel from the main site to the farther site along the magnetic field lines of the large loop.

1.3 Radio Emission in Solar Flares

After the first discoveries of radio emission from the Milky Way galaxy and the Sun by Karl Jansky (1930) and Grote Reber (1944), research based on radio phenomena remains a productive and important field of study. Over the decades of evolution, solar radio observations have been carried over a broad frequency window of a few kHz to a few hundred GHz that can be used to explore phenomena from close to the surface of the Sun (in the corona) to the Earth (at 1 AU) and beyond. The radio emission from solar flares provides numerous diagnostic tools to examine the particle acceleration, energy release, and transport of particles with the magnetized plasma during the flares.

1.3.1 Radio Emission Mechanisms

Distinct emission mechanisms are responsible for producing various wavelengths of the radio and microwave bands over the electromagnetic spectrum. These radio emission mechanisms are mainly dominated by the free electrons, either in a thermal or a non-thermal distribution. The radio emission is further classified as coherent and incoherent mechanisms depending on the phase association of these electrons with the emitted photons, as shown in Table 1.2.

In the *incoherent emission*, the emitted photons have no phase association, that is no coherence. The electrons act individually to produce the emission but their numbers are proportional to the emission. *Coherent emissions* have the emitted photons that are in phase from the electrons which also accelerate in phase and act together to produce the emission. Coherent emission is mainly observed below 1-2 GHz due to the wave-wave and wave-particle interactions. In this research, we discuss and focus on incoherent emissions that occur during solar flares.

Incoherent emission is commonly detected on the Sun are mainly observed from two emission mechanisms of free-free/bremsstrahlung and gyromagnetic (gyroresonance or gyrosynchrotron mechanisms). Free-free radio emission is produced due to the collisions between thermal electrons and ions. This emission is dominated by the radio radiation from the non-flaring active regions and the quiet Sun. The gyromagnetic emission is produced by the accelerated electrons gyrating in

Table 1.2 Radio Emission Mechanisms During Solar Flares

Emission mechanism	Frequency	Source/Exciter
(1) Incoherent radio emission:		
(1a) Free-free emission (bremsstrahlung)	$\nu > 1$ GHz	Thermal plasma
– Microwave postbursts		Thermal plasma
(1b) Gyroemission	$\omega = \mathrm{s}\Omega_e$	
Gyroresonance emission	(s = 1, 2, 3, 4)	Thermal electrons
Gyrosynchrotron emission	(s ≈10–100)	Mildly relativistic electrons
– Type IV moving		Trapped electrons
– Microwave type IV		Trapped electrons
(2) Coherent Radio Emission:		
(2a) Plasma emission	$\nu_p = 9000\sqrt{n_e}$	Electron beams
– Type I storms		Langmuir turbulence
– Type II bursts		Beams from shocks
– Type III bursts		Upward propagating beams
– Reverse-slope (RS) bursts		Downward propagating beams
– Type J bursts		Beams along closed loops
– Type U bursts		Beams along closed loops
– Type IV continuum		Trapped electrons
– Type V		Electron beams
(2b) Electron-cyclotron maser	$\omega = s\Omega/\gamma + k_{\|\|}\nu_{\|\|}$	Losscones
- Decimetric ms spike bursts		Losscones

ν - radio frequency, ω - angular frequency ($2\pi\nu$), Ω_e - gyrofrequency, s - harmonic number, ν_p - plasma frequency, n_e - electron density, Ω/γ - relativistic gyrofrequency Source: [2, 3]

the magnetic field. This gyromagnetic emission is called *gyroresonance* when the gyrating electrons are thermal and have a moderate temperature ($\sim 10^6$ K), which corresponds to the non-flaring regions in the corona. The gyromagnetic emission is called as *gyrosynchrotron (GS)* when the electrons gyrating in the magnetic field are mildly relativistic and are with thermal and non-thermal energy distributions. Such incoherent gyrosynchrotron emission plays a significant role at millimeter and centimeter wavelengths during the impulsive phase of flares. The details of the gyrosynchrotron emission during flares are discussed in Section 1.3.3.

1.3.2 Radiative Transfer

In the Rayleigh-Jeans regime, for radio frequencies $h\nu \ll kT$, the specific intensity I_ν and the source function S_ν can be expressed in brightness temperature T_b as

$$I_\nu = kT_b\nu^2/c^2, \tag{1.1}$$

and

$$S_\nu = \left(\frac{\eta_\nu}{k_\nu}\right) kT_{\text{eff}}\nu^2/c^2, \text{respectively.} \tag{1.2}$$

Where h is Planck's constant, f is the radio frequency, k is Boltzmann's constant, and T_{eff} is the effective temperature of the emitting volume. η_ν and k_ν are the emission and absorption coefficients, respectively.

The radiative transfer equation for continuum radio emission is expressed along a given line of sight as

$$T_b = \int T_{\text{eff}} e^{-\tau'_\nu} d\tau'_\nu + T_b^{-\tau_\nu}, \tag{1.3}$$

where $\tau_\nu = \int \kappa_\nu dl$ is the optical depth.

For an isolated source, T_{eff} is constant

$$T_b = T_{\text{eff}}, \quad \text{for } \tau_\nu \gg 1 \text{ optically thick source} \tag{1.4}$$

$$T_b = T_{\text{eff}}(1 - e^{-\tau_\nu}), \tag{1.5}$$

$$T_b = \tau_\nu T_{\text{eff}} = \frac{c^2 \eta_\nu L}{k\nu^2}, \quad \text{for } \tau_\nu \ll 1 \text{ optically thin source.} \tag{1.6}$$

The flux density S of a radio source through spatially unresolved and integrated observations in two polarizations is related to the brightness temperature through

$$S(\nu) = \frac{2k\nu^2}{c^2} \int T_b(\nu) d\Omega, \tag{1.7}$$

where c is the velocity of light, $d\Omega$ is the differential solid angle in steradians, and T_b is expressed in Kelvin. S_ν may be expressed in the units of Jansky (Jy) or conveniently expressed in solar observations with solar flux unit (sfu) [1 sfu = 10^4 Jy = 10^{-22} Wm^{-2}Hz^{-1}]. This flux density changes as a function of frequency from a positive to negative slope as shown in Figure 1.4 along with the brightness temperature spectrum.

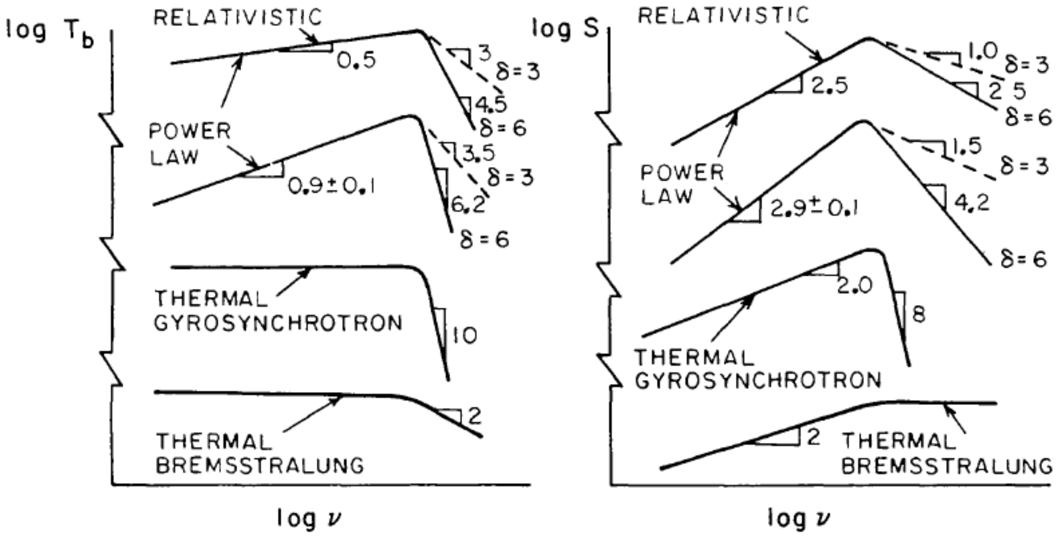

Figure 1.4 Schematic of universal spectra for the brightness temperature (T_b) and the flux density (S) from a homogeneous source. The top two curves are the gyrosynchrotron radiation for the power-law distribution from highly and mildly relativistic electrons, respectively.
Source: [17]

1.3.3 Gyrosynchrotron Emission

In the microwave band, gyrosynchrotron emission during flares is typically produced from non-thermal electrons with energies in the range of ≈100 keV to a few MeV. Thus, gyrosynchrotron emission could be associated with the acceleration mechanisms of hard X-ray and gamma rays. Gyrosynchrotron emission dominates the emission at centimeter and millimeter wavelengths (cm-λ and mm-λ). Commonly observed gyrosynchrotron emission is a broadband microwave spectrum in the typical frequency range of $\approx$ 2 to 20 GHz [111, 95, 109, 94, 17, 53].

Gyrosynchrotron radiation provides necessary information on the physical parameters of the flare sources and the kinematics of the accelerated electrons in the flaring loops. gyrosynchrotron emission is the main mechanism during flares, produced from the mildly-relativistic electrons that gyrate around the magnetic field. As the electrons move in the magnetic field, they experience the Lorentz force, which makes the electrons gyrate at the gyrofrequency ν_B depending on the magnetic field strength B (in Gauss).

$$\nu_B = \omega_e/2\pi = eB/2\pi m_e c \approx 2.8 \times 10^6 B \quad Hz. \tag{1.8}$$

In the range of high energies of electrons, the emission beams towards the direction of motion of the electrons due to relativistic effects and generates harmonics at frequency $\nu = s\nu_B$. As shown in Table 1.2, the mildly relativistic electrons correspond to gyrosynchrotron radiation, where the electrons gyrate at a small but significant fraction of the speed of light observed at high harmonics s = 10 - 100. In contrast, gyroresonance emission from electrons at a higher velocity and relativistic speeds gives rise to gyroresonance line at low harmonics of s = 1, 2, 3,.so on.

The expressions for gyrosynchrotron emissivity and absorption are somewhat complex [95] and therefore often need modern computing resources to solve numerically [21], although with some simplified approximations [94, 19, 17, 53] of homogeneous source emission. Some useful expressions were derived by [17] for the gyrosynchrotron emission from the isotropic pitch angle electron distribution valid over the range $2 < \delta < 7$, $\theta > 20°$, and $10 < s < 100$, and for a time these were very useful for low-precision estimates of parameters as well as insight into how their variations might affect the microwave spectrum. However, with the availability of the fast gyrosynchrotron codes of [21], which provide superior precision, apply to a much wider range of parameters, and can be applied to non-powerlaw and non-isotropic pitch angle distributions, the utility of these approximate expressions has declined in the modern era.

The observed microwave spectra and their shape have been studied for many years from the early 1960s using a few isolated frequencies [110, 41, 118] and more recently broadband emission observations [77, 69, 99]. Diagnosing a microwave flux density spectrum gives information about the emission mechanism involved and the physical parameters in the microwave source region [72, 34]. Figure 1.5 shows the universal spectra of a homogeneous source for Bremsstrahlung emission and both thermal and power-law non-thermal distributions for gyrosynchrotron emission. The spatially resolved observation of the radio source gives its brightness temperature and is expressed in the units of Kelvin [K], as shown in the top row of the figure. The corresponding flux density spectra are shown in the bottom panels. The key physical parameters such as magnetic field strength B, viewing angle to the source θ, the parameter NL with the number of electrons N above some energy limit, the path-length of the source L and the angular size of the source $d\Omega$ show variation on the spectrum with each of their change by a factor of 2 indicated by the labeled arrows in each panel of the figure [32, 9, 37].

The parameter NL of the non-thermal gyrosynchrotron case has a similar effect on the spectrum as the temperature T in the thermal gyrosynchrotron case. For example, when these parameters are increased, the spectra move up to the right, increasing the turnover frequency and the amplitude of the spectrum. The thermal brightness temperature spectra are identified with their flat optically thick slope and steep optically thin slope. The optically thin slope is directly proportional to the power-law index of the electron energy distribution.

The different parts of the flux density spectra also give information on the flare diagnostics depending on the parameters marked. The low-frequency optically thick

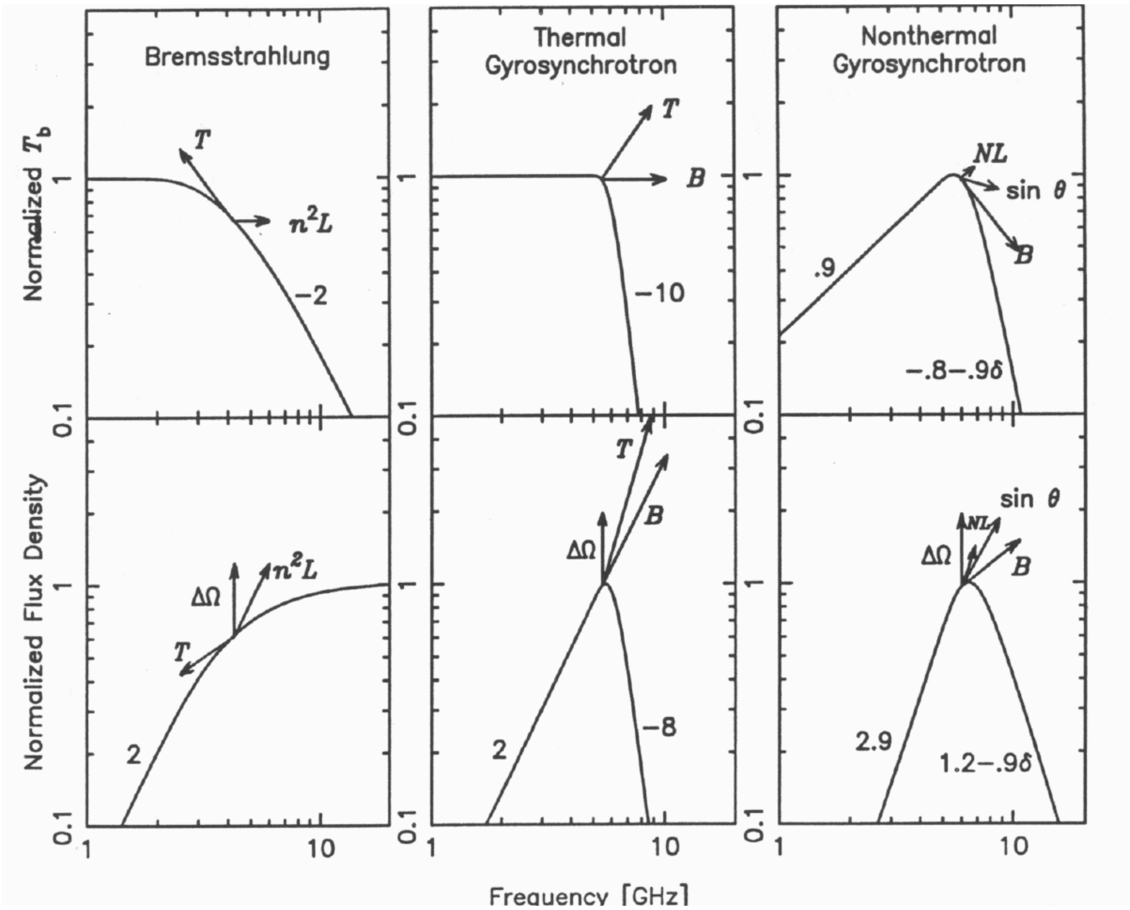

Figure 1.5 Changes on the homogeneous source spectra for the varying physical parameters. In each of the emissions, the vectors (arrows) indicate the shift in the magnitude and direction for an increase by a factor of two in the labeled parameters. Source: [32]

slope strongly depends on the magnetic field and the morphology of the emitting sources. This characteristic of the spectrum is discussed in detail in Chapter 3. The high-frequency optically thin slope of the spectrum gives non-thermal electron spectral index [55] and provides insight on the effects of pitch angle anisotropy of the electrons [24, 23]. However, effects like free-free absorption and Razin suppression can steepen the low-frequency side of the spectrum. Self-absorption is by the non-thermal electrons themselves at relatively low temperature [17, 6] and suppression of the emission by the Razin effect is due to high ambient density in the medium with refractive index less than unity [39, 96, 95, 53, 8, 22]. The flatness of the slope indicates the level of inhomogeneity and complexity in the source.

1.3.4 Gyrosynchrotron Source Morphology and Characteristics

The gyrosynchrotron emission at centimeter-wavelengths is from the energetic electrons that carry a significant amount of energy during the impulsive phase of the flare. Microwave sources due to gyrosynchrotron emmision often show complex emissions that arise from not only single magnetic loop configuration but also double-loop, or more complex loop systems [44, 87, 40, 61]. Single-loop configuration is easy to compare with the models of the gyrosynchrotron emission. Observations show that the high-frequency gyrosynchrotron optically thin emission usually concentrates at the footpoints of the flaring loop. In contrast, the low-frequency emission in the optically thick regime is distributed over the loop, and looptop [7, 86, 68, 78, 85]. This magnetic loop located in the corona has a strong field at the footpoint that becomes weaker towards the looptop. At a given frequency, the harmonic number of the emission is low at the footpoints and high at the looptop. The energy of electrons emitting at a frequency ν is $E \propto (\nu/\nu_B)^{0.5} = s^{0.5}$ [5]. Therefore, electrons with high energy emit at the looptop, and low energy emits at the footpoints. As per Equation (1.3.3), a strong magnetic field at the footpoints is favorable for high-frequency emission, and similarly, the emission at the decreasing frequencies is anticipated from the flaring loop and looptop. A few studies have also shown optically thin high-frequency emission with maximum close to the loop top of the flaring loop, and this can be due to the transverse pitch angle anisotropy of the particles injected in the loop [64, 80]. From a few briefly available microwave observations (from instruments like OVSA, VLA, SSRT, RATAN) and NoRH high-frequency observations, the gyrosynchrotron sources have shown quantitative changes of their spatial extent and polarization as a function of frequency and time.

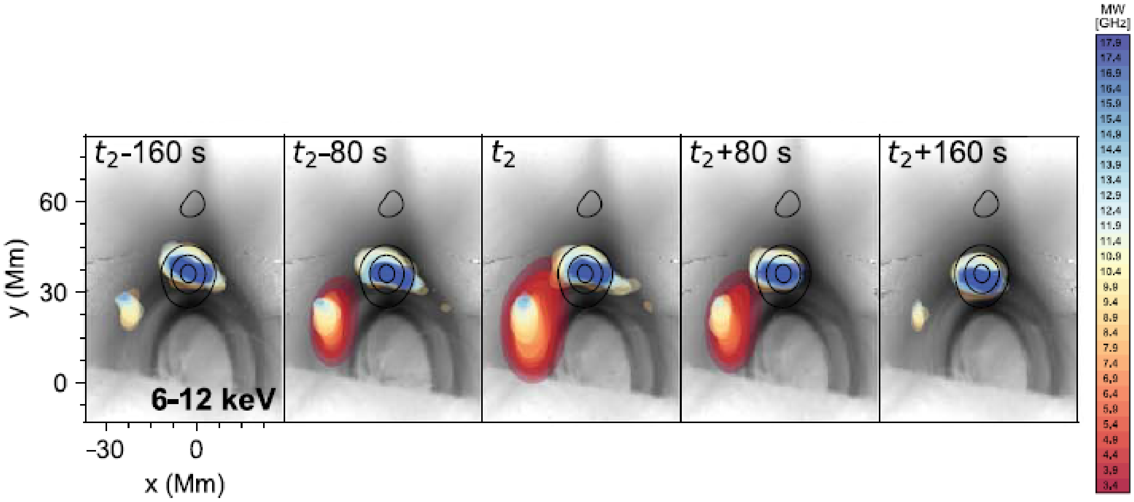

Figure 1.6 Spatial evolution of the gyrosynchrotron sources observed by EOVSA in 2.5 to 18 GHz. The sequence shows the looptop and loop leg emissions at different frequencies (represented by the colors) for 40% of peak brightness during the selected time interval together with the RHESSI 6–12 keV X-ray black contours overlaid on SDO/AIA 131 Å images.
Source: [121]

Evolution of source morphology as a function of frequency Some previous studies in the gyrosynchrotron cm-wavelengths have shown that the size of the gyrosynchrotron sources usually decreases with increasing frequency at a given time during the burst [33, 116, 56, 60]. In general, the characteristic full width half maximum of source size changes with frequency roughly as $d_{FWHM} \propto \nu^{-1}$ [5]. This change in the overall size is attributed to the inhomogeneities of plasma density, magnetic field strength, and electron energy distribution [54, 105].

Variation of source morphology as a function of time Once again, using rare observations of gyrosynchrotron cm-wavelength sources, some studies have shown temporal evolution of the source morphology. For example, in [32], the one-dimensional size of the source changed from 4 arcsec to ∼12 arcsec. This variation of source morphology can be attributed to the changes in the physical parameters of the energetic electrons. These changes in the parameters can be the magnetic field variation during the flare reconnection, changes in opacity along the line of sight (LOS), or differences in the energy distribution and number density of the energetic electrons. Sources evolve by appearing at different locations of the flare site over the duration of the burst, which is interpreted as the effect of magnetic flux emergence, small reconnection events in the case of preflare activity studies [101, 28]. [65] have shown variations in non-thermal and thermal emissions in the early impulsive and gradual phases of the flare. In addition, changes in the primary emission and/or absorption mechanism can also play a role in the source morphology variations. Most recently, Figure 1.6 shows one of the flares observed by EOVSA that shows the evolution of the gyrosynchrotron sources having high-frequency emission from the looptop and most of the low-frequency from the loop leg region.

1.3.5 Gyrosynchrotron Sources in Low-Frequencies

Very little is known about the low-frequency (LF) sources and their involvement in the flare process, mainly due to the limitations of the radio instruments over the past decades of observations. Some of the previous single frequency observations (see Figure 1.7) have shown that these LF sources are exceptionally large compared to the frequently observed high-frequency sources.

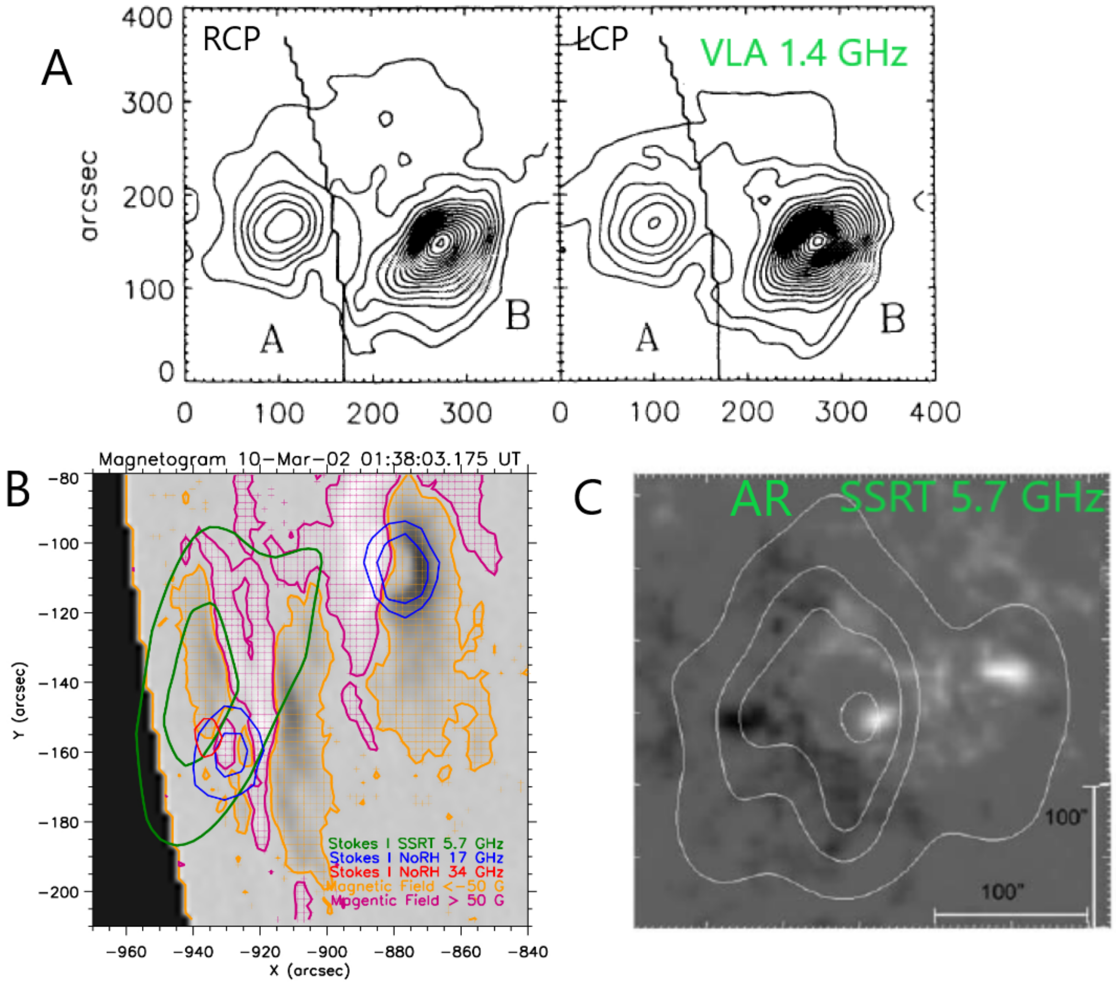

Figure 1.7 Gyrosynchrotron sources in the cases of flare and quiet Sun single-frequency observations. (A) Contours of flare sources for two polarizations were observed by VLA 1.4 GHz. (B) Contours of flare emission at 5.7 (SSRT), 17, and 34 (NoRH) GHz overlaid on SOHO/MDI magnetogram. (C) SSRT 5.7 GHz intensity of the non-flaring halo source over the active region on SOHO/MDI magnetogram.

Source: [60, 26, 50]

The limited resolution and data availability did not allow tracking the flare-based emission over the entire gyrosynchrotron frequency band. In order to resolve these LF sources one needs simultaneous high spatial, spectral and temporal resolution from the radio telescope. These challenges can now be addressed after the recent development of EOVSA, which provides a higher number of baselines with simultaneous high spatial, spectral and temporal resolution. Its large bandwidth, and capability to image every frequency-time bin with high resolution in the dynamic spectrum makes it highly appropriate to such studies.

Additionally, the simplified approximation of a single homogeneous source for gyrosynchrotron emission does not take into account the inhomogeneity in the sources observed in most flares. That means the low-frequency slope which is an indicator of the source morphology does not match with the expected slopes from the homogeneous theory. The current study reports and investigates a number of events with flux density spectra consisting of low-frequency spectral slopes that are much flatter than the expected ones.

1.4 Scientific Goal and Dissertation Outline

The advent of solar instruments like Yohkoh, RHESSI, and NoRH has changed our perspective of solar flares, supporting the standard 2D solar model discussed in Section 1.2.1. Recently, flare observations from EOVSA have provided additional observational evidence in association with the standard solar model [30, 20, 121, 15, 14]. As mentioned above, in the handful of studies/observations of the Sun at lower frequencies that have been made in the past, the flare sources cannot entirely be explained by the traditional standard flare model. These sources show extended emission around the main flaring site, which is not seen in any other wavelength observations. This brings up questions like:

Do we need a revised 2D solar flare model?

Can the double-loop 3D flare models created by using the high-frequency microwave and other wavelength observations still fit the LF sources observed in some of the flares from the recently upgraded EOVSA instrument?

Before addressing these broad questions, this dissertation addresses the following research questions about the LF flare sources:

- How commonly do the large LF flare sources occur, and what are their characteristics with time and frequency?
- Are these sources exceptionally large in size?
- Given the extended and complex structures at LF, and confined structures at HF, can these sources still be explained by the standard flare model? If not, why? And what can we infer from them?
- How the flare conditions such as acceleration and transport of high-energy electrons can be explained for these sources?

The objective of this dissertation is to address these questions by focusing on the spectral and spatial behavior of the gyrosynchrotron emission source during flares using EOVSA and other multi-wavelength observations.

Organization of the Dissertation

This dissertation is organized as follows:

- Chapter 2 gives the various data-sets, and analysis methods used in this research.
- Chapter 3 discusses the case study of the flat flux density spectral events to understand the low-frequency sources and their morphology using EOVSA radio data from the year 2015.
- Chapter 4 presents the study with EOVSA imaging spectroscopy of the large microwave flare sources with their physical and spatial characteristics.
- Finally, Chapter 5 discusses the conclusion, summary as well as ideas on future work.

Chapter 2

DATA AND METHODS

2.1 Ground and Space-based Observations

2.1.1 Expanded Owens Valley Solar Array (EOVSA)

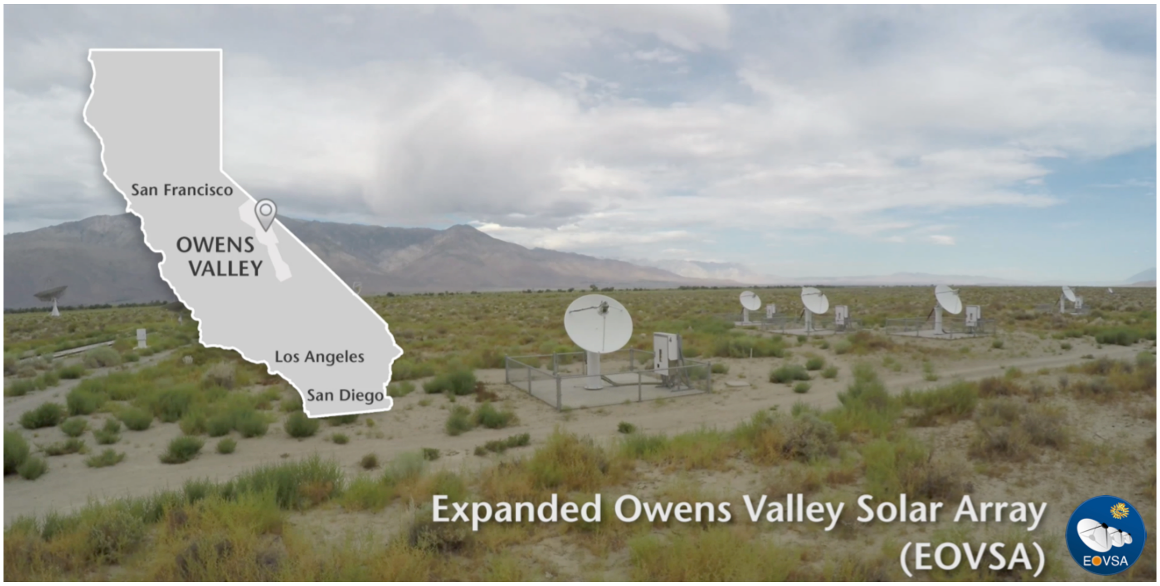

Figure 2.1 Completed array of EOVSA layout showing the central array of 2 m antennas and the 27 m antenna at a distance in the background.
Source: Dale E. Gary

The primary data used in this dissertation are the measurements from the commissioning phase and the early completion phase of the Expanded Owens Valley Solar Array (EOVSA), located near Big Pine, CA, USA [36, 30] shown in Figure 2.1. EOVSA is a solar-dedicated radio interferometer that provides imaging spectroscopy of the full Sun daily in the ∼1 to 18 GHz microwave frequency range, operated by the New Jersey Institute of Technology. It comprises thirteen 2.1 m antennas with a frequency resolution of about 40 MHz and a temporal resolution of 1 s. EOVSA uses one 27 m antenna for and calibration of the array.

During the pre-imaging commissioning phase, EOVSA observed a number of flares in total power mode only, from January to June 2015, and then added a partial cross-correlation mode (data from a limited number of baselines). During this phase, EOVSA comprised thirteen 2.1-m antennas with a frequency resolution of about 40 MHz and a temporal resolution of 1 s in the microwave frequency range of 2.5–18 GHz.

After the full expansion, EOVSA started to commission the unprecedented imaging spectroscopic capability with around 500 science channels spanning 1 to 18 GHz frequency range and two polarizations. The images have a time cadence of 1 s and have a frequency-dependent angular resolution of ∼53 arcsec (at 1 GHz) to ∼3 arcsec (at 18 GHz). As described in [89, 30], EOVSA's design is to cover the entire frequency spectrum with a few hundreds of frequency channels spanning over 34 spectral windows (spw) of 500 MHz bandwidth over the 1–18 GHz band. Currently, EOVSA is fully functional with imaging spectroscopy providing 50 spws. EOVSA upgrade specifications before and after 2019 are shown in Table 2.1.

Nobeyama Radio Polarimeters (NoRP) and Nobeyama Radioheliograph (NoRH):

Nobeyama Radio Observatory (NoRO; [83]) operated NoRH and NoRP, which are the ground-based solar dedicated radio telescope/interferometer and total power polarimeter located in Japan. They continuously observe the Sun for about eight hours daily. NoRP and NoRH are the current complementary radio observations for EOVSA data. NoRP records the total incoming flux from the full disk of the Sun in multiple microwave frequencies of 1, 2, 3.75, 9.4, 17, 35, and 80 GHz in a temporal cadence of 0.1 s [115, 83]. NoRH consists of 84 parabolic antennas and has the imaging capability to observe the full-disk of the Sun at 17 GHz (right and left polarization) and 34 GHz (total flux intensity only) with a spatial resolution of

Table 2.1 EOVSA Specifications

Parameters	2017	2019
Number of bands	31	50
Frequency range	2.84 to 18 GHz	1.1 to 18 GHz
Number of science frequencies	134	451
Instantaneous usable bandwidth	160 MHz	325 MHz
Bandwidth gaps	340 MHz	None
Frequency resolution	40 MHz	
Time resolution	1 s	
Number and type of antennas	Nine 2-m Azimuth-Elevation Four 2-m Equatorial, and One 27-m Equatorial	
Angular Resolution	57”/ν GHz x 51”/ν GHz	
Array size	1.08 km EW x 1.22 km NS	

Source: http://www.ovsa.njit.edu/

10 arcsec and 5 arcsec, respectively [83, 102, 113]. The time cadences of the NoRH observation are 0.1 s in event mode and 1 s in normal/steady mode.

Reuven Ramaty High Energy Solar Spectroscopic Imager (RHESSI):

RHESSI [73] was a space-based X-ray telescope designed for spatially resolved imaging spectroscopy of solar flares with a high spectral resolution. It measured energetic photons from SXR (∼6 keV) to gamma-rays (up to ∼ 20 MeV) with an angular resolution of 2 arcseconds for ∼4 keV to ∼100 keV energy range, 7 arcseconds up to ∼400 keV, a spectral resolution of ∼ 1 keV, and a temporal cadence of 4 s. For reconstructing the images, RHESSI allows alternate procedures like CLEAN, Maximum Entropy Methods (MEM), Forward-Fitting, and PIXON based on IDL SSW software for any combination of the time range, energy range, and detector collimators. By early 2018, only a handful of the detectors operational, having suffered radiation damage and RHESSI's energy resolution had also degraded severely. RHESSI was eventually decommissioned in August 2018. [`https://hesperia.gsfc.nasa.gov/rhessi_extras/detector_health/`, accessed on 07/27/2021].

Solar Dynamic Observatory (SDO):

SDO [91] is also a space-borne solar telescope with three instruments onboard, Helioseismic and Magnetic Imager (HMI ; [98]), Atmospheric Imaging Assembly (AIA; [71]), and Extreme Ultraviolet Variability Experiment (EVE ; [119]). The HMI provides the continuous full-disk coverage of (LOS) line-of-sight magnetic field component and the vector magnetogram of the photosphere every 45 s and 720 s, respectively, with a spatial resolution is 1 arcsec/pixel. The AIA images the full-disk solar atmosphere in 10 multiple wavelengths ranging from white-light continuum to Fe VIII line from different layers of the Sun's atmosphere with a temporal cadence of 10 to 12 s and spatial resolution of 1 arcsec.

2.2 Spectral Fitting and Modeling Methods

2.2.1 Relative Visibility Measurements

Relative visibility (RV) gives an estimate of one-dimensional source size of the burst under the assumption of a Gaussian source brightness distribution. It can be deduced from the observed visibility data measured by an interferometer, even when a lack of phase calibration prevents true imaging [32, 60, 67].

RV is the normalized Fourier transform of the observed visibility amplitudes. Mathematically, RV can be derived from the ratio of cross- and auto-correlations $\frac{x_{ij}}{\sqrt{a_{ii}a_{jj}}}$, where x_{ij} and a_{ii}, a_{jj} are the cross- and auto-correlated amplitudes respectively, for i and j antennas. Alternatively, it can be written as the ratio of fringe amplitude $v(s)$ at antenna spacing s (in wavelengths) to the total power amplitude $v(0)$, zero spacing.

For a Gaussian source with flux density $S(x) = pe^{-(x-x_0)^2/\alpha^2}$, where p is peak flux at angular position $x = x_0$, the logarithm of the relative visibility is

$$\begin{aligned} \ln(RV) = \ln\left(\frac{v(s)}{v(0)}\right) &= -9.325 \times 10^{-14} d^2 B_{\text{cm}}^2 f_{\text{GHz}}^2 \\ &= -8.393 \times 10^{-11} B_{\lambda}^2 d^2, \end{aligned} \tag{2.1}$$

where the visibility $v(s) = \int_{-\infty}^{\infty} pe^{-(x-x_0)^2/\alpha^2} e^{-2\pi isx} dx = p\sqrt{\pi}\alpha e^{-\pi^2 s^2 \alpha^2} e^{-2\pi i x_0 s}$. Therefore, a plot of logarithm of the RV as a function of square of projected baseline length (distance between each pair of antennas) produces a line whose slope is directly proportional to the size of the source at every frequency. This source size d is the one-dimensional full width at half maximum (FWHM), B_λ and B_{cm} are the baseline lengths in wavelength and cm units, respectively, f_{GHz} is the observing frequency in GHz, and s is the spatial frequency or inverse of the fringe spacing. The FWHM size d is related with the Gaussian $1/e$ width α as $d = 2\sqrt{\ln 2}\,\alpha = 1.665\,\alpha$.

Then, the slope m of the $\ln(RV)$ versus B_λ^2 plot derived from Equation (2.1), is given by

$$m(\nu) = -8.393 \times 10^{-11} \times d(\nu)^2, \tag{2.2}$$

which gives the source size in arcsec as

$$d = \sqrt{m(\nu)(-1.192 \times 10^{10})}\,. \tag{2.3}$$

Thus, from the observed visibility of a burst, relative visibility expressed as a function of frequency can estimate a Gaussian-equivalent source size at each frequency.

2.2.2 Inhomogeneous Model

To demonstrate the idea of source inhomogeneity emission, we adopt a model introduced by [49], which represents the three-dimensional (3D) magnetic field distribution with multiple sources of homogeneous components.

The model uses seven components with different magnetic field strengths and physical parameters. These components are simultaneously adjusted to generate a composite spectrum that matches the observed spectrum. The primary factors defined here for the modeling are the source area, A (perpendicular to the LOS) and the thickness, L (along the LOS) of each component using two ad hoc scaling laws: area of each segment

$$A_n = A_0\left(\frac{B_i}{B_0}\right)^{-\alpha}, \tag{2.4}$$

and thickness of each segment

$$L_i = L_0\left(\frac{B_i}{B_0}\right)^{-\beta} \text{with i } = \text{ 0 to 6} \tag{2.5}$$

The index 'i' in the Equations (2.4) and (2.5) is defined by the number of components chosen in the model. Each of these components has individual magnetic field strengths and physical parameters. The magnetic field strength value is logarithmically scaled between B_0 and B_6, with B_6 being the smallest magnetic field strength component. The gyrosynchrotron emission in terms of flux density and brightness temperature for the components in the Equations (2.4) and (2.5) is derived from Dulk's approximations [17] using Equations 13 to 17 of [19]. After defining these primary parameters of the source area, thickness, and magnetic field of the desired components, these parameters, along with a set of physical parameters, are all simultaneously adjusted to generate a composite spectrum that matches the observed spectrum.

The following two modeling tools are used in the preliminary analysis of the study in the following chapters of this dissertation.

GSFIT Package

GSFIT is an IDL SSW-based microwave spectral fitting widget graphical user interface (GUI) package. It provides an interface of gyrosynchrotron fast-fitting codes with user-friendly mapping of EOVSA image data cubes. GSFIT also functions on a command prompt mode called GSFITCP. The individual spectra can be also fit by manual investigation using this GUI application. Selected blocks of data can also be processed using parallel/multi-core batch mode. GSFITVIEW is an additional routine to further display and investigate the fitting results. This package follows the GS codes that account for gyrosynchrotron, free-free emission, and absorption and is an enhanced form over the Petrosian-Klein approximation of the GS equations [21, 31, 20, 66].

GX-Simulator

GX-Simulator is a three-dimensional modeling tool based on IDL SSW for simulating the imaging and spectral data in the gyrosynchrotron frequency range with other complementary data [88]. GX-simulator allows its users to do the following analysis.

1. Import a photospheric magnetic field map and perform extrapolations on it to generate a 3D magnetic field model,
2. Investigate the 3D magnetic field topology and interactively create magnetic flux lines and associated fluxtubes,
3. Populate those magnetic flux tubes with user-defined inhomogeneous, thermal and anisotropic, non-thermal electron populations,
4. Investigate the model generated images and spectral properties of radio and X-ray emission, and
5. Finally, compare the simulated images and spectra with the observational data.

This package also uses GS codes, integrating with soft and hard X-ray codes, potential, and linear force-free field extrapolation routines.

Chapter 3

IMPLICATIONS OF FLAT OPTICALLY THICK MICROWAVE SPECTRA IN SOLAR FLARES FOR SOURCE SIZE AND MORPHOLOGY

3.1 Introduction

During solar flares, microwave bursts generated by the gyrosynchrotron emission mechanism usually peak in 5–10 GHz frequency range [41, 77] with a transition from optically thick to optically thin emission, below and above the peak, respectively. Over the decades, microwave observations conducted predominantly at optically thin frequencies have shown that the gyrosynchrotron flare emission is of mostly compact and nearly uniform sources [79, 76]. But they tend to be larger and more complicated in occasionally observed optically thick frequencies well below the peak [116, 1, 30].

Solar-dedicated radio instruments like NoRH, operating at 17 and 34 GHz [83] have been extensively studying the high-frequency microwave flare sources. However, the LF centimeter wavelength emission is less understood due to the paucity of relevant past imaging observations. There has been relatively little research on the spatial configuration and the spectral characteristics of the LF sources in the flare process. A few previous studies based on modeling and scarcely available microwave imaging observations have reported large spatial sizes of the flare microwave LF sources [60, 25, 22, 67]. Additionally, some studies have also reported large unstructured halo sources at 3–5 GHz that are as large as the entire non-flaring active region [50, 92].

As discussed in Chapter 1, the spectral index/slope (α_l) of a gyrosynchrotron microwave spectrum in the low-frequency, optically thick side (at $\nu<\nu_p$ with optical depth, $\tau > 1$) reflects the physical parameters of the microwave source region. Studies using spectral shape and slope indices have shown that the microwave LF sources do not conform to the predicted spectra of a homogeneous source

[107, 70, 77, 49], and therefore, are generally inhomogeneous by nature. For a spatially integrated spectrum, the source inhomogeneity results in a flatter than the expected low-frequency part of the spectrum, i.e., one with a small α_l value [112]. Studies reported that these inhomogeneous sources are mainly found to have high flux densities and large source areas at low frequencies [42, 97, 54, 70, 106]. A few spectral studies have also shown that the evolution of simultaneous emission from multiple sources with different physical parameters can also result in a flat spectrum [101, 18, 55].

Most of the previous studies at low frequencies lack good frequency resolution, coverage, and imaging capability. There has been significantly less focus on the low-frequency part of the gyrosynchrotron emission, morphology, and behavior of the source of this emission during flares. However, as discussed in Chapter 2 the high-resolution observations in frequency and time from the EOVSA interferometer make the data unique and valuable for spectral-based studies. The high-frequency resolution can produce finer and better-defined slopes of the spectrum compared to earlier observations. Furthermore, having corresponding imaging observations from EOVSA for one of the events is an added advantage to validate the analysis based on the spectral behavior alone, as done in the current study.

In this chapter [1], we first address the spectral characteristics observed in a set of 12 bursts during the peak of the solar cycle 24 (in 2015). We focus on the occurrence of the flat spectra at low frequencies, and we determine the source area by analyzing the observed flux density spectra. For the frequency range of ~ 2.5 to 18 GHz, we use the calibrated total power and uncalibrated cross-correlation data during EOVSA's commissioning phase. At this early time, due to the absence of the auto-correlation data transferring the total power calibration to the cross-correlated

---

[1] This chapter is based on the following paper: S. B. Shaik, & D. E. Gary, "Implications of Flat Optically Thick Microwave Spectra of Solar Flares for Source Size and Morphology," *The Astrophysical Journal*, in Press

visibility data is prevented. Instead, we analyze the source size information inherent in the visibility data by forming a relative measure (a pseudo-relative-visibility described in Setion 3.4.2). In addition, to demonstrate the role of inhomogeneity on the flat spectrum, we implement inhomogeneous modeling to generate the observed spectrum.

3.2 Data and Methods

As discussed in Chapter 2, the primary data used in this first study of this dissertation are the pre-imaging spectral measurements from the commissioning phase. During this phase, EOVSA observed a number of flares in total power mode only, from January to June 2015, and then added a partial cross-correlation mode (data from a limited number of baselines). EOVSA had eight antennas and was running two independent copies of a prototype 4-element correlator design. During this time, the prototype correlator recorded only 12 baselines and did not produce the correct auto-correlation data. EOVSA attained full imaging capability with a 16-element correlator starting in April 2017. We include one event with imaging data (2017 September 10) to validate our methods for interpreting the earlier, less-complete data.

The total power calibration is performed based on the daily flux density measurements reported by the National Oceanic and Atmospheric Administration (NOAA) from the U.S. Air Force Radio Solar Telescope Network (RSTN) and Penticton at nine frequencies (eight from RSTN and one from Penticton). The calibration procedure is to read these daily flux density measurements, calculate the mean value at each frequency, fit a quadratic function to the fluxes at seven frequencies in the $1 - 15.4$ GHz range, and apply interpolation or extrapolation to match the EOVSA frequencies. Any pointing offsets are determined for all the antennas as a function of frequency and are used with primary beam corrections to the observed data.

Radio imaging data available from the NoRH at 17 GHz are complemented with the EOVSA data for one of the events (2015 March 10 M2.9 flare) shown here. The hard X-ray emission, which is believed to correlate with the microwave emission from the closely related electron population, is obtained from RHESSI for spatial comparison. In addition, for determining the configuration of the photospheric and coronal magnetic fields in the flaring region, the extreme ultraviolet (EUV) images from AIA instrument and magnetograms from HMI onboard the SDO spacecraft are correlated.

The set of 12 bursts analyzed in this study is listed in Table 3.1. Most bursts have a short burst duration ranging from 1 minute to 6 minutes and smooth time evolution of the flux density spectra. For a burst observation, each antenna measures the same total power spectrum independently. The median over the operating antennas is utilized to arrive at a single dynamic spectrum of the burst. The standard deviation among antennas is used as a measure of instrumental uncertainty.

Each burst in the list is processed for flagging bad antennas, background subtraction, flux calibration, and corrections for temporal discrepancies in the data for a few bursts. Then the spectral fitting is performed on the observed spectra for the whole duration of each burst. This fitting provides a reliable set of parameters for a large number of time points at each frequency from the given high time and frequency resolution of EOVSA. The parameters are obtained from the procedure as described and introduced in [107]. The functional form of this procedure for the flux density is written as

$$S(\nu) = A\nu^{a}(1 - e^{-B\nu^{-b}}). \tag{3.1}$$

This equation for the generic shape of the gyrosynchrotron microwave spectrum provides a positive slope at low frequencies (optical depth, $\tau > 1$), reaches a peak flux density (ν_p, peak frequency in the range 5 to 10 GHz) and forms a negative slope at high frequencies ($\tau < 1$). At low frequency, the term $e^{-B\nu^{-b}}$ becomes negligible with coefficients B and b making $(1-e^{-B\nu^{-b}}) \approx 1$. Therefore, the low-frequency slope (α_l) of the microwave spectrum is represented by the parameter a. Similarly, the other parameters deduced from the equation are high-frequency slope ($a-b$), peak flux $S(\nu_p)$, and peak frequency ν_p. This generic functional fitting is carried out on each 1 s of observed spectrum for the events in Table 3.1, thus providing the temporal evolution of all the parameters.

Furthermore, the spatial components of the microwave sources are determined from the technique of relative visibility discussed in Chapter 2. Section 3.4.2 discusses the relative visibility and the resultant source size calculated at each frequency from the observed visibility of the bursts .

3.3 Observations

3.3.1 Spectral Index and Flat Spectra

The low-frequency optically thick spectral index α_l, as discussed in Section 3.1, is a sensitive parameter of the microwave burst spectrum that indicates the source spatial characteristics as a function of frequency. This slope and the shape of the non-thermal gyrosynchrotron radiation spectrum are conveniently defined by numerical approximations to the theory [19, 17] for an isolated homogeneous source. The relationship between the brightness temperature T_b, the effective temperature of the radiating electrons T_{eff}, and the emitted flux density S of the radio source are given in the following equations for the optically thick regime:

$$T_b = T_{\text{eff}}, \tag{3.2}$$

$$T_{\text{eff}} = 2.2 \times 10^{9-0.31\delta} (\sin\theta)^{-0.36-0.06\delta} \left(\frac{\nu}{\nu_B}\right)^{0.5+0.085\delta}, \tag{3.3}$$

Table 3.1 List of Selected Bursts Observed by EOVSA

EOVSA events						
Event Number	Date	GOES Class	Start Time (UT)	Active region configuration	NOAA region	Peak flux (SFU)
1^*	Mar 10, 2015	M2.9	23:46	$\beta\gamma\delta$	12297	1338
2^*	Mar 12, 2015	M2.7	21:44	$\beta\gamma\delta$	12297	548
3	Apr 21, 2015	M2.0	16:55	β	12322	97
4	Apr 21, 2015	M1.8	21:39	β	12322	31
5^*	May 5, 2015	X2.7	22:05	$\beta\gamma$	12339	1441
6^{**}	Jun 21, 2015	M2.0	01:02	$\beta\gamma\delta$	12371	1252
7	Aug 22, 2015	M3.5	21:19	$\beta\gamma$	12403	985
8^*	Aug 24, 2015	M1.0	17:40	$\beta\gamma\delta$	12403	256
9	Aug 24, 2015	C3.0	22:40	$\beta\gamma\delta$	12403	253
10	Sep 24, 2015	C3.3	23:41	α	12418	76
11	Sep 27, 2015	C4.2	17:41	$\beta\gamma\delta$	12422	388
12^*	Sep 27, 2015	C9.3	19:44	$\beta\gamma\delta$	12422	126

Note: Asterisks mark the flat spectral events and the double asterisk marks event 6 with flat spectrum only in the peak phase. (sfu, solar flux unit is a measure of solar radio flux density; 1 sfu = 10^4 Jy = 10^{-22} $\mathrm{W\,m^{-2}Hz^{-1}}$).

where ν and ν_B are the observed frequency and gyrofrequency respectively, θ is the viewing angle and δ is the electron spectral index. In addition, the total power flux density is the brightness temperature integrated over the source as given in Equation (1.7) and T_b is equal to the effective temperature for the optically-thick emission as in Equation (3.2).

For the typically observed values of δ in the range of $2 \leq \delta \leq 7$ and from the Equations (3.2) to (1.7),

$$S(\nu) \propto \nu^{2+x}$$

with $0.75 \leq x \leq 1.095$.

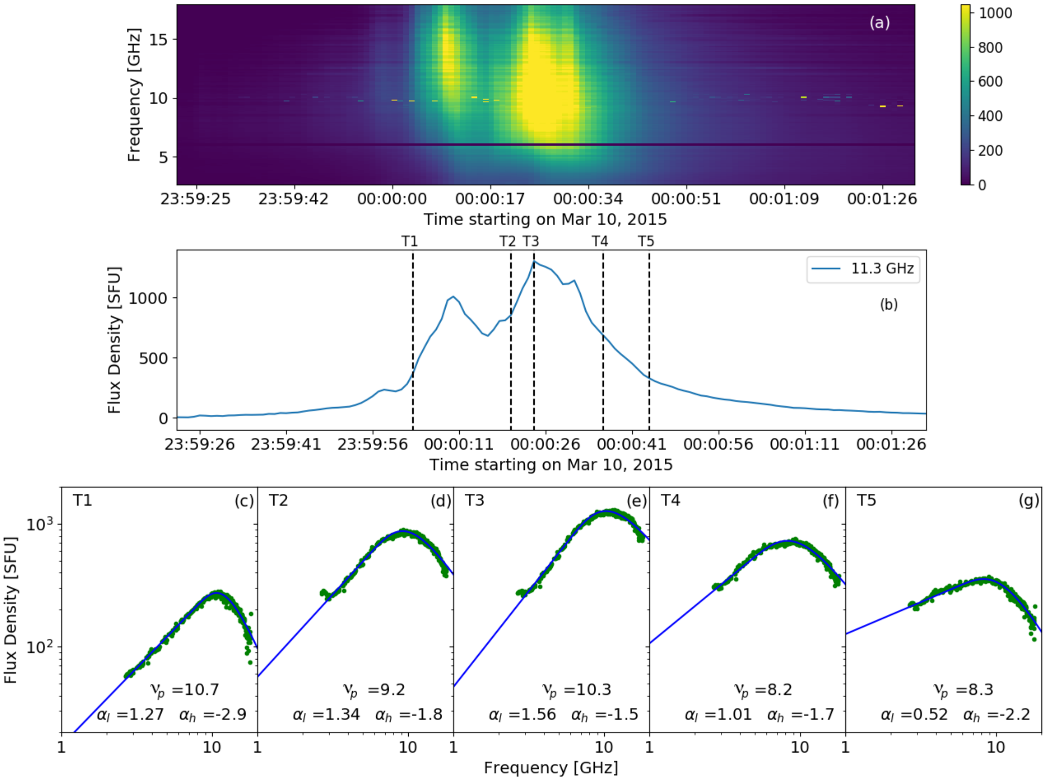

Figure 3.1 Microwave spectral evolution of the 2015 March 10 event. (a) Total power median dynamic spectrum for the frequency range 2.5–18 GHz.
(b) Time profile at 11.3 GHz (near the burst peak frequency). (c to g) Spectra for the five times, T1, T2, T3, T4, and T5 marked in (b) with vertical dashed lines. T1 and T2 are chosen for the rise phase of the pre-peak (00:00:09 UT) and the main peak (00:00:24 UT), respectively. Spectral fit parameters are noted at the bottom of each panel.

Therefore, for a single homogeneous burst source, one would expect the observed flux density spectrum to have an optically thick slope $\alpha_l \approx 2.75$–3.1 for $\delta \approx 2$–7. The average α_l of this relatively small range can thus be taken as typical value for a homogeneous source,

$$S(\nu) \propto \nu^{2.9}. \tag{3.4}$$

Any value of the slope far from this range indicates some peculiarity in the characteristics of the source. Steeper spectra, $\alpha_l \geq 3.1$ can only be due to Razin suppression or absorption by a different source of cooler, intervening plasma [95, 6]. Shallow/flat spectra with $\alpha_l \leq 2.75$ indicate spatial inhomogeneity of the source emission. Therefore, examining the low-frequency spectral index of the gyrosynchrotron spectrum provides a sensitive means to reveal complexity in the source morphology.

Note that $\alpha_l \approx 2.9$ is for a non-thermal distribution of electrons. Emission from a hot ($T \sim 10$ MK) thermal distribution can produce a low-frequency slope of 2 but, for a homogeneous source, it would also produce an extremely steep high-frequency slope [32]. Since the bursts in Table 3.1 do not show such steep high-frequency slopes and have low-frequency slopes shallower than 2, we interpret the emission as non-thermal and inhomogeneous.

Initially, all the events in Table 3.1 are analyzed for the low-frequency index α_l of their spectra. The procedure is illustrated in Figure 3.1, which gives the overview of the first event, 2015 March 10 in Table 3.1. Figure 3.1a shows the total power dynamic spectrum over a 2 minute period, while Figure 3.1b shows the flux density time profile at the peak frequency, 11.3 GHz. The corresponding flux density spectral evolution is shown in Figure 3.1c–g. The vertical dashed lines in Figure 3.1b indicate five times in the burst—2 times during the rise phase, the peak time, and two times in the decay phase—selected for the spectra shown in Figure 3.1c–g and designated as T1 to T5.

For each time, the spectral fitting is applied using the Stähli equation as discussed in Section 3.2. The fitting parameters, low-frequency index α_l, high-frequency index α_h, and peak frequency ν_p are marked at the bottom of each spectral plot.

In Figure 3.1c–g, the main point of interest of this study, the low-frequency spectral index always remains well below the theoretical value of around 2.9 predicted for a homogeneous source by Equation (3.4). This low index value is observed to be more pronounced in the decay phase of the burst. Additionally, in agreement with the previous studies [70, 77], the peak frequency ν_p clearly increases in the rise phase (T2 to T3) and decreases during the decay phase, which is an indicator [77] that the peak is controlled by optically thick gyrosynchrotron emission.

To statistically examine α_l and its evolution over the duration of the bursts, the time profiles of α_l for all 12 events are determined in the same manner. Figure 3.2 shows α_l over the duration of six of the bursts selected for their representative trends. In each panel, the spectral index is plotted in red (scale on the right side of each plot) and the flux density at the peak frequency in blue (scale on the left). The error bars in the spectral index curves are calculated from the standard deviation over the neighboring 5 s (5 data points).

The overall behavior of the plots illustrates three types of α_l evolutionary trend. In the first type, as shown in Figure 3.2a and b, α_l starts to decrease before the peak and continues to drop into the decay phase except for a slight, short-duration increase near the peak. During the late decay phase, α_l shifts back to higher values. For example, in the 2015 March 10 event shown in Figure 3.2a the index starts with a value of ~ 3 in the rise phase then smoothly reduces to a value of 1 at peak and eventually decreases almost to 0 in the decay phase. In the second type (Figure 3.2c and d), α_l shows a sharp decrease at the peak and increases in the early decay phase. In the third type of α_l evolution, shown in Figure 3.2e and f, the spectral index follows

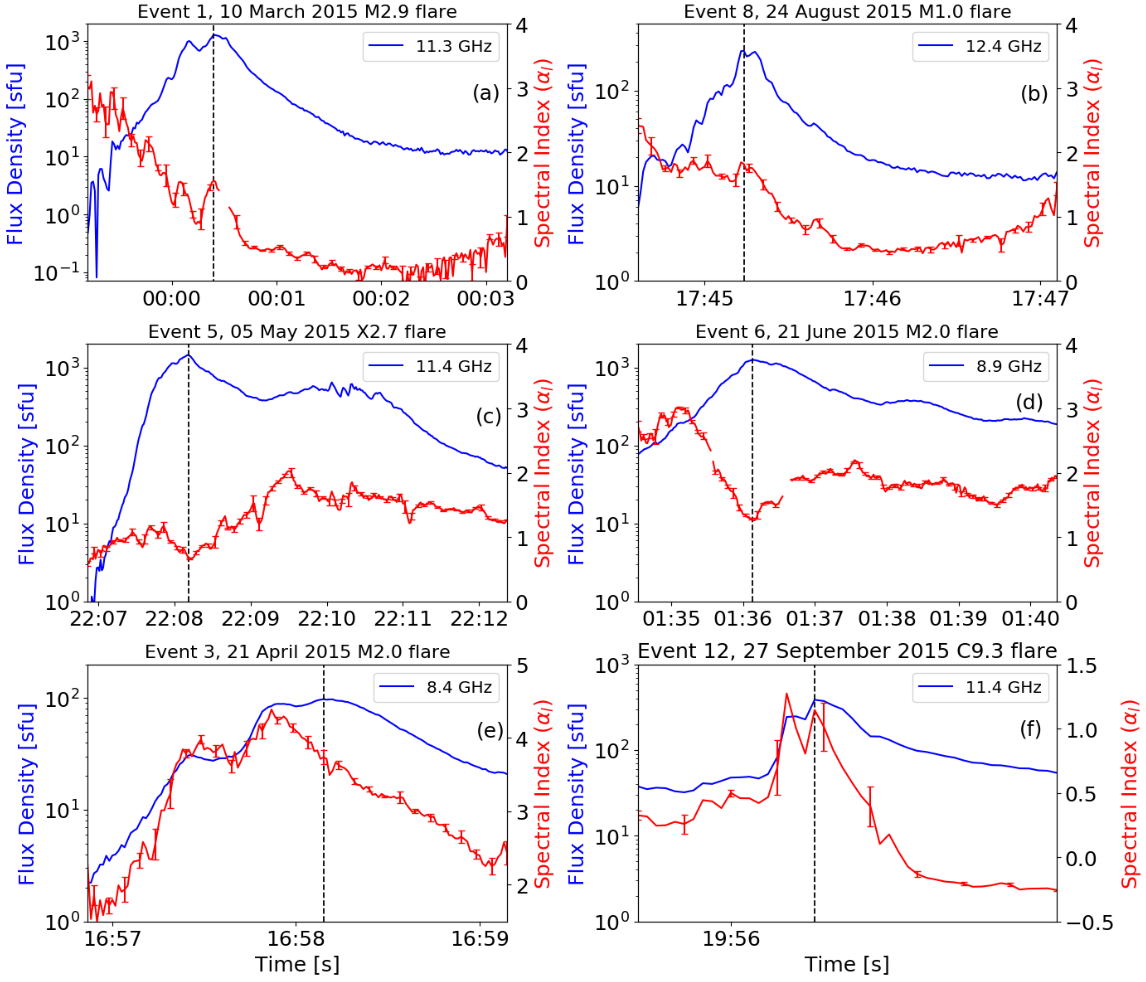

Figure 3.2 Spectral index evolution of the six representative events for the whole duration of the bursts (red). The corresponding flux density time profile are plotted in blue color. Note that the time profiles are plotted in logarithmic scale in y-axis.

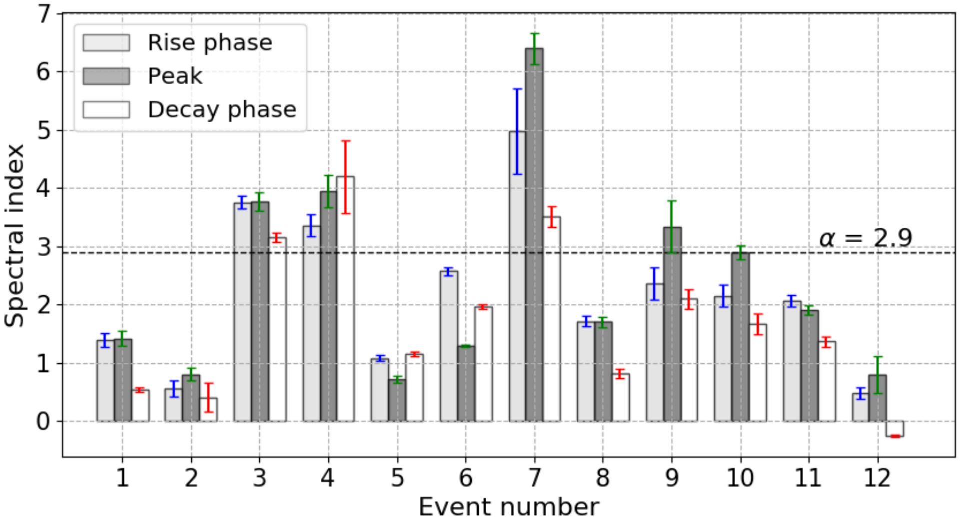

Figure 3.3 Bar chart of spectral index for the events in Table 3.1. In each event, the spectral indices are shown at each of the rise, peak and decay phases (see text for details). The homogeneous source model spectral index of 2.9 is marked as a black dashed horizontal line.

the same trend as the flux density, growing steeper during the rise phase and dropping rapidly after the main peak and in the decay phase.

To better compare the behavior of the spectral index over all the events, Figure 3.3 presents a bar chart for the trend of α_l versus each event number listed in Table 3.1. The chart reports the indices averaged over a 10 s period in the rise phase, peak, and decay phase of each event (e.g., at times T1, T3, and T5 in Figure 3.1 corresponding to each phase). The rise phase for a given event is defined as the time when the flux density first reaches 10% of the maximum, while the decay phase is at the same flux density during the decay. The theoretical homogeneous source spectral index of ∼2.9 is marked by the horizontal dashed line. Note that the α_l value in each phase of the burst differs slightly from the value shown in Figure 3.1 for the 2015 March 10 event due to the averaging of the ten values in each corresponding phase in Figure 3.3. The error bars are the standard deviation of fluctuations in α_l during each 10 s period.

The observations of the chart are summarized as follows.

1. *Index evolution:* Over the evolution of the burst, the spectral index decreases from peak to decay phase for nine out of the 12 events (Event numbers 1–3, 7–12).

2. *Index value:* Compared to the theoretical value, most of the events have α_l below 2.9. Nine of the events have spectral indices less than 2.9 in at least one of the three phases or all the phases of the burst (Event numbers 1, 2, 5, 6, 8–12). In particular, five of them (1, 2, 5, 8, and 12) show extreme spectral index values < 1 in at least one phase of the burst, which we henceforth define as flat events.

3. Contrary to that suggested in earlier studies, flat low-frequency spectral indices are not limited to large, high-flux-density (X-class) flares [42, 97, 70] but can also appear in a relatively weak C9.3 flare (event 12) with a low peak flux ~ 125 sfu.

4. All the events but one (event 5, the sole X-class flare in our list) that show flat indices originate from active regions with a complex magnetic configuration of $\beta\gamma\delta$ as seen in Table 3.1.

5. The variation of the spectral index within an event is generally smaller than between the events. An event with either a large or small index maintains similar values during its evolution.

Interpreting these points in terms of the homogeneity of the emitting source, a very low value of α_l signifies that the emission is from a highly inhomogeneous source. The area/emitting volume of this source grows with decreasing frequency due to the non-uniform physical parameters within. The declining value of α_l with time in some events suggests that the inhomogeneity and the complexity of the burst source grow as the flare evolves with time.

This spectral index analysis leads to a representative set of 5 events (42% of our sample) that have a flat ($\alpha_l < 1$) spectrum, which is further investigated for additional evidence of source inhomogeneity in the next section.

3.4 Results and Discussion

3.4.1 Source Area Spectrum

The microwave flux density as a function of frequency $S(\nu)$ for a simple homogeneous source as mentioned in Equation (1.7) can be written as

$$S(\nu) = \frac{2k\nu^2 T_b(\nu)}{c^2}\Omega(\nu) \quad [\mathrm{Wm^{-2}Hz^{-1}}]. \tag{3.5}$$

At the observed frequency ν, for a constant brightness temperature T_b, the emitted flux density $S(\nu)$ is directly proportional to the solid angle area of the source $\Omega(\nu)$ (Ω as a function of ν emphasizes that the source area indeed depends and changes with frequency). We expect that most of the flares observed in microwave emission exhibit some level of inhomogeneity, leading to an increase in source area with decreasing frequency. The flat events that we have identified require an extreme rise in size and hence inhomogeneity.

Equation (3.5) can be rewritten following Equation (4) in [27, 22] as

$$A \approx 137\,\frac{S(\nu)[\mathrm{sfu}]}{\nu_{\mathrm{GHz}}^2}\left(\frac{10^8\,\mathrm{K}}{T_b}\right), \tag{3.6}$$

where A is the area in square arcsec, the constant applies when the flux density is expressed in sfu, and the frequency is in GHz. Note that the constant factor is corrected and is different from the equation in [27, 22] due to an over-simplification in their expression (Fleishman, private communication). As discussed earlier, the non-thermal brightness temperature for the optically thick part of the spectrum is equal to the effective temperature, $T_b = T_{\mathrm{eff}}$. Observations show that the effective temperature during large flares is typically quite high; thus, the last term is of order unity. If we assume a fixed, frequency-independent value for the effective temperature ($\gg 10^7$ K), we can obtain an approximate representation of the source area spectrum for the optically thick regime of the observed flux density. For a given spectrum, according to Equation (3.4), $S \propto \nu_{\mathrm{GHz}}^{\alpha_l}$. Therefore, Equation (3.6) leads to the source area $A \propto \nu_{\mathrm{GHz}}^{\alpha_l - 2}$.

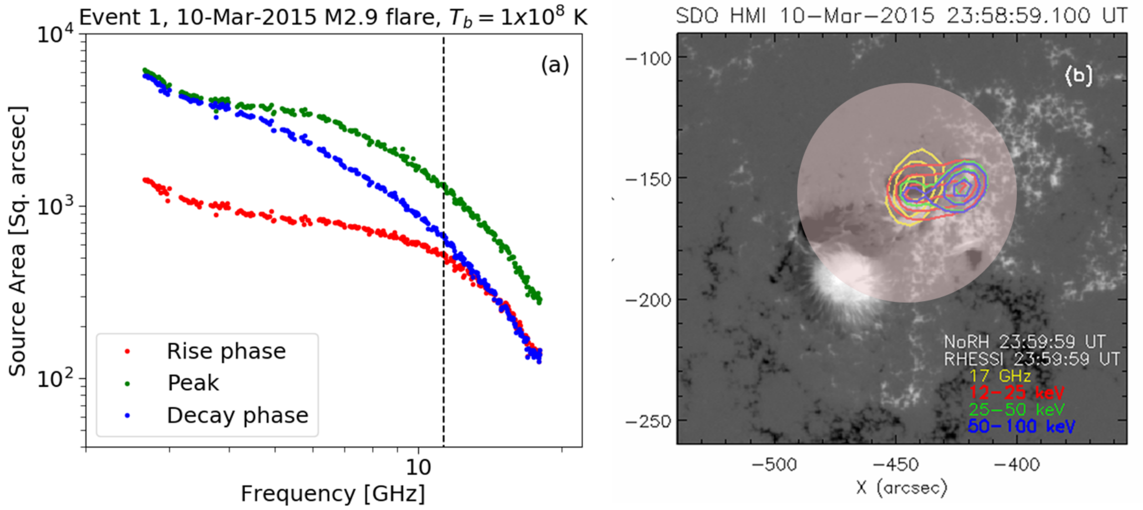

Figure 3.4 Source area spectrum at each phase of the burst and the image map of the flare sources at the peak time. (a) The source area calculated for a given brightness temperature is marked in red, green, and blue for the three phases. The peak frequency, 11.3 GHz, is marked by the vertical dashed line to separate optically thick and thin parts of the spectrum. (b) NoRH and RHESSI flare emission at 50, 70, 90% of their corresponding maximum fluxes are plotted over the HMI magnetogram at the burst peak time. The masked region shows the equivalent circular microwave source area cartoon for 2.9 GHz.

As an illustration, Figure 3.4a shows the source area spectrum of the 2015 March 10 burst, whose α_l varies from 1.3 to 0.5 over the burst duration. For the observed EOVSA flux density, we assume a constant and high brightness temperature of 10^8 K and calculate the source areas as shown in the figure. The three curves are the areas measured for the times selected in Figure 3.1 (T1, T3, and T5) at the rise phase, peak, and decay phase, respectively. These source size estimates are valid for the optically thick emission well below the spectral peak, shown by the vertical dashed line. In the peak (green) and decay phase (blue) curves, at the low frequencies ~ 2.9 GHz, the source areas are ~ 6200 and ~ 5500 arcsec^2, respectively. The area spectrum for both the peak and decay phase is relatively flat until ~ 4 GHz and then decreases more steeply in the decay phase from frequencies above ~ 4 GHz. For the rise phase (red) curve, the source area starts smaller than the other two phases, at $\sim$ 1500 arcsec^2. However, this size would be larger if we make the reasonable assumption of a variable effective temperature, starting from a lower value and increasing with time towards the peak of the burst. Following the source area at one frequency, say 3 GHz, the rise phase area starts with a large value and grows still larger in the peak and decay phase.

According to Equation (3.6), for the case of a flat spectrum with $\alpha_l \approx 0.5$, the source area goes as $A \propto \nu_{\mathrm{GHz}}^{-1.5}$. For example, in the decay phase, a moderate-sized source with area $\sim$ 900 arcsec^2 at $\nu_p \sim$ 10 GHz must grow to an area of $\sim$ 5000 arcsec^2 at 3 GHz. For the range of spectral index values α_l observed in this event, the power-law index n in $A \propto \nu_{\mathrm{GHz}}^{-n}$ ranges from 0.7 to 1.5.

At 2.9 GHz, the area for the peak time gives a diameter of $\sim$ 89 arcsec assuming a circular shape of the source (light gray circle in Figure 3.4b). For comparison, the high-frequency NoRH microwave 17 GHz images and the RHESSI Hard X-ray (12–25, 25–50, and 50–100 KeV) sources at the burst peak time are overlaid on a HMI magnetogram as shown in the figure. So, even with our assumption of a high brightness temperature, the estimate of the low-frequency radio source size is many times greater than the 17 GHz and the hard X-ray sources (which themselves may appear larger than they are due to finite resolution). The actual brightness temperature in the flaring site, if not as high as the assumed T_b, will only lead to a much larger source.

As the emission is optically thick over its volume, these source area measurements characterize the actual area of the source magnetic structure. The changes observed in the area spectrum can be caused by gradients in the magnetic field strength and density [54, 60, 4, 22] that result in spatially-dependent changes in opacity. The fact that the flux density spectrum becoming flatter with time and the source area spectrum becoming steeper indicates that the sources grow significantly large with decreasing frequencies. Such large sources cannot be homogeneous but have to be non-uniform and inhomogeneous in the flare site. This line of reasoning with inhomogeneity is further discussed in Section 3.4.3.

We have performed a similar analysis on all the other events and verified that the flat events exhibit the same trend of large areas. We now seek confirmation of these estimates by indirect interferometric measurements via the relative visibility technique described earlier. Before doing that, however, in the next section, we examine the RV technique by comparing its results with the direct EOVSA imaging of source sizes available for the 2017 September 10 event [30].

3.4.2 EOVSA Relative Visibility Analysis

As discussed earlier, relative visibility is a sensitive measure of source size and complexity for a flare microwave emission using the observed visibility amplitudes. For a Gaussian source, RV amplitude vs. baseline length shows a smoothly decreasing shape depending only on the source size [32]. For an extended source, RV is unity at short baselines and decreases with increasing baseline length. Generally, short baselines cannot resolve a single Gaussian source; therefore, cross and auto-correlated data will have almost the same flux density leading their ratio to be unity. When sources become resolved at longer baselines, the cross-correlated data has less power leading to the RV ratio gradually decreasing from unity. Any deviation of the source from a Gaussian shape will modify the manner in which the RV ratio decreases, but the initial drop at short baselines is expected to measure the size of an equivalent Gaussian shape.

2017 September 10, X8.2 class Flare

The 2017 September 10, X8.2 class west limb flare is one of the largest flares in solar cycle 24 that occurred in the active region AR 12673 [30, 90]. The time profiles of the microwave burst at three selected frequencies and the total power dynamic spectrum are shown in Figure 3.5a and 3.5c, respectively. This event is a long duration burst extending for more than an hour with a gradually evolving rise phase and a long decay phase. The black dashed vertical line in Figure 3.5a marks the time of the 8.95 GHz peak used for the relative visibility analysis. Figure 3.5b shows the flux density spectrum for this time with the fitting procedure of the curve as in Figure 3.1. The spectral index α_l and peak frequency ν_p are marked at the bottom of the panel. Although not important for the RV validity check, we remark that this event is intermediate between a homogeneous ($\alpha_l = 2.9$) and a flat spectral type ($\alpha_l < 1$) with α_l changing from 1.9 to 1.4 over the time shown in Figure 3.5a. At the chosen time, the spectrum shows broadband emission with the spectrum still rising at 18 GHz, which implies that the peak frequency would have occurred beyond 18 GHz.

Using the cross- and auto-correlated data relation for RV, the logarithm of RV (blue dots) versus square of baseline length (B_λ^2) at the selected time is shown in Figure 3.5d. As noted above, the approximately linear decrease in $\ln(RV)$ at short baselines is the behavior expected for a Gaussian source, whose fitted slope (green dashed line) provides an estimate of source size as per Equation (2.2). This procedure can be repeated at each of the 30 frequency bands available in the data to create a source size spectrum. However, Figure 3.5d shows that after following the line for several e-foldings, the points begin to deviate from a single slope at longer baselines. To examine this non-linear distribution of RV amplitudes at longer baselines, we obtain the alternative RV (red curve) directly from the available EOVSA images for this event shown in Figure 3.5e. The contours are for a subset of available frequencies at the selected time overlaid on the bright AIA 171 Å EUV loops.

The image RV (red curve) is obtained from the visibility space by taking the Fast Fourier Transform (FFT) of the image map. The RV is calculated for the row of pixels along the FFT plane's horizontal axis (referred to as EOVSA map RV_x), with the zeroth element used to supply the zero spacing intensity needed in Equation (2.1).

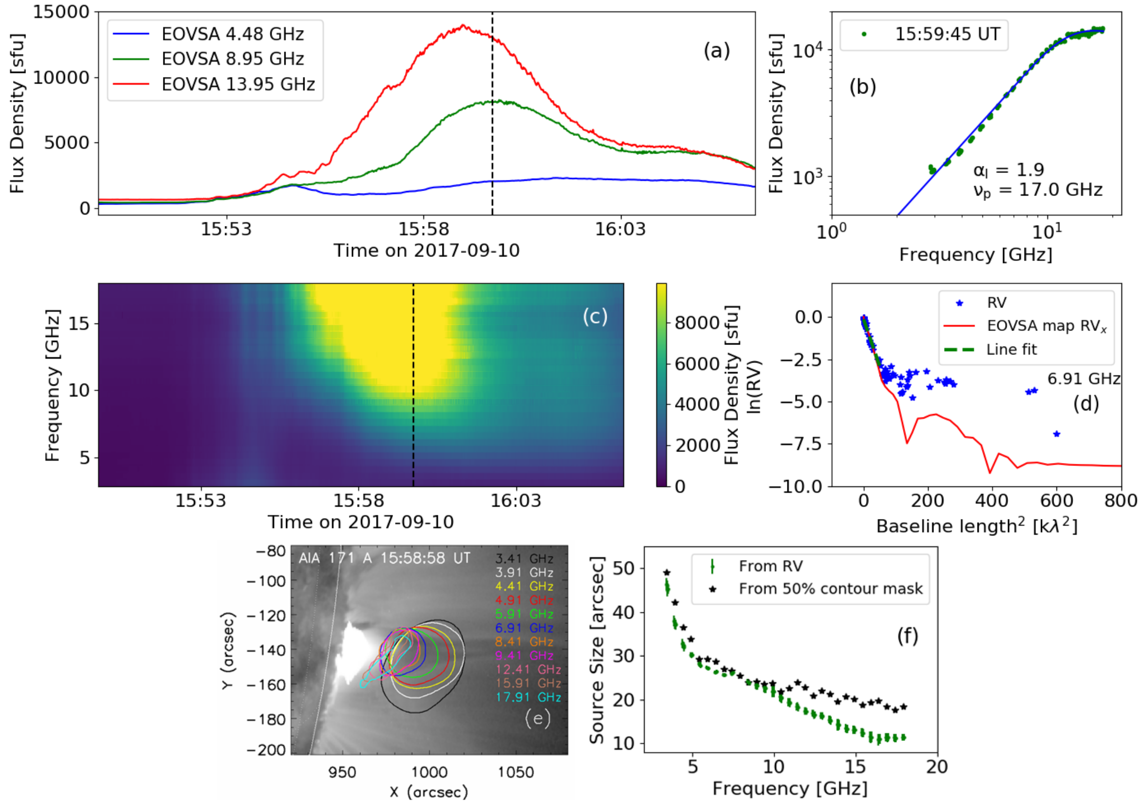

Figure 3.5 Relative visibility and source size analysis at 15:59:05 UT around the peak of 2017 September 10 X8.2 flare at the three given frequencies. (a) to (c): Time profiles, flux density spectrum at the peak time (with α_l and ν_p marked at the bottom of the plot), and median total power dynamic spectrum of the burst. (d) $\ln(RV)$ versus B_λ^2 plot at the peak time for 6.91 GHz with a linear fitting marked in green. RV calculated solely from the observed EOVSA image maps is in red. (e) The 50% contours of peak flux density of EOVSA images at the given frequencies are overlaid on AIA 171 Å EUV map. The solar limb is marked in white. (f) Source size spectrum deduced from the relative visibility slopes are plotted in green and the images in black. The error bars on the green symbols are the uncertainties of the fitting coefficients calculated from the covariance matrix from the fitting procedure.

When plotted to the square of baseline lengths at 6.91 GHz, these relative visibilities resemble the true RV, and both show a dip near 120 kλ^2 (with a small dip $\sim$ 35 kλ^2) and a maximum near 200 kλ^2. We interpret this as evidence for a tendency of the source to have a more uniform surface brightness and sharper edges than a true Gaussian source so that its FFT develops sinc-function-like lobes. When examined at other frequencies, the overall pattern persists for each increasing frequency. This pattern shifts in a regular manner towards the longer baseline lengths, increasing the width of each lobe in the sinc function and decreasing the slope value of the linear region. Both of these changes indicate that the source size grows smaller with increasing frequency, consistent with the images in Figure 3.5e.

Finally, to deduce the quantitative source size measurements from the actual RV, the linear portion of the RV distribution in Figure 3.5d is passed through a linear fitting procedure. The green dashed line shows the fit at 6.91 GHz after restricting the fit to the inner 40 baselines (out of total 78 baselines). These are the baselines that sample the linear portion of RV plots for the full frequency range. The FWHM source size is then determined from the slopes of these fits using Equation (2.3) to generate a source size spectrum as shown in Figure 3.5f in green symbols. Additionally, the one-dimensional circular size measured directly from the 50% contour of the peak intensity of the images is overplotted in black symbols. Both the measures agree reasonably well up to 10 GHz, after which the source sizes diverge mainly could be due to our assumption that the source is circular, whereas the EOVSA emission as seen in Figure 3.5e becomes more elliptical and elongated.

This exercise demonstrates that the RV source spectrum is a reliable tool to deduce the source size as a function of frequency even in the absence of imaging spectroscopy, so long as the source approximates a Gaussian shape. Furthermore, the departures from a Gaussian profile are easily recognized from the RV data. Having validated the RV approach, we now apply the RV analysis to the events in Table 3.1

and examine them for the source morphology differences between flat events and the non-flat normal events.

RV Analysis of Flares in our Sample Set

As discussed earlier, the auto-correlation measurements are not available for the set of bursts in our study, which were taken with a prototype correlator that was not producing correct auto-correlations. Therefore, we must form a pseudo-RV by substituting the data from one of the short inner baselines in the place of the auto-correlation data. Generally, the pseudo-RV is determined by $\frac{x_{ij}}{x_{\mathrm{short}}}$, where x_{short} is the cross-correlated amplitude of any sufficiently short baseline. This short baseline has a frequency-dependent fringe spacing (>18–2.5 arcmin for 2.5–18 GHz) large enough to guarantee that any reasonable flare source is unresolved. We note that, unfortunately, one of the strengths of RV–that it is independent of calibration–is lost for this pseudo-RV form on those events, so we must limit our study to the events with good gain calibration. Due to that, events 1-6 in Table 3.1 are not ideal for this pseudo-RV analysis and therefore limiting to events 7-13.

To illustrate the steps in the pseudo-RV analysis, we use the decay phase of the M1.0 class flare observed on 2015 August 24 (a flat spectral event, number 8 in Table 3.1, with an averaged index of $\sim$1.8 at the peak and ~ 0.8 in the decay phase). Figure 3.6a and c show the time profiles at 7.88 and 13.95 GHz, and the total power dynamic spectrum of the burst, respectively. The time profiles indicate that the event is a very impulsive burst lasting for about a minute. The vertical dashed line marks the time 17:45:26 UT, at which the pseudo-RV is determined, selected in the decay phase with flux density $> 25\%$ of the peak value. Figure 3.6b is the flux density spectrum at this time, with the low frequency slope $\alpha_l = 1.2$.

The number of good baselines available for this event was 9, far fewer than the 2017 September 10 event with 78 baselines. Figure 3.6d is the $\ln(RV)$ vs. square of the

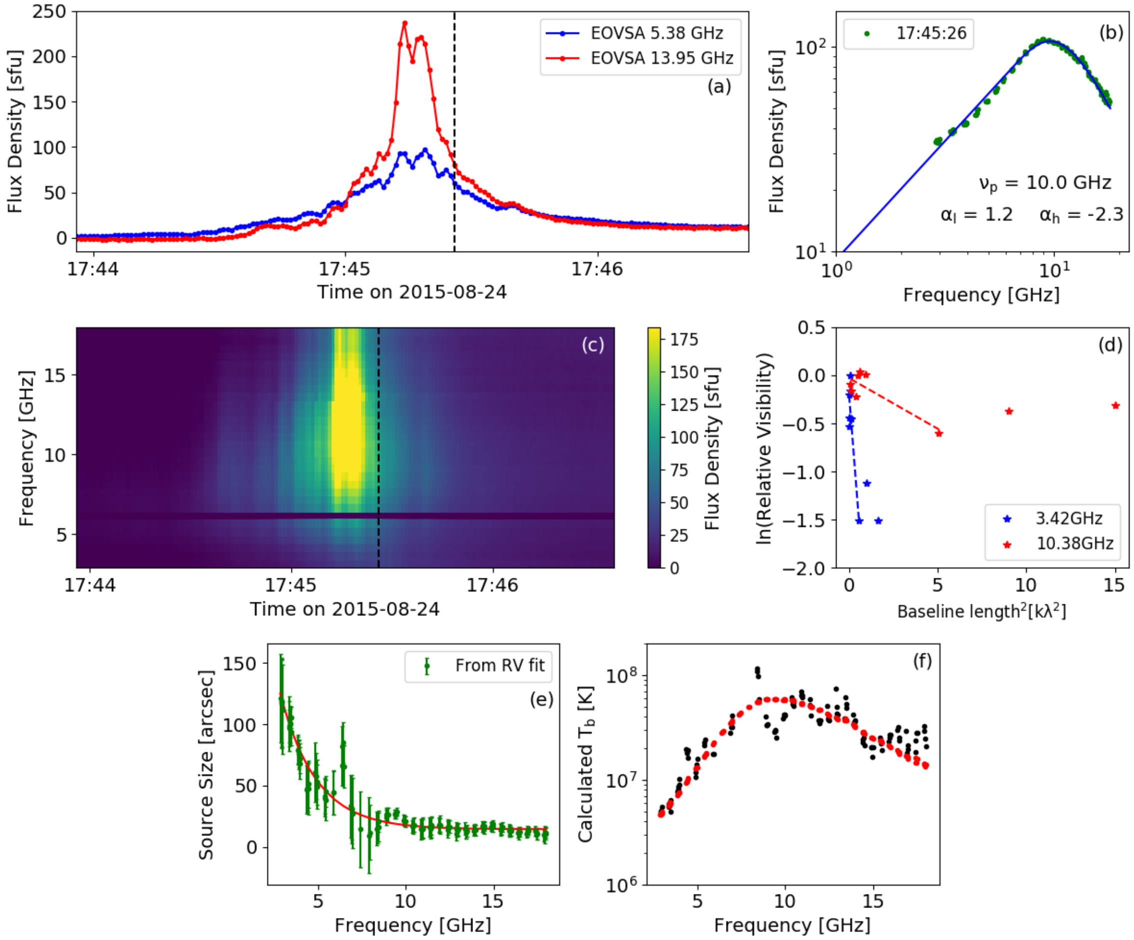

Figure 3.6 Relative visibility and source size analysis during the decay phase of the August 24, 2015 flare. (a) to (c): Time profiles, flux density spectrum at the decay phase, and the total power median dynamic spectrum of the burst. Fitting parameters are marked at the bottom of the panel (b). (d) ln(RV) as a function of B_λ^2 at the two given frequencies. (e) Source size spectrum extracted from relative visibility slopes at each frequency. The red curve is the exponential form fitting of the source size. (f) Calculated brightness temperature spectrum from the obtained source size measurements. The black symbols are from the actual size measurements (green in panel (e)), and the red symbols are from the fitted curve (red in panel (e)).

baseline length plot at the two frequencies marked at the bottom of the panel. Here, the pseudo-RV is calculated using $\frac{x_{ij}}{x_{14}}$, where x_{14} is the cross-correlated data from antennas 1 and 4 acting as an auto-correlation component which has the maximum peak flux density compared to the other short baselines. For both the frequencies plotted in the figure, the 9 RV amplitude points are spread such that the first 6 are in a close cluster at short baselines, and the remaining 3 are spread outwards at the longer baselines.

When these $\ln(RV)$ vs. B_λ^2 plots are viewed progressively with frequency, the 9 RV points shift in a fashion similar to that of the previous event, with the points extending outward for increasing baseline length. Even though a clear sinc-like function curve cannot be distinguished due to the smaller number of baselines, the same combination of linear and non-linear trends is apparent. The fitting is carried out with the first 7 points, which lie on the linear trend, ignoring the flatter trend of points 8 and 9, which may represent the sinc-like function in Figure 3.5. Fits to these 7 points for the given two frequencies are shown by the dashed lines in Figure 3.6d. Fits at other frequencies follow this same trend, giving us confidence that these fits reveal the general source size trend with frequency despite the relatively large scatter of the points. By determining the slopes of the line fits at each frequency, the source size spectrum is obtained as shown in Figure 3.6e, where the large error bars reflect the uncertainties in the individual fits. The source size starts with a value of ~ 125 arcsec at the lowest frequency 2.9 GHz and continues to decrease to $\sim$ 10 GHz. After $\sim$ 10 GHz, the size remains small and almost constant for higher frequencies, as expected for an optically thin source. The overall pattern of source size with frequency is well fitted with an exponential function (red curve in Figure 3.6e).

The source size estimates from the RV analysis can be used to calculate the brightness temperature spectrum for the measured flux density as shown in Figure 3.6f. The peak brightness temperature reaches at least 6×10^7 K and decreases

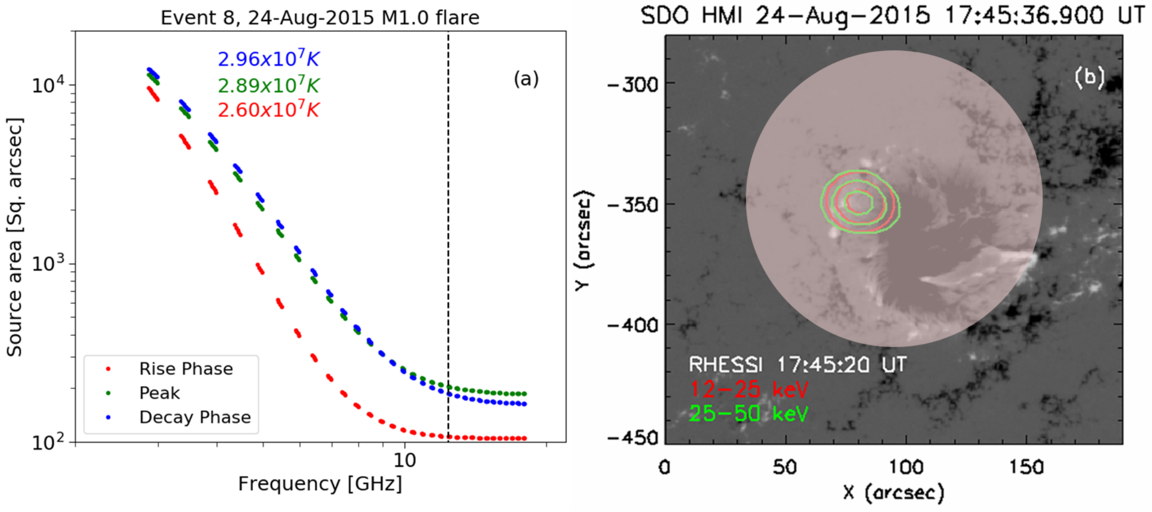

Figure 3.7 Source area spectrum from RV measurements at the three phases of the 2015 August 24 burst with the corresponding hard X-ray emission. (a) The areas are obtained from the RV applied at each of the three phases (red, green, and blue). The brightness temperatures marked at each phase are the average values calculated from the RV measurements. The peak frequency, 12.4 GHz at the peak time, is marked by the vertical dashed line. (b) RHESSI flare emission contours are plotted at 50, 70, 90% of peak flux in red and green over the HMI magnetogram. The decay phase LF source at 2.9 GHz is shown as a cartoon with a circular masked region.

towards both lower and higher frequencies. The black points in Figure 3.6f are calculated from the individual points in Figure 3.6e, while the red points are calculated from the exponential fit.

Figure 3.6 gives the RV source measurements for one time during the decay phase of the burst. We repeat the analysis for the other phases of the burst (rise and peak) and convert the exponentially fit source size to arrive at the source area spectra assuming a circular source shown in Figure 3.7a (red, green, and blue points, respectively). The measurements suggest that the source was already quite large during the rise phase and grew substantially larger at the peak. Then the source stopped evolving in size and faded in brightness during the decay phase.

It is of interest to compare the source area spectrum in Figure 3.7a with the similar one in Figure 3.4a for the 2015 March 10 event. Recall that the source area spectrum in Figure 3.4a was derived from an assumption of a single constant brightness temperature over the whole frequency range. This assumption served to show that the source area must be large, but it cannot be realistic and leads to a sudden flattening of the curves at lower frequencies in Figure 3.4a instead of the continued rise in the source area, we see in Figure 3.7a. With the benefit of RV analysis, we could derive a brightness temperature spectrum that varies with frequency in agreement with expectations from theory [17] as in Figure 3.6f. For this decreasing T_b at the low frequencies, the source area continues to rise steeply and shows a much larger source area needed to match the observed flux density.

For spatial comparison, the one-dimensional size of $\sim 125\,\mathrm{arcsec}$ at 2.9 GHz from the RV measurements for the decay phase is overlaid as a cartoon on an HMI magnetogram in Figure 3.7b, with RHESSI contours at $12-25$ and $25-50$ keV. Clearly, the low-frequency emission of the flare requires a far larger source extent than the RHESSI contours ($\sim 30\,\mathrm{arcsec}$). Most of the usually reported RHESSI flare sources, as seen in Figure 3.4b, are restricted to only the higher density regions that occur at low coronal heights in the flare [58, 10, 59]. The extended emission that we observe here suggests the involvement of the overlying magnetic structures, which have correspondingly lower magnetic field strength and density, leading to such low-frequency emission. The conclusion that LF sources sometimes exhibit a large emission area at a relatively high brightness temperature $> 10^7$ K agrees well with the previous recent studies [25, 22].

This pseudo-RV analysis is further conducted on the remaining events listed in Table 3.1 (events 7 and 9 to 12) to estimate their source morphology. The results are shown in Table 3.2 along with the spectral index at the time of RV measurements. These source sizes shown here are those measured for the lowest frequency observed in each of the events. The flat spectral events, in particular, have shown a source size of $\geq 120\,\mathrm{arcsec}$, and thus, there is generally an anti-correlation between low-frequency source size and spectral index.

Table 3.2 Source size Measurements from RV Averaged over 3 seconds at the Lowest Frequency

Event Number	Spectral index α_l	Source size (arcsec)
1^*	1.5	-
2^*	0.8	-
3	3.7	-
4	3.7	-
5^*	0.7	-
6^{**}	1.3	-
7	6.6	70
8^*	1.2	125
9	2.1	97
10	3.0	71
11	1.8	95
12^*	1.1	120

Note: The corresponding averaged spectral index of each event at the time of RV calculation is given in the second column.

3.4.3 Adding Inhomogeneity

We have demonstrated that emission from a large source area at low frequencies is needed to make the flux density spectrum flat. We have suggested that this is due to a rather extreme source inhomogeneity. As a flat microwave spectrum diverges from the spectrum produced by a single uniform source, the general homogeneous source theoretical model cannot produce an acceptable fit. Hence, modeling that includes inhomogeneity of the source is needed to explain the observed flat spectrum [55]. An intermediate step in complexity is to consider an inhomogeneous model consisting of multiple homogeneous sources that are physically discrete, but when combined, will result in the observed flat spectrum. As discussed in Chapter 2 we demonstrate the idea of inhomogeneity by adopting a model introduced by [49], which represents the three-dimensional (3D) magnetic field distribution with multiple sources of homogeneous components [see Equations (2.4) and (2.5)].

As a specific example, in Figure 3.8 we show the EOVSA total power spectrum of the 2015 August 24 event for the decay phase at 17:45:26 UT (marked with plus symbols). The dashed lines are the model spectra produced from each of the seven spectral components, and the black line shows the total contribution from all the emission of each component. These discrete components can be visualized as the emission from the source regions where the electrons have access, traveling from the main acceleration site during the flare. Individual peaks from these discrete sources are not expected to be observed in the total power flux density as the spectra are measured integrating over the area from the entire flaring region.

Along with the seven values of magnetic field B_i (spaced between 1900 and 380 G), the parameters given in Table 3.3 (except α and β) are varied according to their dependence on the spectral shape [32, 107, 35]. The high frequency index α_h at the time of the spectrum gives electron power-law index $\delta \approx 4.1$. Since α in Equation (2.4) is the factor that controls the slope of the spectrum in the optically

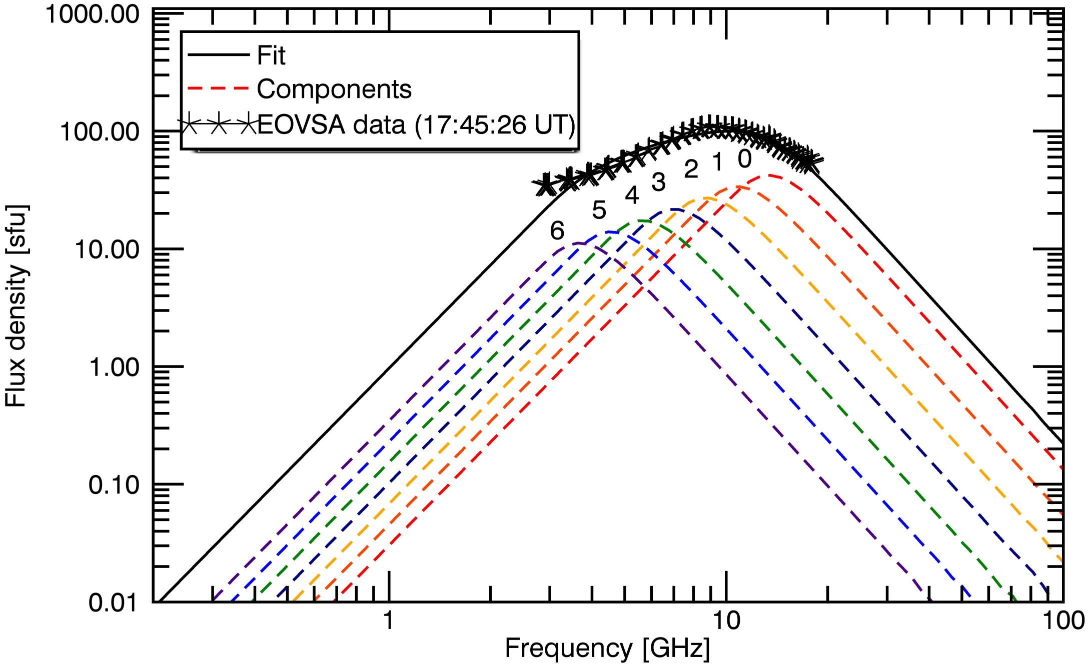

Figure 3.8 Inhomogeneous model applied to the observed flux density spectrum of the 2015 August 24, M1.0 flare at the time marked. The dashed curves of various colors are the simultaneous emission spectra derived from the seven components labeled 0 to 6. The plus symbols mark the observed spectrum, and the thick black line shows the overall fit.

thick part, it is set separately from the other parameters. The remaining parameters, B_0 and L_0 are fixed with nominal values to obtain the peak frequency close to the observed one. Then, A_0 is set to match the total flux density, and N_{NT} value is set arbitrarily, which is the spatial density of the non-thermal electrons. Having these multi-variant parameters, the model spectra that best matches the observed spectrum are distinguished having the least χ^2 value generated from

$$\chi^2 = \sum_{i=0}^{nf-1} \frac{[S(\nu_i) - S_m(\nu_i)]^2}{\sigma_i^2},$$

where $S(\nu_i)$ and $S_m(\nu_i)$ are the observed and model fit flux densities with σ_i being the uncertainty at each frequency ν_i.

Table 3.3 Model Parameters

α	β	δ	θ°	Density N_{NT} (cm^{-3})	Thickness L_6 (arcsec)	Area A_6 (arcsec^2)
0.6	0.2	4.1	50	3.8×10^6	69	284

The area A_6 and the thickness L_6 in the table are for the lowest-frequency component 6, peaking at ∼ 3.2 GHz. The area and thickness of the components (0 to 6) range from 108 to 284 arcsec^2 and 50 to 69 arcsec, respectively. To resolve the smallest (11 arcsec) of these discrete sources requires a radio array with modest baseline lengths of order 1 km depending on frequency (0.38 km at 18 GHz). However, EOVSA imaging spectroscopy already provides a much higher resolution of 3.3arcsec at 18 GHz.

As the fluxes in this model are summed to match the flux density spectrum, when each component is combined, give an overall area of ∼1290 arcsec^2 (equivalent circular size of ∼40 arcsec). This size is although smaller than the size estimates given earlier but nevertheless serves to show that an inhomogeneous source can account for the shape of the spectrum. In addition, the corresponding emission volumes accounting for the LOS thickness, $V_j = A_j L_j$, for any component j, are quite large and grow larger at low frequencies.

These measurements indicate that for reproducing a flat spectrum, the emission either has to be comprised of multiple emission components simultaneously observed within the flare volume or has to be from a huge volume. The model shows that the flat spectrum can be the consequence of a significantly large source structure that is implausible to be homogeneous for such extended physical space over the active region and can only be inhomogeneous in nature.

3.5 Summary

We study the flare radio source morphology in the low-frequency emission using the flux density spectra of 12 bursts during 2015 with the excellent frequency and time resolution data available from the EOVSA interferometer. Having the optically thick spectral index as a proxy for microwave source morphology, we illustrate the LF sources associated with the flat spectra by the following characteristics.

1. A flat spectrum can be explained as the emission from spatially inhomogeneous, non-uniform physical parameters of a large source area and/or with simultaneous multiple emission components within. First, the relative visibility source area measurements have shown that the events with flat spectra have a source size greater than at least ~ 120 arcsec at low frequencies. Second, the observed flat spectrum can only be reproduced by the inhomogeneous model with discrete parameters on the source function. Finally, the area spectrum analysis indicates that the source size observed at a relatively low brightness temperature is still large in the case of a flat spectrum than the typically observed LF sources (that roughly follow $A \propto \nu_{\mathrm{GHz}}^{-2}$ [4]). Therefore, the microwave sources at low-frequency can be large, extended, and complex in the spatial domain, whose existence suggests that the accelerated particles have access to a large region of space during the flare.
2. As an evolutionary trend, we observed that most spectra (for nine out of 12 events) exhibit a decrease in α_l significantly in the decay phase from the index value at the peak time. This trend indicates that the inhomogeneity and the complexity of the emission volume increase as the flare process advances. As a piece of evidence for this from flare imaging, the event discussed in [30] shows

the flare sources observed at low frequencies during the decay phase multiply to a bigger size and discrete spatial characteristics.

3. Five of the flat events, in particular, have shown a more shallow and flatter spectrum. Their spectral index is much less than 1.0 in at least any of the three phases of the bursts. In turn, we conclude that the occurrence of large and complex microwave sources, i.e., indicated by the flat spectrum, can be seen in 42% of the flares (5 out of 12 events). All of these flat spectral events are originated mainly from the active regions with a complex magnetic configuration of $\beta\gamma\delta$ (as in Table 3.1). We also find that a flat spectral event need not necessarily be a high-intensity flare with a huge flux density.

In summary, focusing mainly on the low-frequency emission and flat spectral cases, this study has given the means to understand the characteristics of the seldom examined LF microwave flare sources relative to the usually observed high frequency optically thin sources. The large volumes of these sources can involve the large-scale coronal loops filled with particles that get injected and escaped as the seeding particles for solar energetic particle (SEP) events.

A better understanding of these large LF sources and their role during a flare, their magnetic field structure, and their spatial relationship to more commonly observed components of solar flares can be achievable with adequate imaging data now becoming available. This work highlights the importance of focusing on the LF optically thick microwave emission in future studies.

Chapter 4

LARGE MICROWAVE FLARE SOURCES OBSERVED BY EOVSA IMAGING SPECTROSCOPY

4.1 Introduction

Even though solar flares have been observed at microwave frequencies for a few decades, there have been only a handful of observations made at low frequencies, as discussed in Chapter 3. Out of these rare observations, a few have shown gyrosynchrotron emission originating from large and complex source morphology. The role of these LF sources in the flare process and their characteristics are not very well understood in detail due to the paucity of relevant observations.

Chapter 3 discussed in detail the flat spectral slopes as an indicator of the large and complex area of the LF sources. That study also introduced the possibility of multiple emission components to explain the inhomogeneity in the source emission. However, spectral information alone is not enough to interpret the level of inhomogeneity and spatial complexity. This raises the need for high-resolution imaging spectroscopy, which is now provided by EOVSA since its upgrade in the year 2017.

Some of the high-frequency studies have shown that the flare emission is observed along with remote sources, which are believed to result from reconnection of the low-lying loops with the overlying and adjacent loops [38, 117, 16, 120]. Previous studies with microwave imaging have also discussed the importance of complex configuration of magnetic structures with double-loop and multiple loop interactions [82, 44, 45, 63, 40] to produce microwave flare emission. But, not many of the previous studies have examined the low-frequency counterpart of the microwave emission for these complex loop interactions and remote site microwave brightenings.

Based on the conclusions from the study discussed in Chapter 3, in this chapter we focus on examining the spatial source morphology and the magnetic field configuration of the LF sources in another event that has EOVSA imaging. The contribution of multiple loops is investigated in reference to microwave emission occurring in the flaring region. We study the related LF emission through the high-resolution images observed from the EOVSA.

EOVSA started imaging observations in early 2017. The flare event SOL2017-04-04 discussed in this chapter had imaging at 15 frequency channels spanning the 3.44 to 18 GHz frequency band. In the earlier sections of this chapter, the primary examination of all the time profiles, flux density spectra, and imaging of the flare are conducted. In Section 4.4, the changes in the source morphology with the observing frequency are discussed, followed by Section 4.5, which explains the possible magnetic configuration of the flaring region to produce the observed LF sources.

4.2 EOVSA Microwave Spectroscopy and Imaging

SOL2017-04-04 is a C4.9 class flare from the NOAA active region 12645 (S10W47). EOVSA had full coverage of this flare with NoRH at 17 GHz, RHESSI, and AIA EUV observations.

In this current study, during the early commissioning phase, the images were produced by combining frequency channels in each odd spectral window giving 15 equally spaced frequencies ranging from 3.44 to 18 GHz band. With the width of each spws of 160 MHz, the center frequencies of these spws fall at $f_{GHz} = 2.94 + n/2$, where n is the odd spectral window (spw) number from 1 to 30.

Figure 4.1 shows the multi-wavelength time profiles of the flare observed by GOES, RHESSI, and EOVSA. The time derivative of the 1 to 8 Å soft X-ray emission from GOES (Figure 4.1a) resembles the light curves of RHESSI 25 - 50 keV band hard X-rays (Figure 4.1b) and EOVSA microwave emission (Figure 4.1c and

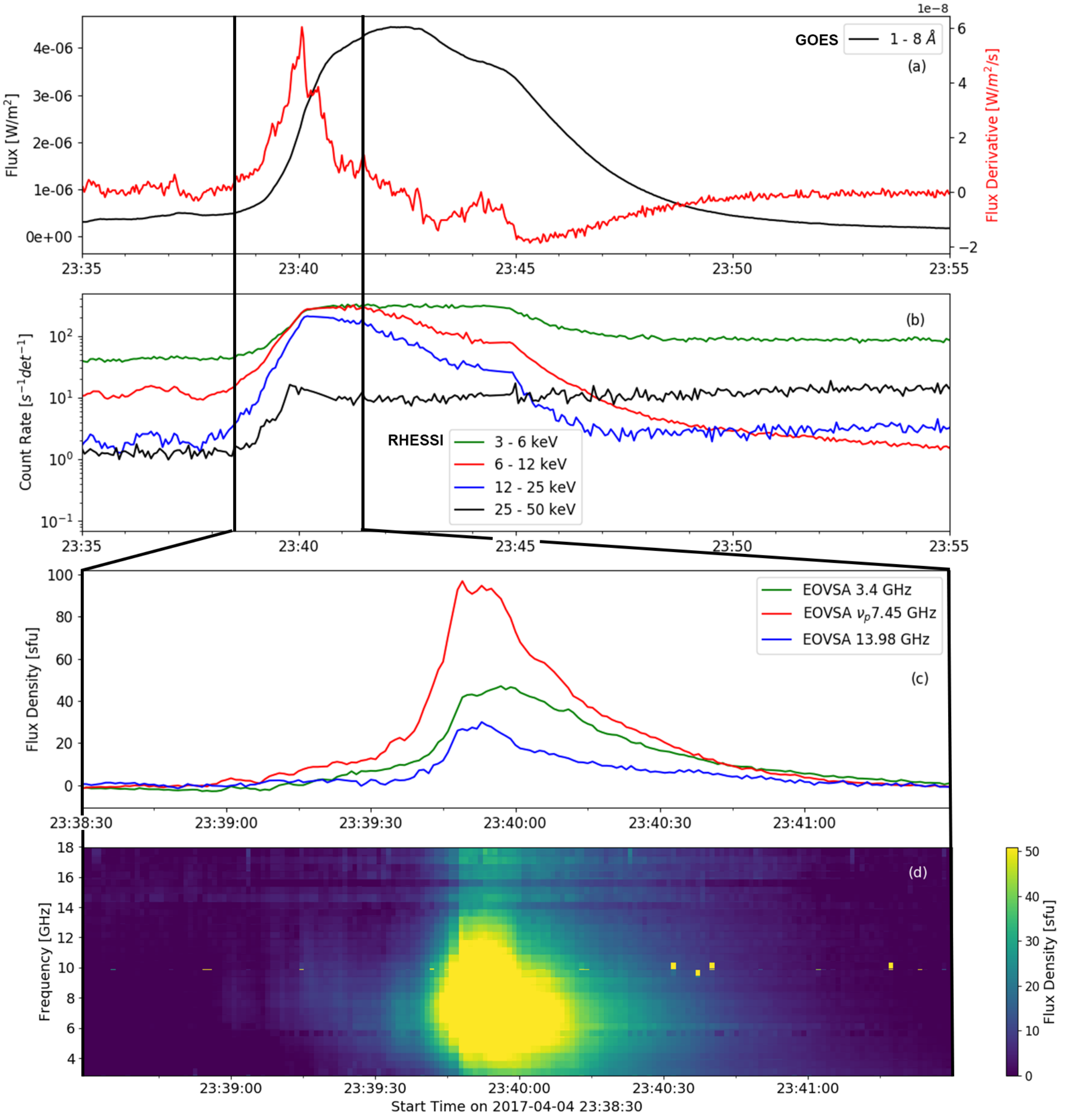

Figure 4.1 Multi-wavelength time profiles of the flare from EOVSA, RHESSI and GOES observations.

4.1d) peaking between 23:39:45 and 23:40:00 UT (in agreement with the so-called "Neupert effect" [84]). The time duration marked by the vertical lines in GOES and RHESSI lightcurves encloses the time of the EOVSA light curves at the three marked frequencies and the total power median dynamic spectrum of the EOVSA emission between 23:38:30 to 23:41:30 UT. This event is a short-lived microwave burst lasting for less than five minutes in EOVSA emission.

4.3 Multi-wavelength Observations

Figure 4.2 shows the EOVSA contours for eight different frequencies overlaid on SDO AIA 171 Å EUV images for the peak time of the burst (∼23:39:54 UT). Lower contour levels of 5, 10, and 20% are included in the low-frequency EOVSA maps to reveal the full extent of the emission. The flare brightening from EUV, hard X-rays, and microwaves is mainly concentrated at the eastern sunspot with a small loop system, which we call the main flaring site (source $S1$). RHESSI hard X-ray, high-frequency EOVSA, and NoRH 17 GHz (optically thin) sources show the confined emission associated with the small loop at the main site. RHESSI contours show complex features with two to three individual centroids over the small region of the main site. These sources may be individual footpoints and possibly looptop emission from the small loop. With decreasing frequency, the EOVSA emission increasingly extends from the main flaring loops farther westward towards the western sunspot at coordinates (800,-100). An extension to the east is also seen. The extended emission shows distinct emission centroids predominantly at 3.44 and 4.44 GHz that diminish to a single main source by 10 GHz. These LF optically thick sources visible at multiple locations suggests that the accelerated particles have access to a large volume in the active region, which is investigated in the following sections.

To examine the observed LF source morphology at 3.44 GHz in connection with the flux density spectrum and its shape, Figure 4.3 shows the time evolution of the

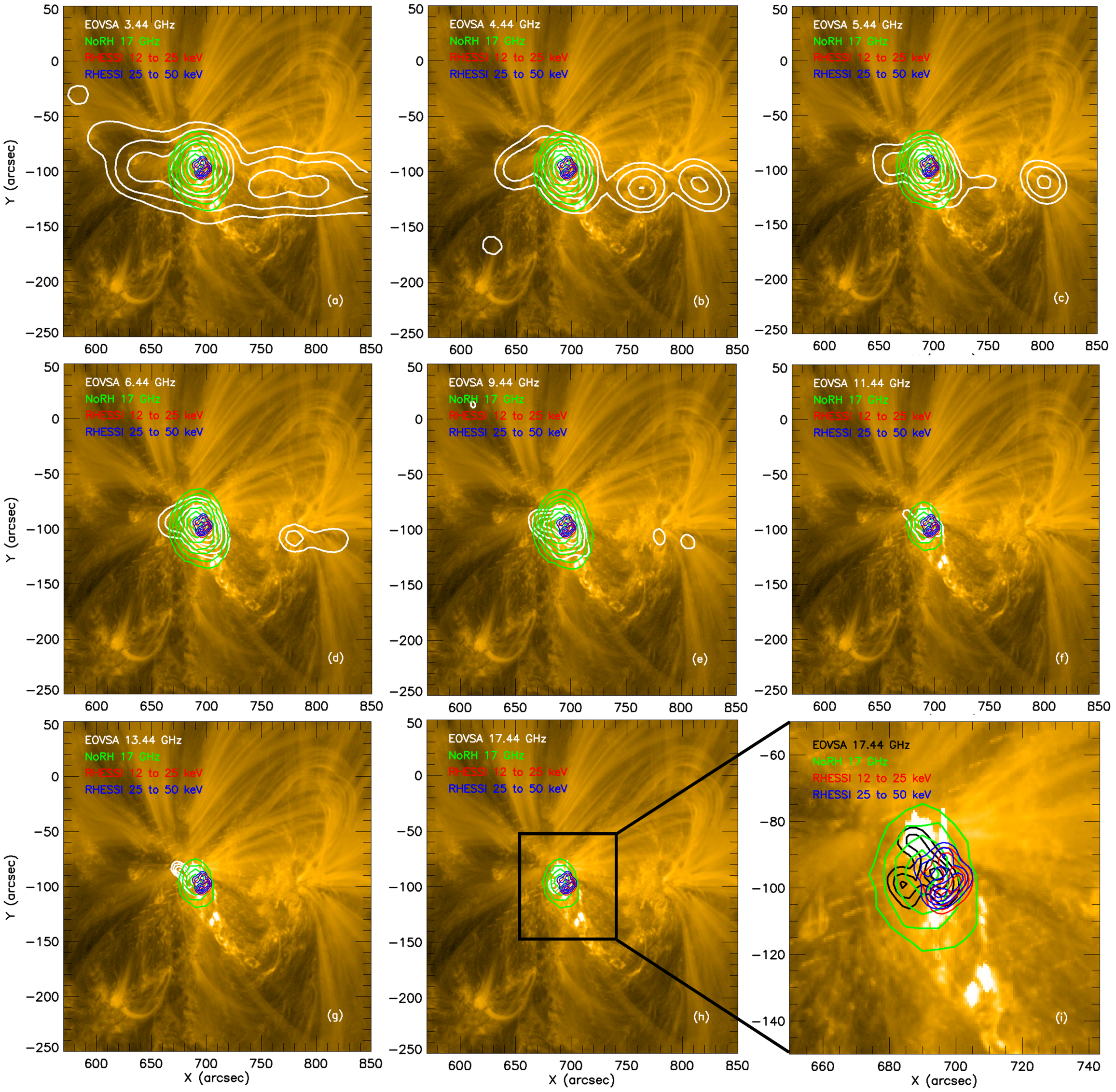

Figure 4.2 Spectral evolution of the flare sources as observed by EOVSA, RHESSI (12 - 25 and 25 - 50 keV), and NoRH 17 GHz overlaid on SDO AIA 171 Å for ∼23:39:54 UT. From 3.44 to 9.44 GHz, maps of EOVSA and NoRH show contour levels of 5, 10, 20, 30, 50, 70, 90% and RHESSI with 30, 50, 70, 90% of the peak emissions. From 11.44 to 17.44 GHz, all the maps show 30, 50, 70, 90% contour levels. Note that the color of the RHESSI contour in the last panel (i) is changed to black from white only for the color contrast from the background EUV emission.

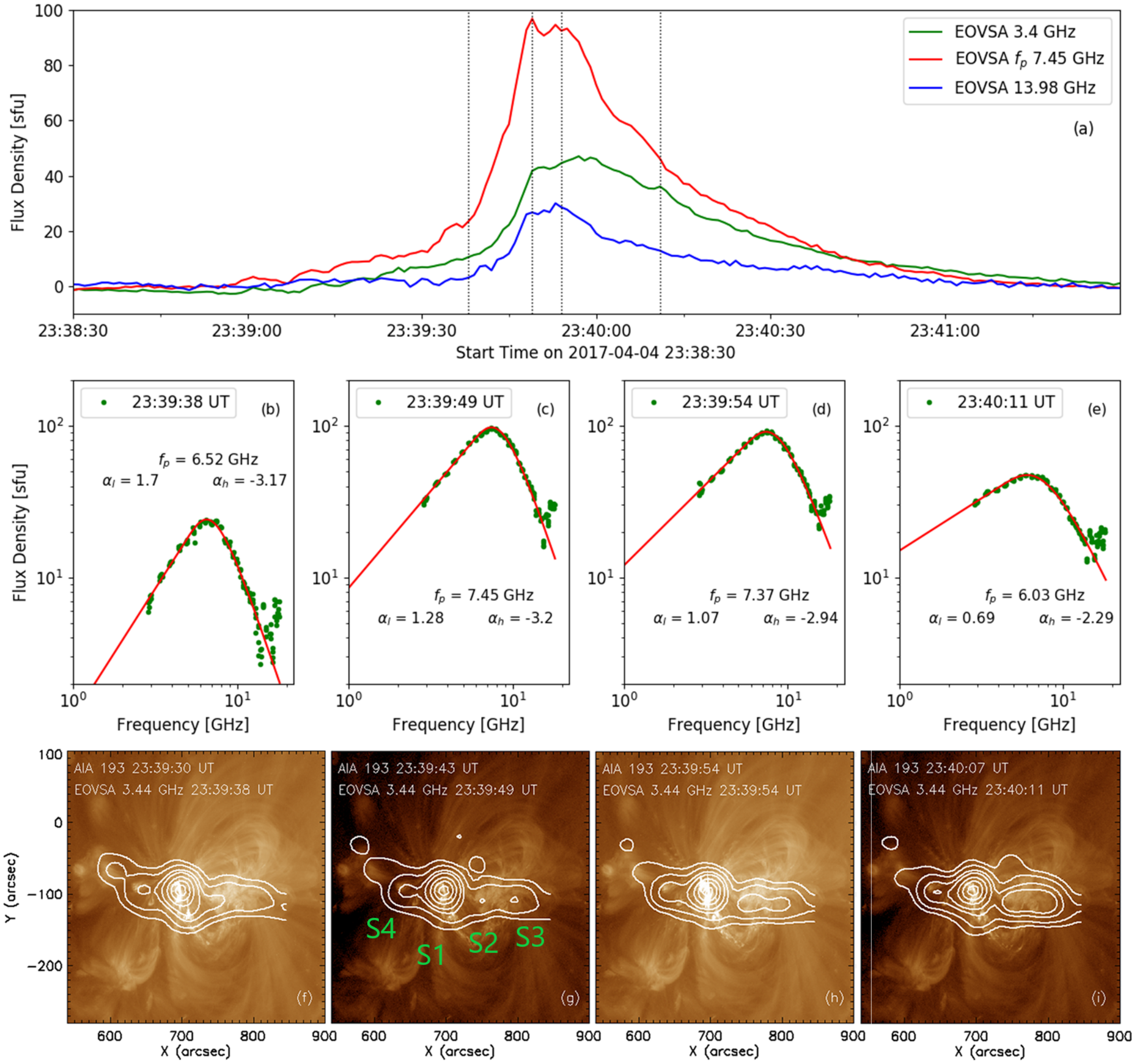

Figure 4.3 Light curve and the flux density spectrum at a different time of the event. (a) The light curve at the three frequencies is marked on the top. The black vertical lines are the times at which the spectra and images are shown in the following panels. (b to e) Flux density spectra at the four selected times and fitted with the procedure introduced in [107]. The spectra show the characteristic shape with peak frequency ranging between 6 to 8 GHz. Note the spectral parameters are marked for each spectrum. (f to i) EOVSA 3.44 GHz emission contours overlaid on AIA 193 Å image maps close to the four times.

images and spectra simultaneously. The middle row of panels show the behavior of the flux density spectrum with time. The solid curve is a fit to the spectrum following the same spectral fitting procedure explained in Section 3.2. The fitting frequency range excludes frequencies from 13 GHz in order to exclude the outliers. The four times (vertical lines) on the light curve of Figure 4.3a are selected depending on the features observed in the images. The two times in the middle are the peak times for two widely spaced frequencies. Until the first time in the rise phase, the source remains compact As the burst continues to brighten after the initial rise phase, the main site develops in size and complexity. Around the peak time, the distinct LF emission is seen at three additional locations together with the main site $S1$. We call these sources $S2, S3$ and $S4$ as marked in the figure. The fourth time is well into the decay phase, at which the LF sources show the maximum extent of size and complexity.

As the flare progresses from peak to decay phase, the LF source reaches an overall source size of $\sim 250\,\mathrm{arcsec} \times \sim 100\,\mathrm{arcsec}$ at 10% contour level for 3.44 GHz. The corresponding flux density spectra in Figure 4.3b to 4.3e show an increased flatness (decreased α_l) with time in the optically thick portion of the spectra. This is in good agreement with the study of Chapter 3 [99], which shows that the extreme flatness is a direct indication of the increase in the source size and/or the complexity of the source at low frequencies.

This dramatic increase in source complexity in the decay phase suggests that after the onset of the burst, the accelerated particles continue to get injected and trapped in the magnetic system to emit at these frequencies. This might be due to the successive reconnection that continues to take place in the flaring region. In addition, simultaneous occurrence of the distinct sources $S1, S2, S3$ and $S4$ at various sites creates a large inhomogeneous source (Figure 4.3f to i).

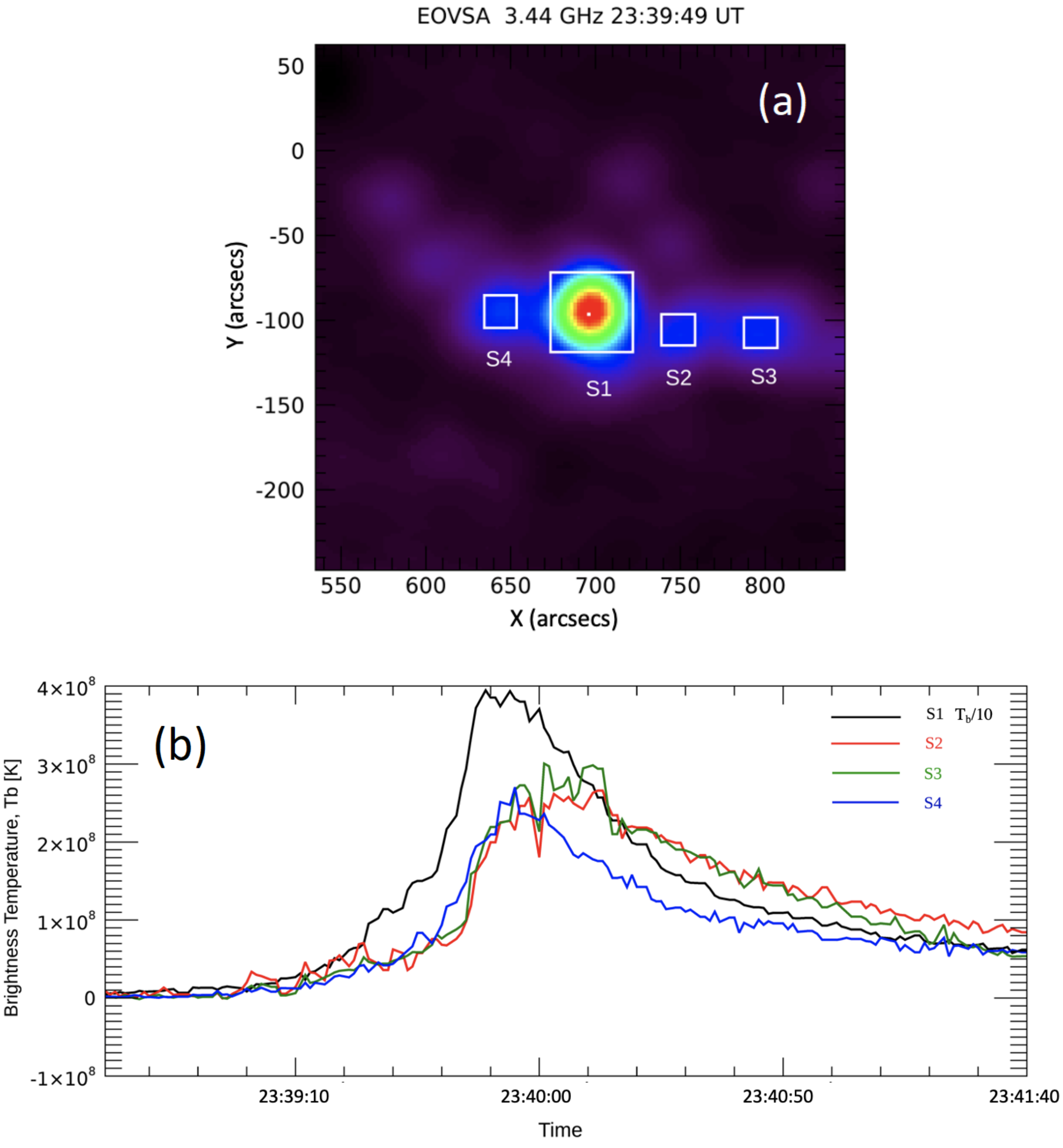

Figure 4.4 Time profiles of the integrated brightness temperature of the main source and secondary sources observed at 3.3 GHz. (a) Selected regions over each source is marked with the boxes. (b) The corresponding integrated brightness temperature profiles for each source. Note that the main source $S1$'s profile is scaled by 10 only for the purpose of mutual comparison.

A time lag is expected between time profiles of emissions from the main site and secondary site compared with the Hard X-ray time profiles as suggested by [45], but such travel time delays are expected to be less than 1 s, which is too short for EOVSA to resolve. However, a comparison of the temporal evolution of the individual sources is still of interest since it can shed light on other particle transport effects such as injection and trapping that can occur over longer timescales. A visual comparison of the appearance of EOVSA sources with AIA EUV 171 Å movie and GOES soft X-rays time profile shows that the secondary sites illuminate after a delay from the start of the main site radiation at 3.3 GHz. Figure 4.4 shows the time profile comparison among the sources $S1, S2, S3$ and $S4$ observed at the lowest frequency (3.3 GHz). The brightness temperature of the sources is integrated over each of the boxes shown in Figure 4.4a. Figure 4.4b shows the light curves. To facilitate comparison, the extremely bright main source (black) is shown divided by a factor of 10. Clearly, the two easternmost sources (main source $S1$ and eastern source $S4$) show very similar temporal evolution while secondary sources $S2$ and $S3$ show a finite time delay of 10-15 s and have a more extended decay compared to the main source. The sources $S2$ and $S3$ change with a similar fashion with time, but source $S4$ has a little smoother behavior. We will discuss possible reasons for these differences Section 4.5.

4.4 Source Morphology as a Function of Frequency

Some previous studies have shown the source size dependence on frequency ν as $d_{FWHM} \propto \nu^{-1}$, that is area $A_{FWHM} \propto \nu^{-2}$ [5] and more generally $A_{FWHM} \propto \nu^{-\gamma}$ with γ between 0.5 and 3.5 [22]. Here, in the case of this event, we can directly measure the "area spectrum" as we do in Figure 4.5. The figure shows two measures of the source area, one taken within the 50% contour in the right panel, which reflects only the area variation of the main source, and one taken within the 10% contours to include the rapid increase in source area at low frequencies. Two points have

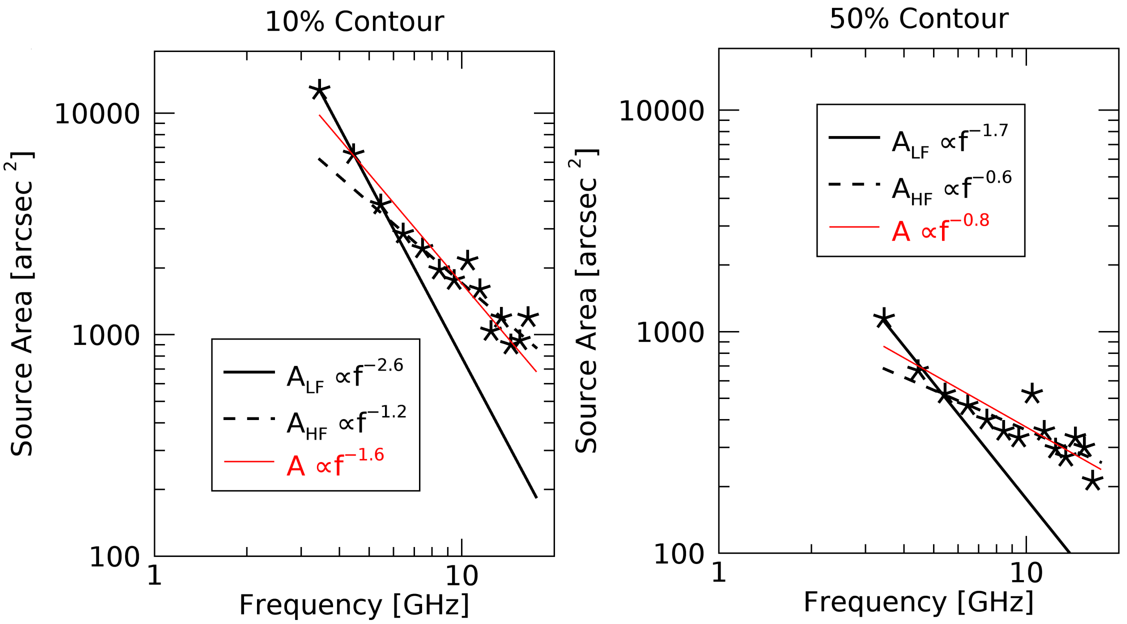

Figure 4.5 Power-law dependence of the source area spectrum at the peak time of burst for the 10% and 50% (FWHM) contours of peak emission.

to be noted when considering general relationships for the source area. Firstly, a single power-law is not applicable for the entire gyrosynchrotron frequency range with both the optically thick and thin emissions. There is a clear change in the trend of source area between the low-frequency and high-frequency emissions. The other point is that the full-width half maximum size of a single dominant Gaussian source cannot represent the overall emission observed in the LF sources, which are far from Gaussian in shape. Therefore, FWHM area measurements for the LF sources over the entire frequency range are not useful for this flare. Figure 4.5 shows the frequency dependence of the LF sources and the associated power-law indices. The secondary sources become visible only well below the ≤45% contour. They become largest and full-fledged at the low-frequencies only when emission is included down to the 10% contour level. The two black (solid and dashed) lines show individual trends of the low-frequency and high-frequency sources, where the low-frequency trend of the 10% contour shows an even steeper index than the one discussed in [5]. The 50% source area trend clearly shows that it does not include the emission from the secondary sources but only that from the main site, so that the area more closely follows a single powerlaw for all frequencies except the lowest one. In both cases, the area of the LF sources (with index 2.6 and 1.7) falls much more steeply than the high-frequency sources (with index 1.2 and 0.6). If a single powerlaw fit is attempted (red lines), the index falls to -1.6 but this underestimates the rapid increase in size at the lowest frequencies. Applying these insights to the work in Chapter 3, we can speculate that the flat-spectrum events studied there may have similar behavior, but more flat-spectrum EOVSA events should be studied in the future to verify this.

4.5 Magnetic Reconnection Site and Low-Frequency Sources

In Figure 4.6a the tri-wavelength AIA EUV image at the burst peak time shows that the flaring region involves a multiple flux loop system. All the loops with loop legs that closely match with the EOVSA sources $S1, S2, S3$ and $S4$ and that are involved in the flaring process (Figure 4.6b) are numbered from 1 to 6. Figure 4.6b shows the microwave emission at three different frequencies overlaid on the HMI magnetogram. This overlay shows the relative locations of microwave sources over the magnetic structure of the flaring region. This comparison between Figure 4.6a and b have shown that four possible flux loops 1, 2, 3, and 4 can be mainly involved for the microwave emission of the flare.

We obtain non-linear force-free field (NLFFF) extrapolation using the GX-simulator modeling tool to understand the magnetic connectivity of these distinct sources at low frequencies. Figure 4.6c shows the extrapolated field lines within the black box of Figure 4.6b zoomed over the main site. The active region shows a quadripolar structure that connects the majority of the large loop system. The negative polarity spot (at the north-eastern side) is mainly structured in an inverted ”U” shape, engulfing tiny and distributed positive spots creating a compact loop system. This small compact loop system portrays a closed dome-shaped structure

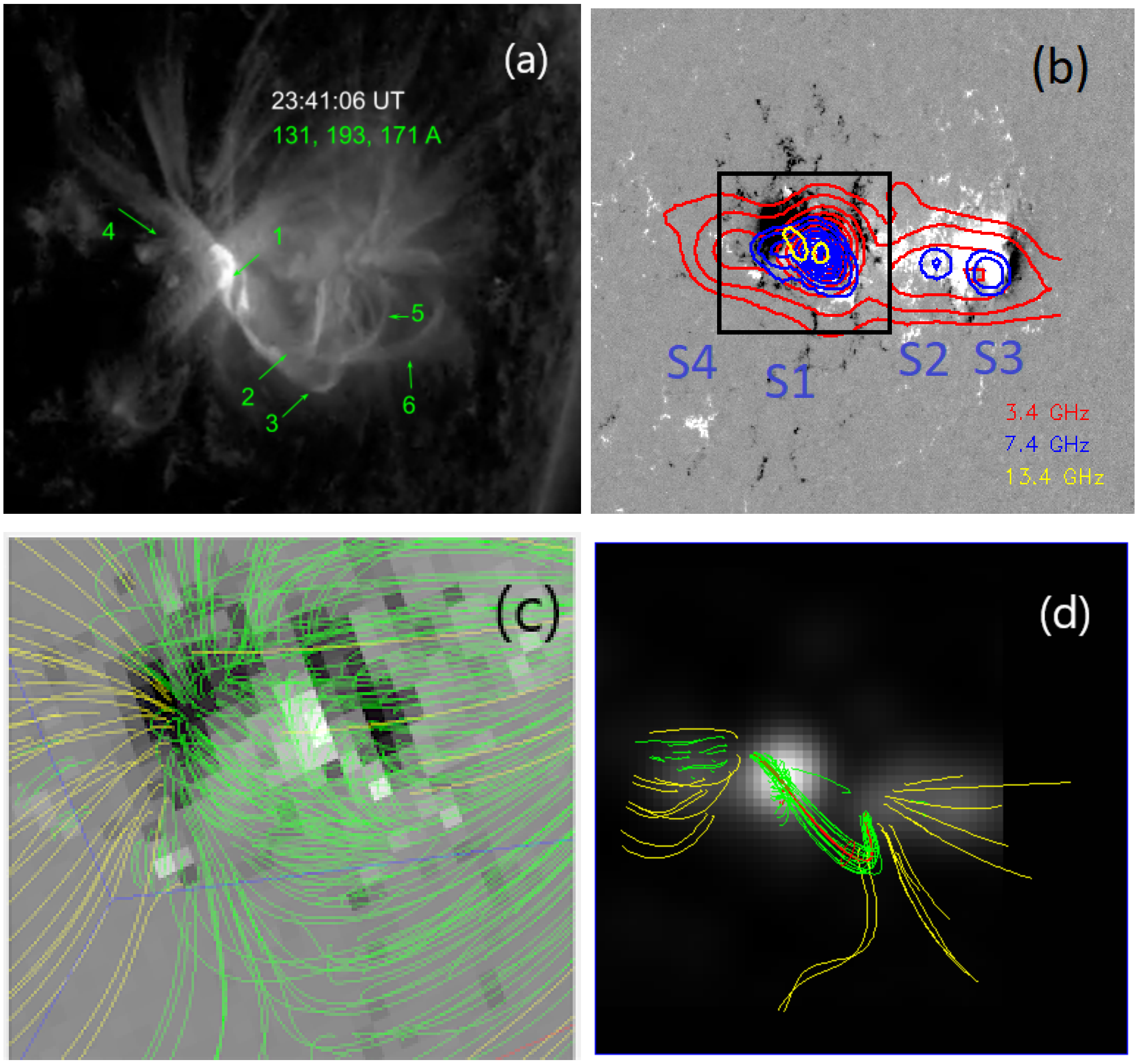

Figure 4.6 (a) Picture of the main magnetic loops in the flaring region as observed in triple-wavelength AIA EUV image during the peak of the burst. The numbers show the corresponding loops that match with EOVSA LF source centroids. (b) EOVSA LF emission at the marked frequencies overlaid over the HMI magnetogram. (c) Zoomed view of the active region configuration with extrapolated flux lines over HMI magnetogram obtained from GX-simulator modeling tool. The closed flux lines are in green, and the open field lines are in yellow. (d) The corresponding extrapolated flux tubes are overlaid on the EOVSA 3.3 GHz emission.

that extends on one side towards the western positive polarity spot. These compact loops are the locations of the main flare brightening, as discussed earlier (Figure 4.2). The magnetic flux tubes corresponding to this magnetic connectivity of the flaring region are shown in Figure 4.6d overlaid on EOVSA 3.3 GHz emission.

As all the hard X-ray and high-frequency flaring sources are observed at the main site, if we consider this site as the only reconnection location, the existence of the large LF emission from the outlying sources is hard to understand.

The possible scenario is that the small loop of the main site undergoes magnetic reconnection as in "standard 2D flare model", but the rising flux rope encounters overlying, oppositely-directed magnetic fields that undergo separate breakout reconnection. This may account for the delayed peak and slower decay of sources $S2$ and $S3$ in Figure 4.4 The particles accelerated in the main source reach the loop legs creating high-frequency microwave and hard X-ray emissions by trapping and collision of the electrons. This accounts for the particles that travel downwards in outflow from the current sheet of the reconnection region. The upward outflow and the outward movement of the reconnected flux rope from the reconnection region could not eject easily into the corona, because of the overlying loops. Therefore, these larger loops undergo "loop-loop interaction". The eruption of the flux loop from the Western far end of the active region is an indication of this interaction scenario.

The electrons at the LF sources are expected to be in the high energy range to create emissions at such low frequencies. The secondary sources are not observed in EOVSA high frequencies, NoRH 17 GHz and hard X-rays, which might be due to the weaker magnetic field strengths and higher mirror ratio at the legs of the large loops in the secondary site.

Based on all the observations discussed above, the flare scenario of this event is illustrated in the cartoon as shown in Figure 4.7. The onset of the flare takes place with the sequential reconnection in the small loop system (green). The star symbols

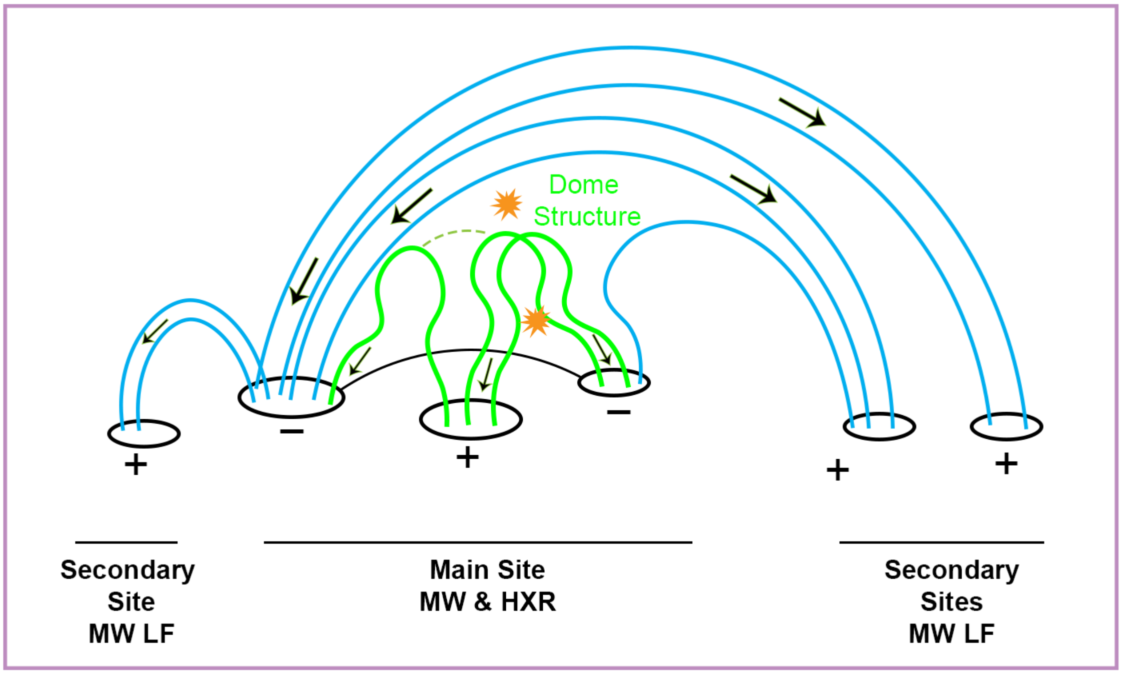

Figure 4.7 Cartoon showing the side-view of the possible flare scenario of the magnetic dome-structure with small and large overlying loop systems.

mark the reconnection sites. The accelerated particles travel to the loops creating footpoints and looptop sources observed in hard X-rays and microwave emission. The outflows from the rising structure of the small loop interact with the large overlying loops (blue) and cannot easily escape high in the corona; but they get enclosed by the large loops creating "3D loop-loop interaction" on the top of the small loops. The particles in this interaction go through trapping in the newly-reconnected large overlying loops, creating microwave LF sources at the secondary sites. This interaction also leads to eruption and restructuring the flux loop 6 in EUV emission Figure 4.6a. The EOVSA emission from this loop 6, if there is any, is not available in the image maps and hence is not discussed.

4.6 Discussion and Conclusions

This work focuses on the imaging spectroscopy of the LF sources observed in a C4.9 class flare. We report large-area microwave LF sources observed over a complex magnetic region during the flare. These LF sources show multiple centroids so that the sources taken together represent a very inhomogeneous emission. The frequency dependent source area measurements have shown that the emission, in particularly at low-frequencies, varies sharply with frequency. The large spatial extent of sources indicates the access of the particles accelerated during the flare to travel multiple locations of the flaring region. This event serves as a good example to show that a flat microwave spectrum is an evidence of large and inhomogeneous source emission that is spread over the flaring region and that which changes dramatically with the phases of the burst. The investigation of the microwave emission with other multi-wavelength observations have shown contribution of multiple loops with multitude scaled magnetic flux tubes and their interaction resulting in the flare eruption. This study also gives the need for having a new three-dimensional perspective and additional improvements over the standard solar flare model.

Chapter 5

SUMMARY AND FUTURE WORK

5.1 Summary of the Dissertation

Over the last few decades of microwave observations, a few studies have reported complex and extended source morphologies at low frequencies. Such sources are not entirely understood and cannot be explained by the standard flare model. In this context, the recent high-resolution daily observations made by EOVSA allow consistent observations of such emission that is yet to be explored fully.

This dissertation focuses on investigating gyrosynchrotron emission in solar flares at low microwave frequencies. The two studies discussed here are based on flare events observed by EOVSA with other multi-wavelength observations.

In the first study, we examine 12 flare events and their associated microwave bursts observed by EOVSA to understand the source morphology, occurrence rate, and characteristics of the exceptionally large LF sources.

1. These events were from 2015, during which EOVSA was in its pre-commissioning phase providing flux density data, but not microwave images. EOVSA has the state-of-the-art high cadence and high frequency resolution capability compared to any other radio instrument currently available for solar observations in the microwave range. This study focuses on the source morphology by primarily using the total-power flux density spectra and the some cross-correlated data of the events in the frequency range of 2.5 to 18 GHz.
2. The optically thick low-frequency index of the flux density spectrum is a clear indicator of source morphology and homogeneity. Upon analyzing the evolution of these indices with time for each event, we observed that around 42% of the flares (five out of 12 events) exhibit flat slope/low-index values. These five events have shown spectral index values less than 1.0 in at least one of the three phases of the bursts, compared to the theoretical value of ~ 2.9 for a homogeneous source. In particular, this flat spectral trend is observed to significantly increase in the decay phase of the bursts.

3. Using the relative visibility analysis, we found that the events that exhibit flat indices all have a large source size, up to ∼120 arcsec at low frequencies, relative to the more homogeneous flare sources. In addition, the observed flat spectra could only be reproduced by the inhomogeneous spectral modeling consisting of multiple emission components.

To summarize, we report that the microwave LF flare sources in the cases of flat flux density spectrum have to be large, extended, and complex, indicating that the accelerated particles can have access to large spatial volume, especially in the decay phase of the impulsive microwave emission.

The second part of this dissertation uses the understanding gleaned from the first study in the context of another event for which the full capability of high-resolution imaging spectroscopy from EOVSA is available. This work looks at the role of the unique LF sources during the impulsive phase of the flare phenomena.

1. The flare event studied here, of soft X-ray class C4.9, occurred on 04 April 2017 and serves as the best example to demonstrate the broad LF emission for its inhomogeneity. During the observation of this event, EOVSA produced images at 15 distinct frequencies channels in the range of 3.44 to 18 GHz.

2. We primarily examine the flux density spectra of the event corresponding to the evolution of the LF sources. The investigation stands as a proof of concept for the first study of this dissertation discussed in Chapter 3. The images show that the flat optically thick microwave spectrum is a clear indicator of broad elongated inhomogeneous source emissions observed at low frequencies. We observe that the source at 3.3 GHz is almost ten times as large as the high-frequency source and its associated hard X-ray sources. The power-law dependence of source area vs. frequency is found to be at least $A \propto f_{\mathrm{GHz}}^{-1.6}$ measured in the 10% level area in the entire frequency range, and as extreme as $A \propto f_{\mathrm{GHz}}^{-2.6}$ when considering only the LF emission. Within the 10% contour level, the area of the source seems to grow steeply by more than an order of magnitude as we move from high to low frequency. In contrast, the 50% area grows by only by a factor of ∼3.

3. Upon investigating the flaring region, the broad LF sources spreading over the whole flaring region demonstrates that the accelerated particles have access to multiple flux loops on which they somehow appeared almost simultaneously to create distinct source centroids connecting all of the major sunspots of the region. The magnetic field extrapolation shows a dome structure with a compact

> loop system crossed by overlying large loops. The small loop system must therefore somehow interact with the large overlying loops to accelerate or inject high-energy particles onto them, creating the extended LF sources.

The event studied here seems to exhibit both the “2D flare model” scenario with a flux rope eruption involving the small loop system and also the “loop-loop 3D interaction” between the small and overlying large loops. This leads to a more realistic flare model consisting of a multi-polar magnetic field configuration.

We outline that the LF sources are broadened from the accelerated particles that travel over a large spatial extent in the flaring active region, where other wavelength emissions are almost invisible. This highlights the diagnostic potential of microwave frequencies through which the physical conditions during flares can be directly interpreted.

5.2 Current and Future Endeavours

Preliminary Work from GSFIT procedure

To obtain the physical parameters and their space-time variation maps in a flare site, the observed spectra can be fitted with the GSFIT procedure. The parameters can be magnetic field strength, electron powerlaw index in energy, ambient temperature and plasma density, viewing angle, and others, as discussed in [20, 66].

As discussed in Chapter 2, GSFIT can simultaneously perform model fitting of the spectra produced from each pixel, read over the image map cube. For the second study of this dissertation, we have generated some highly preliminary fitting for brightness temperature maps as shown in Figure 5.1. Spectra from each of the pixels marked by the dashed lines are read from the left panels and shown in the right panels of Figure 5.1 along with the corresponding fits and their parameters. The pixels selected in the two image panels are the two different source centroids observed at the main site of the flare.

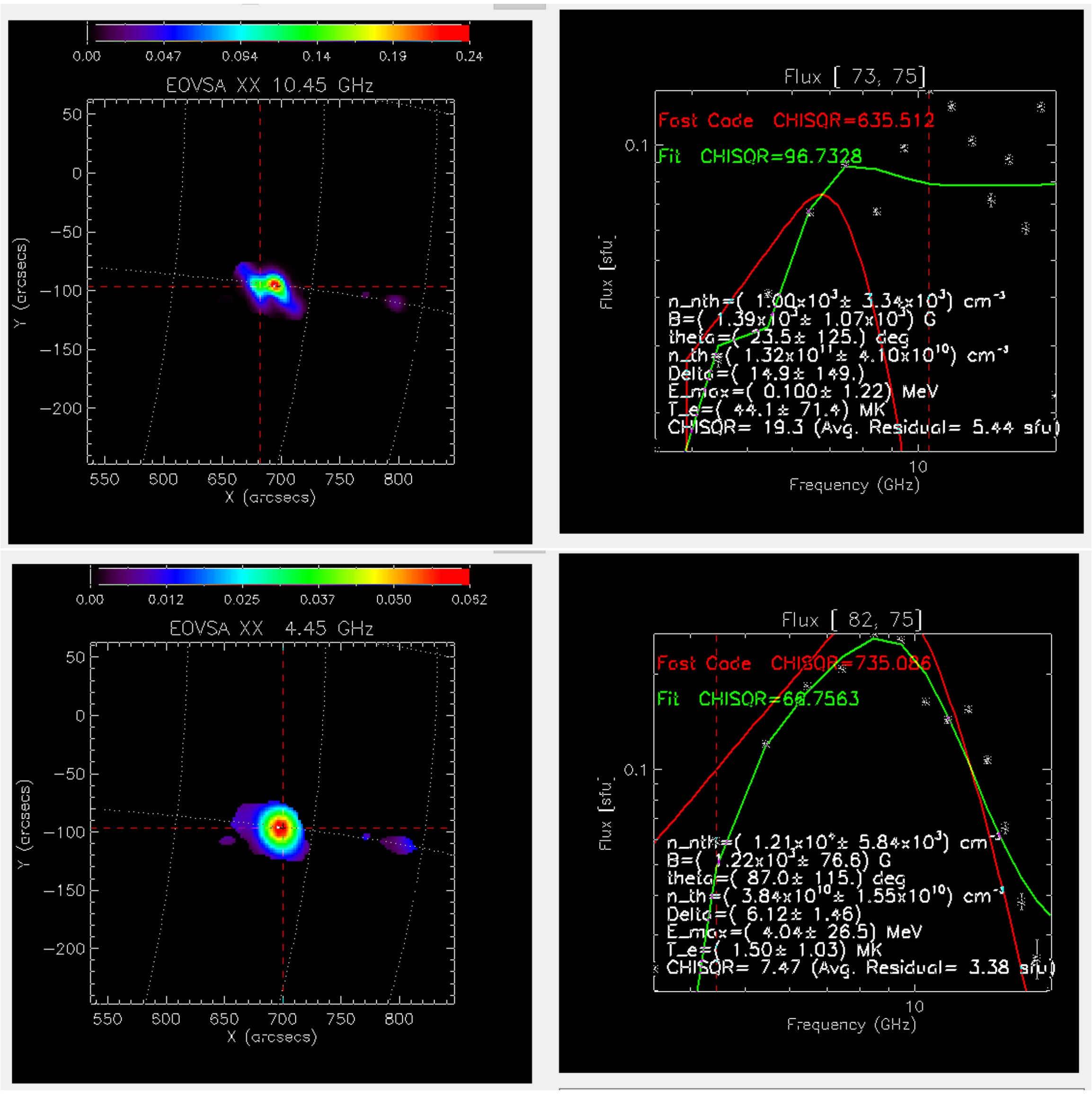

```
n_nth=( 1.00x10³± 3.34x10³) cm⁻³
B=( 1.39x10³± 1.07x10³) G
theta=( 23.5± 125.) deg
n_th=( 1.32x10¹¹± 4.10x10¹⁰) cm⁻³
Delta=( 14.9± 149.)
E_max=( 0.100± 1.22) MeV
T_e=( 44.1± 71.4) MK
CHISQR= 19.3 (Avg. Residual= 5.44 sfu)
```

```
n_nth=( 1.21x10⁴± 5.84x10³) cm⁻³
B=( 1.22x10³± 76.6) G
theta=( 87.0± 115.) deg
n_th=( 3.84x10¹⁰± 1.55x10¹⁰) cm⁻³
Delta=( 6.12± 1.46)
E_max=( 4.04± 26.5) MeV
T_e=( 1.50± 1.03) MK
CHISQR= 7.47 (Avg. Residual= 3.38 sfu)
```

Figure 5.1 Preliminary GSFIT fitting parameters for the pixels selected in the main site with different centroids at the low-frequency and high-frequency. Panels on the left show the image maps with frequency, and the panels on the right show the fitting parameters for the pixel selected in the image map.

As a concluding remark to this dissertation, the future directions and scope are outlined below:

- **Obtaining and Refining Physical Parameters from GSFIT**

  To better understand the relationship between the particles in the remote sites and those in the main flare site, it would be highly advantageous to obtain the particle energy distribution parameters from GSFIT in the four different sites. Unfortunately, the remote sites appear only at a few of the lowest frequencies, and even then only in the lowest contour levels, making it challenging to obtain good spectral fits. Still, the spatially resolved spectra at those locations do contain the information needed to at least constrain the particle energies, and this is future work to be attempted.

  After obtaining the best fits to a spectrum, characterizing the uncertainties between model fit and the observed data, and potential cross-correlations among parameters, are essential steps for spectral fitting. The Markov Chain Monte Carlo (MCMC) method [15, 14, 100, 104] helps to achieve parameter uncertainties as well as to explore their interdependence. A pre-defined range of free parameters will be required to perform this minimization. An example for a different event is shown in Figure 5.2 after such minimization to result in final parameter distributions.

- **Three-dimensional modeling with GX-simulator**

  The preliminary magnetic extrapolation maps from GX-simulator have shown the associated flux ropes in the flaring region. The GX-simulator modeling tool can simulate the imaging and spectral data in the gyrosynchrotron frequency range with other complementary data as described in Chapter 2 [88]. We aim to reproduce microwave images and deduce the local plasma parameters, especially at the low-frequency emission.

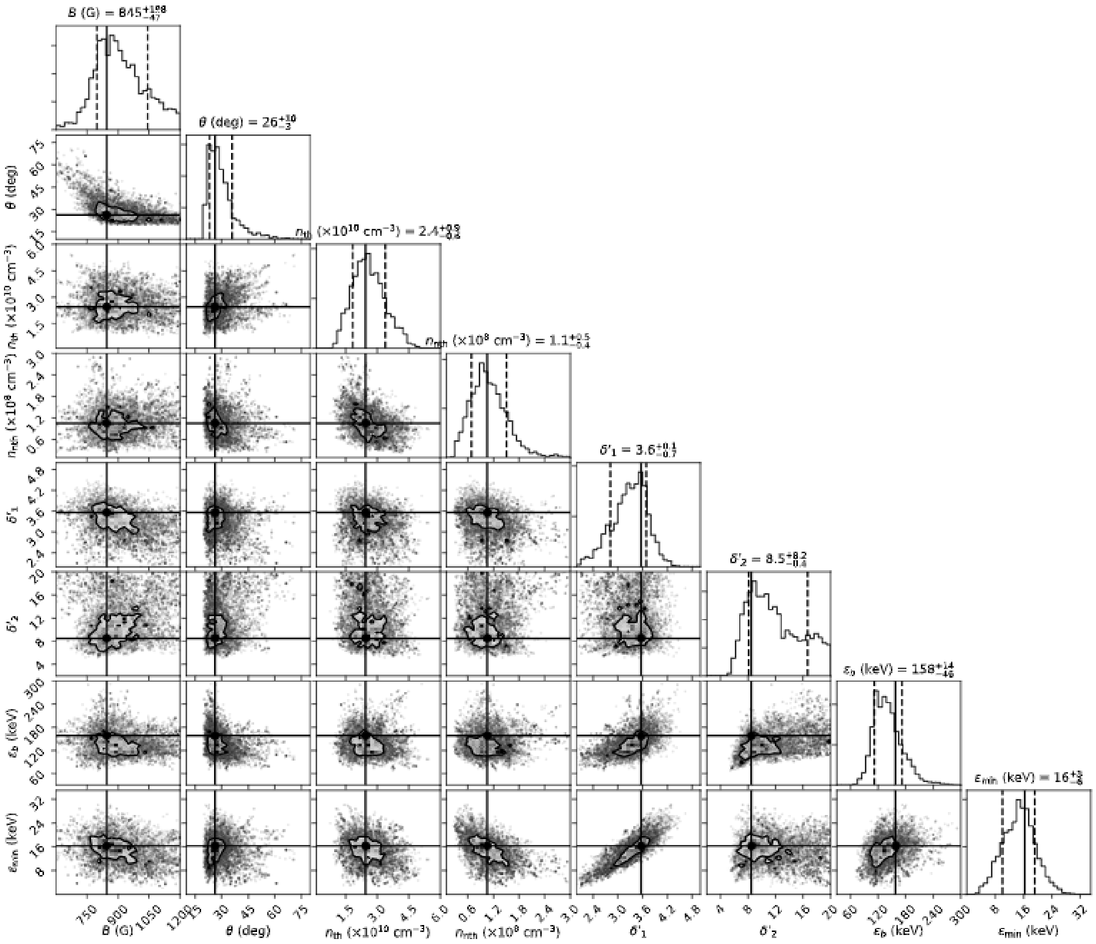

Figure 5.2 Each panel shows the final 2D distribution of the fit parameters and the results obtained from MCMC analysis. The histogram of individual parameter is plotted on the top panel of each column.

Source: [14]

REFERENCES

[1] A. A. Altyntsev, G. D. Fleishman, S. V. Lesovoi, and N. S. Meshalkina. Thermal to Nonthermal Energy Partition at the Early Rise Phase of Solar Flares. *Astrophysical Journal*, 758(2):138, October 2012.

[2] M. J. Aschwanden. Particle acceleration and kinematics in solar flares - A Synthesis of Recent Observations and Theoretical Concepts (Invited Review). *Space Science Reviews*, 101(1):1–227, January 2002.

[3] M. J. Aschwanden. *Physics of the Solar Corona. An Introduction.* Springer, 2004.

[4] T. S. Bastian. Impulsive flares: A microwave perspective. In *Proc. Nobeyama Symp*, pages 211–222. Nobeyama Radio Observatory (NRO) Report, 1999.

[5] T. S. Bastian, A. O. Benz, and D. E. Gary. Radio Emission from Solar Flares. *Annual Review of Astronomy and Astrophysics*, 36:131–188, 1998.

[6] T. S. Bastian, G. D. Fleishman, and D. E. Gary. Radio Spectral Evolution of an X-Ray–poor Impulsive Solar Flare: Implications for Plasma Heating and Electron Acceleration. *Astrophysical Journal*, 666(2):1256–1267, sep 2007.

[7] T. S. Bastian and A. L. Kiplinger. VLA and Hα Observations of the M8.7 Flare of 17 June 1989: A Preliminary Report. In R. M. Winglee and A. L. Kiplinger, editors, *Max '91/SMM Solar Flares: Observations and Theory*, page 153, 1991.

[8] L. Belkora. Time Evolution of Solar Microwave Bursts. *Astrophysical Journal*, 481:532–544, May 1997.

[9] L. A. Belkora. *Interferometric Studies of the Sun at Microwave and Millimeter Wavelengths.* PhD thesis, Univeristy of Colorado at Boulder., January 1995.

[10] A. O. Benz. Flare Observations. *Living Reviews in Solar Physics*, 5(1):1, December 2008.

[11] A. O. Benz. Flare Observations. *Living Reviews in Solar Physics*, 14(1):2, December 2017.

[12] H. Carmichael. *A Process for Flares*, volume 50, page 451. Greenbelt, MD. Proceedings of the AAS-NASA Symposium, 1964.

[13] R. C. Carrington. Description of a Singular Appearance seen in the Sun on September 1, 1859. *Monthly Notices of the Royal Astronomical Society*, 20:13–15, November 1859.

[14] B. Chen, M. Battaglia, S. Krucker, K. K. Reeves, and L. Glesener. Energetic Electron Distribution of the Coronal Acceleration Region: First Results from Joint Microwave and Hard X-Ray Imaging Spectroscopy. *Astrophysical Journal Letters*, 908(2):L55, February 2021.

[15] B. Chen, C. Shen, D. E. Gary, K. K. Reeves, G. D. Fleishman, S. Yu, F. Guo, S. Krucker, J. Lin, G. M. Nita, and X. Kong. Measurement of Magnetic Field and Relativistic Electrons Along a Solar Flare Current Sheet. *Nature Astronomy*, 4:1140–1147, January 2020.

[16] L. Doyle, P. F. Wyper, E. Scullion, J. A. McLaughlin, G. Ramsay, and J. G. Doyle. Observations and 3D Magnetohydrodynamic Modeling of a Confined Helical Jet Launched by a Filament Eruption. *Astrophysical Journal*, 887(2):246, December 2019.

[17] G. A. Dulk. Radio Emission From the Sun and Stars. *Annual Review of Astronomy and Astrophysics*, 23:169–224, 1985.

[18] G. A. Dulk, T. S. Bastian, and S. R. Kane. Two-Frequency Imaging of Microwave Impulsive Flares near the Solar Limb. *Astrophysical Journal*, 300:438–441, January 1986.

[19] G. A. Dulk and K. A. Marsh. Simplified Expressions for the Gyrosynchrotron Radiation from Mildly Relativistic, Nonthermal and Thermal Electrons. *Astrophysical Journal*, 259:350–358, August 1982.

[20] G. D. Fleishman, D. E. Gary, B. Chen, N. Kuroda, S. Yu, and G. M. Nita. Decay of the Coronal Magnetic Field can Release Sufficient Energy to Power a Solar Flare. *Science*, 367(6475):278–280, January 2020.

[21] G. D. Fleishman and A. A. Kuznetsov. Fast Gyrosynchrotron Codes. *Astrophysical Journal*, 721:1127–1141, October 2010.

[22] G. D. Fleishman, M. A. Loukitcheva, Varvara Yu. Kopnina, G. M. Nita, and D. E. Gary. The Coronal Volume of Energetic Particles in Solar Flares as Revealed by Microwave Imaging. *Astrophysical Journal*, 867(1):81, November 2018.

[23] G. D. Fleishman and V. F. Melnikov. Gyrosynchrotron Emission from Anisotropic Electron Distributions. *Astrophysical Journal*, 587(2):823–835, April 2003.

[24] G. D. Fleishman and V. F. Melnikov. Optically Thick Gyrosynchrotron Emission from Anisotropic Electron Distributions. *Astrophysical Journal*, 584(2):1071–1083, February 2003.

[25] G. D. Fleishman, G. M. Nita, and D. E. Gary. A Large-scale Plume in an X-class Solar Flare. *Astrophysical Journal*, 845:135, August 2017.

[26] G. D. Fleishman, V. D. Pal'shin, N. Meshalkina, A. L. Lysenko, L. K. Kashapova, and A. T. Altyntsev. A Cold Flare with Delayed Heating. *Astrophysical Journal*, 822:71, May 2016.

[27] G. D. Fleishman, V. D. Pal'shin, N. Meshalkina, A. L. Lysenko, L. K. Kashapova, and A. T. Altyntsev. A Cold Flare with Delayed Heating. *Astrophysical Journal*, 822(2):71, May 2016.

[28] K. Fujiki. *High Spatial Resolution Imaging for the Nobeyama Radioheliograph and Observations of Weak Activities Prior to Solar Flares*. PhD thesis, University of Tokyo, Japan, January 1997.

[29] D. E. Gary. Cause and Extent of the Extreme Radio Flux Density Reached by the Solar Flare of 2006 December 06. *arXiv e-prints*, page arXiv:1901.09262, January 2019.

[30] D. E. Gary, B. Chen, B. R. Dennis, G. D. Fleishman, G. J. Hurford, S. Krucker, J. M. McTiernan, G. M. Nita, A. Y. Shih, S. M. White, and S. Yu. Microwave and Hard X-Ray Observations of the 2017 September 10 Solar Limb Flare. *Astrophysical Journal*, 863:83, August 2018.

[31] D. E. Gary, G. D. Fleishman, and G. M. Nita. Magnetography of Solar Flaring Loops with Microwave Imaging Spectropolarimetry. *Solar Physics*, 288(2):549–565, December 2013.

[32] D. E. Gary and G. J. Hurford. A Simple Solar Microwave Burst Observed with High Spectral Resolution. *Astrophysical Journal*, 339:1115–1122, April 1989.

[33] D. E. Gary and G. J. Hurford. Multifrequency Observations of a Solar Microwave Burst with Two-dimensional Spatial Resolution. *Astrophysical Journal*, 361:290–299, September 1990.

[34] D. E. Gary and G. J. Hurford. Radio Spectral Diagnostics. In D. E. Gary and C. U. Keller, editors, *Astrophysics and Space Science Library*, volume 314 of *Astrophysics and Space Science Library*, page 71, September 2004.

[35] D. E. Gary and G. J. Hurford. *Radio Spectral Diagnostics*, pages 71–87. Springer Netherlands, Dordrecht, 2005.

[36] D. E. Gary, G. J. Hurford, G. M. Nita, S. M. White, J. McTiernan, and G. D. Fleishman. The Expanded Owens Valley Solar Array (EOVSA). In *American Astronomical Society Meeting Abstracts*, volume 224 of *American Astronomical Society Meeting Abstracts*, page 123.60, June 2014.

[37] D. E. Gary and C. U. Keller. Solar and Space Weather Radiophysics - Current Status and Future Developments. *Astrophysics and Space Science Library*, 314, September 2004.

[38] G. A. Gary and R. L. Moore. Eruption of a Multiple-Turn Helical Magnetic Flux Tube in a Large Flare: Evidence for External and Internal Reconnection That Fits the Breakout Model of Solar Magnetic Eruptions. *Astrophysical Journal*, 611(1):545–556, August 2004.

[39] V. L. Ginzburg and S. I. Syrovatskii. Cosmic Magnetobremsstrahlung (synchrotron Radiation). *Annual Review of Astronomy and Astrophysics*, 3:297, January 1965.

[40] V. V. Grechnev, M. R. Kundu, and A. Nindos. A Study of Accelerated Electrons in Solar Flares Using Microwave and X-Ray Observations. *Publications of the Astronomical Society of Japan*, 58:47–54, February 2006.

[41] D. A. Guidice and J. P. Castelli. Spectral Distributions of Microwave Bursts. *Solar Physics*, 44(1):155–172, 1975.

[42] O Hachenberg and G Valais. The Spectrum of the Bursts of the Radiofrequency Radiation of the Sun in the cm-wave Range. With 21 Text Images. *Journal for astrophysics*, 52:42, 1961.

[43] Y. Hanaoka. Flares and Plasma Flow Caused by Interacting Coronal Loops. *Solar Physics*, 165(2):275–301, May 1996.

[44] Y. Hanaoka. Double-Loop Configuration of Solar Flares. *Solar Physics*, 173:319–346, July 1997.

[45] Y. Hanaoka. High-Energy Electrons in Double-Loop Flares. *Publications of the Astronomical Society of Japan*, 51:483–496, August 1999.

[46] T. Hirayama. Theoretical Model of Flares and Prominences. I: Evaporating Flare Model. *Solar Physics*, 34(2):323–338, February 1974.

[47] R. Hodgson. On a Curious Appearance Seen in the Sun. *Monthly Notices of the Royal Astronomical Society*, 20:15–16, Nov 1859.

[48] P. Hoyng, A. Duijveman, M. E. Machado, D. M. Rust, Z. Svestka, A. Boelee, C. de Jager, K. T. Frost, H. Lafleur, G. M. Simnett, H. F. van Beek, and B. E. Woodgate. Origin and Location of the Hard X-Ray Emission in a Two-Ribbon Flare. *Astrophysical Journal Letters*, 246:L155, June 1981.

[49] J.-E. Hwangbo, J. Lee, S.-H. Park, S. Kim, D.-Y. Lee, S.-C. Bong, Y.-H. Kim, K.-S. Cho, and Y.-D. Park. Magnetic Structure and Nonthermal Electrons in the X6.9 Flare on 2011 August 9. *Astrophysical Journal*, 796:80, December 2014.

[50] T. I. Kaltman, A. N. Korzhavin, and N. G. Peterova. The Self-Inversion of the Sign of Circular Polarization in “Halo” Microwave Sources. *Solar Physics*, 242:125–142, May 2007.

[51] S. R. Kane. Impulsive (flash) Phase of Solar Flares: Hard X-Ray Microwave, EUV and Optical Observations. In Gordon Allen Newkirk, editor, *Coronal Disturbances*, volume 57 of *IAU Symposium*, page 105. International Astronomical Union. Symposium no. 57, Dordrecht; Boston: Reidel, Jan 1974.

[52] P. M. Kintner, B. O'Hanlon, D. E. Gary, and P. M. S. Kintner. Global Positioning System and solar radio burst forensics. *Radio Science*, 44(2):RS0A08, June 2009.

[53] K.-L. Klein. Microwave radiation from a dense magneto-active plasma. *Astronomy and Astrophysics*, 183:341–350, September 1987.

[54] K.-L. Klein and G. Trottet. Gyrosynchrotron Radiation from a Source with Spatially Varying Field and Density. *Astronomy and Astrophysics*, 141:67–76, December 1984.

[55] K.-L. Klein, G. Trottet, and A. Magun. Microwave Diagnostics of Energetic Electrons in Flares. *Solar Physics*, 104:243–252, March 1986.

[56] L. G. Kocharov, Jeongwoo W. Lee, H. Zirin, G. A. Kovaltsov, I. G. Usoskin, K. R. Pyle, M. A. Shea, and D. F. Smart. Neutron and Electromagnetic Emissions During the 1990 May 24 Solar Flare. *Solar Physics*, 155(1):149–170, November 1994.

[57] R. A. Kopp and G. W. Pneuman. Magnetic Reconnection in the Corona and the Loop Prominence Phenomenon. *Solar Physics*, 50(1):85–98, October 1976.

[58] T. Kosugi, K. Makishima, T. Murakami, T. Sakao, T. Dotani, M. Inda, K. Kai, S. Masuda, H. Nakajima, Y. Ogawara, M. Sawa, and K. Shibasaki. The Hard X-ray Telescope (HXT) for the SOLAR-A mission. *Solar Physics*, 136(1):17–36, November 1991.

[59] S. Krucker, H. S. Hudson, L. Glesener, S. M. White, S. Masuda, J. P. Wuelser, and R. P. Lin. Measurements of the Coronal Acceleration Region of a Solar Flare. *Astrophysical Journal*, 714(2):1108–1119, May 2010.

[60] T. A. Kucera, G. A. Dulk, D. E. Gary, and T. S. Bastian. A Multisource Limb Flare Observed at Multiple Radio Wavelengths. *Astrophysical Journal*, 433:875–885, October 1994.

[61] M. R. Kundu, V. I. Garaimov, S. M. White, and S. Krucker. Nobeyama Radioheliograph and RHESSI Observations of the X1.5 Flare of 2002 April 21. *Astrophysical Journal*, 600(2):1052–1060, January 2004.

[62] M. R. Kundu, V. V. Grechnev, V. I. Garaimov, and S. M. White. Double Loop Configuration of a Flaring Region from Microwave, Extreme-Ultraviolet, and X-Ray Imaging Data. *Astrophysical Journal*, 563:389–402, December 2001.

[63] M. R. Kundu, V. V. Grechnev, V. I. Garaimov, and S. M. White. Double Loop Configuration of a Flaring Region from Microwave, Extreme-Ultraviolet, and X-Ray Imaging Data. *Astrophysical Journal*, 563(1):389–402, December 2001.

[64] M. R. Kundu, A. Nindos, S. M. White, and V. V. Grechnev. A Multiwavelength Study of Three Solar Flares. *Astrophysical Journal*, 557(2):880–890, August 2001.

[65] M. R. Kundu, S. M. White, K. Shibasaki, and J. P. Raulin. A Radio Study of the Evolution of Spatial Structure of an Active Region and Flare Productivity. *Astrophysical Journal, Supplement*, 133(2):467–482, April 2001.

[66] N. Kuroda, G. D. Fleishman, D. E. Gary, G. M. Nita, B. Chen, and S. Yu. Evolution of Flare-accelerated Electrons Quantified by Spatially Resolved Analysis. *Frontiers in Astronomy and Space Sciences*, 7:22, May 2020.

[67] N. Kuroda, D. E. Gary, H. Wang, G. D. Fleishman, G. M. Nita, and J. Jing. Three-dimensional Forward-fit Modeling of the Hard X-Ray and Microwave Emissions of the 2015 June 22 M6.5 Flare. *Astrophysical Journal*, 852:32, January 2018.

[68] J. Lee, D. E. Gary, and K. Shibasaki. Magnetic Trapping and Electron Injection in Two Contrasting Solar Microwave Bursts. *Astrophysical Journal*, 531:1109–1120, March 2000.

[69] J. Lee, D. Lim, G. S. Choe, K.-S. Kim, and M. Jang. Coronal Thick Target Hard X-Ray Emissions and Radio Emissions. *Astrophysical Journal Letters*, 769:L11, May 2013.

[70] J. W. Lee, D. E. Gary, and H. Zirin. Flat microwave spectra seen at x-class flares. *Solar Physics*, 152(2):409–428, 1994.

[71] J. R. Lemen, A. M. Title, D. J. Akin, P. F. Boerner, C. Chou, J. F. Drake, D. W. Duncan, C. G. Edwards, F. M. Friedlaender, G. F. Heyman, N. E. Hurlburt, N. L. Katz, G. D. Kushner, M. Levay, R. W. Lindgren, D. P. Mathur, E. L. McFeaters, S. Mitchell, R. A. Rehse, C. J. Schrijver, L. A. Springer, R. A. Stern, T. D. Tarbell, J-P. Wuelser, C. J. Wolfson, C. Yanari, J. A. Bookbinder, P. N. Cheimets, D. Caldwell, E. E. Deluca, R. Gates, L. Golub, S. Park, W. A. Podgorski, Rock I. Bush, Philip H. Scherrer, M. A. Gummin, P. Smith, G. Auker, P. Jerram, P. Pool, R. Soufli, D. L. Windt, S. Beardsley, M. Clapp, J. Lang, and N. Waltham. The Atmospheric Imaging Assembly (AIA) on the Solar Dynamics Observatory (SDO). *Solar Physics*, 275(1-2):17–40, January 2012.

[72] J. Lim, D. E. Gary, G. J. Hurford, and J. R. Lemen. Imaging Spectroscopy of Solar Microwave Radiation. I. Flaring Emission. *Astrophysical Journal*, 430:425–434, July 1994.

[73] R. P. Lin, B. R. Dennis, G. J. Hurford, D. M. Smith, A. Zehnder, P. R. Harvey, D. W. Curtis, D. Pankow, P. Turin, M. Bester, A. Csillaghy, M. Lewis, N. Madden, H. F. van Beek, M. Appleby, T. Raudorf, J. McTiernan, R. Ramaty, E. Schmahl, R. Schwartz, S. Krucker, R. Abiad, T. Quinn, P. Berg, M. Hashii, R. Sterling, R. Jackson, R. Pratt, R. D. Campbell, D. Malone, D. Landis, C. P. Barrington-Leigh, S. Slassi-Sennou, C. Cork, D. Clark, D. Amato, L. Orwig, R. Boyle, I. S. Banks, K. Shirey, A. K. Tolbert, D. Zarro, F. Snow, K. Thomsen, R. Henneck, A. McHedlishvili, P. Ming, M. Fivian, John Jordan, Richard Wanner, J. Crubb, J. Preble, M. Matranga, A. Benz, H. Hudson, R. C. Canfield, G. D. Holman, C. Crannell, T. Kosugi, A. G. Emslie, N. Vilmer, J. C. Brown, C. Johns-Krull, M. Aschwanden, T. Metcalf, and A. Conway. The Reuven Ramaty High-Energy Solar Spectroscopic Imager (RHESSI). *Solar Physics*, 210(1):3–32, November 2002.

[74] C. Liu, J. Lee, D. E. Gary, and H. Wang. The Ribbon-like Hard X-Ray Emission in a Sigmoidal Solar Active Region. *Astrophysical Journal Letters*, 658(2):L127–L130, April 2007.

[75] A. L. Lysenko, D. D. Fredericks, G. D. Fleishman, R. L. Aptekar, A. T. Altyntsev, S. V. Golenetsky, D. S. Svinkin, M. V. Ulanov, A. E. Tsvetkova, and A. V. Ridnaya. X-ray and Gamma Radiation from Solar Flares . *Advances in Physical Sciences*, 190(8):878–894, 2020.

[76] S. Masuda, M. Shimojo, T. Kawate, S. Ishikawa, and M. Ohno. Extremely Microwave-Rich Solar Flare Observed with Nobeyama Radioheliograph. *Publications of the Astronomical Society of Japan*, 65:S1, December 2013.

[77] V. F. Melnikov, D. E. Gary, and G. M. Nita. Peak Frequency Dynamics in Solar Microwave Bursts. *Solar Physics*, 253:43–73, December 2008.

[78] V. F. Melnikov, S. P. Gorbikov, V. E. Reznikova, and K. Shibasaki. Dynamics of Electron Spatial Distribution in Microwave Flaring Loops. In D. Danesy, S. Poedts, A. de Groof, and J. Andries, editors, *The Dynamic Sun: Challenges for Theory and Observations*, volume 11 of *ESA Special Publication*, page 132.1. Leuven, Belgium. Proceedings of the 11th European Solar Physics Meeting. Published on CDROM, December 2005.

[79] V. F. Melnikov, V. E. Reznikova, K. Shibasaki, and V. M. Nakariakov. Spatially Resolved Microwave Pulsations of a Flare Loop. *Astronomy and Astrophysics*, 439:727–736, August 2005.

[80] V. F. Melnikov, K. Shibasaki, and V. E. Reznikova. Loop-Top Nonthermal Microwave Source in Extended Solar Flaring Loops. *Astrophysical Journal Letters*, 580(2):L185–L188, December 2002.

[81] D. B. Melrose. A Solar Flare Model Based on Magnetic Reconnection between Current-carrying Loops. *Astrophysical Journal*, 486(1):521–533, September 1997.

[82] H. Nakajima, B. R. Dennis, P. Hoyng, G. Nelson, T. Kosugi, and K. Kai. Microwave and X-ray Observations of Delayed Brightenings at Sites Remote from the Primary Flare Locations. *Astrophysical Journal*, 288:806–819, January 1985.

[83] H. Nakajima, H. Sekiguchi, M. Sawa, K. Kai, and S. Kawashima. The Radiometer and Polarimeters at 80, 35, and 17 GHz for Solar Observations at Nobeyama. *Publications of the Astronomical Society of Japan*, 37:163–170, 1985.

[84] W. M. Neupert. Comparison of Solar X-Ray Line Emission with Microwave Emission during Flares. *Astrophysical Journal*, 153:L59, Jul 1968.

[85] A. Nindos. Incoherent Solar Radio Emission. *Frontiers in Astronomy and Space Sciences*, 7:57, November 2020.

[86] A. Nindos, S. M. White, M. R. Kundu, and D. E. Gary. Observations and Models of a Flaring Loop. *Astrophysical Journal*, 533:1053–1062, April 2000.

[87] M. Nishio, K. Yaji, T. Kosugi, H. Nakajima, and T. Sakurai. Magnetic Field Configuration in Impulsive Solar Flares Inferred from Coaligned Microwave/X-Ray Images. *Astrophysical Journal*, 489:976–991, November 1997.

[88] G. M. Nita, G. D. Fleishman, A. A. Kuznetsov, E. P. Kontar, and D. E. Gary. Three-dimensional Radio and X-Ray Modeling and Data Analysis Software: Revealing Flare Complexity. *Astrophysical Journal*, 799:236, February 2015.

[89] G. M. Nita, J. Hickish, D. MacMahon, and D. E. Gary. EOVSA Implementation of a Spectral Kurtosis Correlator for Transient Detection and Classification. *Journal of Astronomical Instrumentation*, 5(4):1641009–7366, Dec 2016.

[90] N. Omodei, M. Pesce-Rollins, F. Longo, A. Allafort, and S. Krucker. Fermi-LAT Observations of the 2017 September 10 Solar Flare. *Astrophysical Journal Letters*, 865:L7, September 2018.

[91] W. D. Pesnell, B. J. Thompson, and P. C. Chamberlin. The Solar Dynamics Observatory (SDO). *Solar Physics*, 275(1-2):3–15, Jan 2012.

[92] N. G. Peterova, L. V. Opeikina, and N. A. Topchilo. “Halo” Type Sources from Microwave Observations with High Angular Resolution. *Geomagnetism and Aeronomy*, 54:1053–1057, December 2014.

[93] L. E. Peterson and J. R. Winckler. Gamma-Ray Burst from a Solar Flare. *Journal of Geophysical Research*, 64(7):697–707, July 1959.

[94] V. Petrosian. Synchrotron Emissivity from Mildly Relativistic Particles. *Astrophysical Journal*, 251:727–738, December 1981.

[95] R. Ramaty. Gyrosynchrotron Emission and Absorption in a Magnetoactive Plasma. *Astrophysical Journal*, 158:753, November 1969.

[96] R. Ramaty and R. E. Lingenfelter. The Influence of the Ionized Medium on Synchrotron Emission Spectra in the Solar Corona. *Journal of Geophysical Research*, 72:879, February 1967.

[97] R. Ramaty and V. Petrosian. Free-Free Absorption of Gyrosynchrotron Radiation in Solar Microwave Bursts. *Astrophysical Journal*, 178:241–250, November 1972.

[98] P. H. Scherrer, J. Schou, R. I. Bush, A. G. Kosovichev, R. S. Bogart, J. T. Hoeksema, Y. Liu, T. L. Duvall, J. Zhao, A. M. Title, C. J. Schrijver, T. D. Tarbell, and S. Tomczyk. The Helioseismic and Magnetic Imager (HMI) Investigation for the Solar Dynamics Observatory (SDO). *Solar Physics*, 275:207–227, January 2012.

[99] S. B. Shaik and D. E. Gary. Implications of Flat Optically Thick Microwave Spectra in Solar Flares for Source Size and Morphology. *arXiv e-prints*, page arXiv:2107.00192, June 2021.

[100] R. Sharma, M. Battaglia, Y. Luo, B. Chen, and S. Yu. Radio and X-Ray Observations of Short-lived Episodes of Electron Acceleration in a Solar Microflare. *Astrophysical Journal*, 904(2):94, December 2020.

[101] R. K. Shevgaonkar and M. R. Kundu. Dual Frequency Observations of Solar Microwave Bursts using the VLA. *Astrophysical Journal*, 292:733–751, May 1985.

[102] K. Shibasaki, T. Takano, S. Enome, H. Nakajima, M. Nishio, Y. Hanaoka, C. Torii, H. Sekiguchi, T. Bushimata, S. Kawashima, N. Shinohara, H. Koshiishi, and Y. Shiomi. Thermal and Nonthermal Flare Emission Observed with the Nobeyama Radio Heliograph. *Space Science Reviews*, 68:217–224, May 1994.

[103] K. Shibata, S. Masuda, M. Shimojo, H. Hara, T. Yokoyama, S. Tsuneta, T. Kosugi, and Y. Ogawara. Hot-Plasma Ejections Associated with Compact-Loop Solar Flares. *Astrophysical Journal Letters*, 451:L83, October 1995.

[104] D. F. Silva, P. J. A. Simões, R. F. Hidalgo Ramírez, and A. Válio. Inferring the Magnetic Field Asymmetry of Solar Flares from the Degree of Polarisation at Millimetre Wavelengths. *Solar Physics*, 295(6):73, June 2020.

[105] P. J. A. Simões and J. E. R. Costa. Solar Bursts Gyrosynchrotron Emission from Three-Dimensional Sources. *Astronomy and Astrophysics*, 453:729–736, July 2006.

[106] Q. W. Song, H. Nakajima, G. L. Huang, B. L. Tan, Y. Huang, and Z. Wu. Turnover Frequency in Solar Microwave Bursts with an Extremely Flat Optically Thin Spectrum. *Solar Physics*, 291:3619–3635, December 2016.

[107] M. Stähli, D. E. Gary, and G. J. Hurford. High Resolution Microwave Spectras of Solar Bursts. *Solar Physics*, 120:351–368, September 1989.

[108] P. A. Sturrock. Model of the High-Energy Phase of Solar Flares. *Nature*, 211(5050):695–697, August 1966.

[109] T. Takakura. The Self Absorption of Gyro-Synchrotron Emission in a Magnetic Dipole Field: Microwave Impulsive Burst and Hard X-Ray Burst. *Solar Physics*, 26:151–175, September 1972.

[110] T. Takakura and K. Kai. Spectra of Solar Radio Type IV Bursts. *Publications of the Astronomical Society of Japan*, 13:94, 1961.

[111] T. Takakura and K. Kai. Energy Distribution of Electrons Producing Microwave Impulsive Bursts and X-Ray Bursts from the Sun. *Publications of the Astronomical Society of Japan*, 18:57, January 1966.

[112] T. Takakura and E. Scalise. Gyro-Synchrotron Emission in a Magnetic Dipole Field for the Application to the Center-to-Limb Variation of Microwave Impulsive Bursts. *Solar Physics*, 11:434–455, March 1970.

[113] T. Takano, H. Nakajima, S. Enome, K. Shibasaki, M. Nishio, Y. Hanaoka, Y. Shiomi, H. Sekiguchi, S. Kawashima, T. Bushimata, N. Shinohara, C. Torii, K. Fujiki, and Y. Irimajiri. *An Upgrade of Nobeyama Radioheliograph to a Dual-Frequency (17 and 34 GHz) System*, volume 483. Springer, 1997.

[114] M. Temmer, A. M. Veronig, B. Vršnak, and C. Miklenic. Energy Release Rates along Hα Flare Ribbons and the Location of Hard X-Ray Sources. *Astrophysical Journal*, 654(1):665–674, January 2007.

[115] C. Torii, Y. Tsukiji, S. Kobayashi, N. Yoshimi, H. Tanaka, and S. Enome. Full-Automatic Radiopolarimeters for Solar Patrol at Microwave Frequencies. *Proceedings of the Research Institute of Atmospherics, Nagoya University*, 26:129–132, March 1979.

[116] H. Wang, D. E. Gary, J. Lim, and R. A. Schwartz. Miocrowave Spectral Imaging, H-alpha and Hard X-ray Observations of a Solar Limb Flare. *Astrophysical Journal*, 433:379–388, September 1994.

[117] H. Wang and C. Liu. Circular Ribbon Flares and Homologous Jets. *Astrophysical Journal*, 760(2):101, December 2012.

[118] H. J. Wiehl, D. A. Batchelor, C. J. Crannell, B. R. Dennis, P. N. Price, and A. Magun. Great Microwave Bursts and Hard X-Rays from Solar Flares. *Solar Physics*, 96(2):339–356, April 1985.

[119] T. N. Woods, F. G. Eparvier, R. Hock, A. R. Jones, D. Woodraska, D. Judge, L. Didkovsky, J. Lean, J. Mariska, H. Warren, D. McMullin, P. Chamberlin, G. Berthiaume, S. Bailey, T. Fuller-Rowell, J. Sojka, W. K. Tobiska, and R. Viereck. Extreme Ultraviolet Variability Experiment (EVE) on the Solar Dynamics Observatory (SDO): Overview of Science Objectives, Instrument Design, Data Products, and Model Developments. *Solar Physics*, 275(1-2):115–143, Jan 2012.

[120] S. Yang and J. Zhang. Mini-filament Eruptions Triggering Confined Solar Flares Observed by ONSET and SDO. *Astrophysical Journal Letters*, 860(2):L25, June 2018.

[121] S. Yu, B. Chen, K. K. Reeves, D. E. Gary, S. Musset, G. D. Fleishman, G. M. Nita, and L. Glesener. Magnetic Reconnection During the Post-Impulsive Phase of a Long-duration Solar Flare: Bidirectional Outflows as a Cause of Microwave and X-Ray Bursts. *Astrophysical Journal*, 900(1):17, September 2020.